Dynamic Cantilever Magnetometry of Reversal Processes and Phase Transitions in Individual Nanomagnets

Inauguraldissertation

zur
Erlangung der Würde eines Doktors der Philosophie

vorgelegt der
Philosophisch-Naturwissenschaftlichen Fakultät
der Universität Basel

von

Andrea Mehlin

aus Rheinfelden, Deutschland

Basel, 2017

Genehmigt von der Philosophisch-Naturwissenschaftlichen Fakultät
auf Antrag von

Prof. Dr. Martino Poggio

Dr. Thomas Mühl

Basel, den 20.06.2017

Prof. Dr. Martin Spiess
Dekan

It always seems impossible,
until it is done.

Nelson Mandela
(South Africa, 1918 - 2013)

Contents

Nomenclature

List of Symbols

Symbols used in this dissertation are reported in order of appearance. Those marked in bold fonts represent vectors.

Symbol	Units	Description
w	m	width of a cantilever
l	m	length of a cantilever
m_e	kg	effective mass of a mechanical resonator
$x(t)$	m	time-dependent displacement function
Γ	kg s^{-1}	intrinsic dissipation
k	N m^{-1}	spring constant
F	N	sum of driving and thermal force of a cantilever
m_{tot}	kg	total cantilever mass
τ_m	Nm	module of the magnetic torque
l_e	m	effective length
θ_c	deg	angle of the cantilever's free end with respect to the applied magnetic field
x	m	position of the cantilever's free end
n	-	index of the vibrational mode
F_{min}	N	minimal detectable force
k_B	J/K	Boltzmann constant
T	K	temperature
B	Hz	measurement bandwidth
f_0	Hz	fundamental cantilever frequency
Q	-	quality factor
t	m	thickness of the cantilever
E_y	Pa	Young's modulus of the material
ρ	kg m^{-3}	mass density of the material
x_{osc}	m	cantilever's oscillation amplitude
Δf	Hz	frequency shift of the cantilever
Δm	kg	change of the cantilever's mass

ω_0	Hz	fundamental angular frequency
λ	m	laser wavelength
c	-	correction factor
$\mathbf{H}$	A m^{-1}	applied magnetic field vector
$\boldsymbol{\mu}(\boldsymbol{H})$	J T^{-1}	magnetic moment of the sample
E	J	total energy of the cantilever with a magnetic sample attached
E_m	J	magnetic energy
$\tau_y(\theta_c)$	Nm	torque in $\hat{y}$ direction as a function of the cantilever's deflection
k_m	Nm^{-1}	magnetic spring constant
F_m	N	magnetic driving force
ω_m	Hz	angular resonance frequency in presence of a magnetic interaction
$\Delta\omega$	Hz	change of the angular frequency
$x(\omega)$	m	displacement response as a function of the angular frequency
$\tilde{x}(w)$	m Hz^{-1}	Fourier transform of the displacement
$\tilde{F}_m(\omega)$	n Hz^{-1}	Fourier transform of the magnetic driving force
$x(t)$	m	time-dependent displacement function
μ_0	N A^{-2}	vacuum permeability
V	m^3	volume of the magnetic sample
K	J m^{-3}	crystalline anisotropy
M_s	A m^{-1}	saturation magnetization
$\mathbf{M}$	-	net magnetization over the sample
θ_m, ϕ_m	deg	angles describing the orientation of the net magnetization
$\mathbf{m}$	-	orientation of the sample
θ_n, ϕ_n	deg	angles describing the orientation of the sample
M_z	T	magnetization pointing in z direction
$\tilde{x}(\omega_m)$	V	amplitude response as a function of ω_m
$\mathbf{H_{AC}}$	T	AC magnetic field
$\bar{\boldsymbol{\chi}}_{\boldsymbol{AC}}$	-	AC magnetic susceptibility tensor
F_p	N	driving force of the piezo-electric actuator
Γ_0	kg s^{-1}	intrinsic cantilever dissipation
$\Gamma_m(H)$	kg s^{-1}	magnetic dissipation
T_1	s	magnetic relaxation time
μ_B	J T^{-1}	Bohr magneton
E_{tot}	J	total magnetic energy
E_Z	J	Zeeman energy
E_{ex}	J	symmetric exchange energy

E_K	J	anisotropy energy
E_{ms}	J	magnetostatic energy
J_{ij}	J	exchange integral
$\mathbf{S_i}, \mathbf{S_j}$	-	spin vectors
A	J m^{-1}	exchange coupling parameter
T_c	K	Curie transition temperature
M_r	A m^{-1}	remanent magnetization
H_c	T	coercive field
$\mathbf{H}_{dm}$	A m^{-1}	demagnetization field
$\mathbf{H}'$	A m^{-1}	total, internal magnetic field
$D_\parallel$, $D_\perp$	-	demagnetization factors
β	-	ratio between inner and outer radius of a tube
r_i	m	inner radius of a tube
r_o	m	outer radius of a tube
d_o	m	outer diameter of a tube
L	m	length of the sample
λ_{ex}	m	spin exchange length
$r_c(\beta)$	m	critical radius depending on β
E_{DM}	J	asymmetric exchange energy
$\mathbf{D_{ij}}$	J	Dzyaloshinskii vector
H_{DM}	J	Hamiltonian describing the asymmetric exchange energy
a	m	crystal lattice constant
L_D	m	skyrmion lattice constant
w_D	J	DMI energy
t_s	m	shell thickness
$\hat{n}$	-	direction of the long axis of the NT
$\hat{n}_T, \hat{n}_B$	-	orientation of the plane in which the NT ends lie
θ	deg	angle of the magnetic field direction in the xz-plane
ϕ	deg	angle of misalignment from the xz-plane of the magnetic field direction
α_T, α_B	deg	angle of the top/bottom end of NT
$\hat{k}$	-	propagation direction of the X-rays
I_{XMCD}		normalized XMCD signal
$\sigma^{\pm}$	-	X-ray chirality
$I_\sigma^{\pm}$		emission intensity of the photoelectrons
α_{max}	deg	maximum angle at which the skyrmion lattice is still formed
K_u	J m^{-3}	intrinsic uniaxial anisotropy
k_u	A^2 m^{-2}	effective uniaxial anisotropy

M	A m^{-1}	absolute value of the sample magnetization
D	J m^{-2}	DMI constant

List of Acronyms

Acronym	**Description**
MRI	magnetic resonance imaging
NW	nanowire
NT	nanotube
DCM	dynamic cantilever magnetometry
CM	cantilever magnetometry
MFM	magnetic force microscopy
SEM	scanning electron microscopy
TEM	transmission electron microscopy
SEMPA	spin-polarized low energy microscopy
PEEM	photoemission electron microscopy
TXM	transmission X-ray microscopy
STXM	scanning transmission X-ray microscopy
XAS	X-ray absorption spectroscopy
SQUID	superconducting quantum-interference device
DC	direct current
MOKE	magneto-optical Kerr effect
PLL	phase-locked loop
FEM	finite element model
PD	photodetector
AC	alternating current
MRFM	magnetic resonance force microscopy
RCM	resonant cantilever magnetometry
FPGA	field-programmable gate array
FM	ferromagnetic
XMCD-PEEM	X-ray magnetic dichroism photoemission electron microscopy
DW	domain wall
DMI	Dzyaloshinskii-Moriya interaction
SANS	small-angle neutron scattering
AFM	atomic force microscopy
FIB	focused ion beam
PLCM	phase-locked cantilever magnetometry

RF	radio frequency
LTEM	Lorenz transmission electron microscopy
THE	topological Hall effect
CVD	chemical vapor deposition
FWHM	full-width at half-maximum
FC	field cooled
ZFC	zero field cooled
P	critical point of skyrmion lattice formation

Introduction

Various kinds of magnetic materials are present in our everyday life and can be found embedded in applications in various fields. For instance, magnets build the basis of audio speakers, they are an ingredient of the contrast agent in medical examinations by magnetic resonance imaging (MRI), or are used in hard discs, to mention a few of them. Besides the high amount of magnetic materials implemented in applications, a continuous and large interest is present in ongoing research to study their behavior in different types, compositions, and shapes.

Interesting studies are motivated by the potential use of magnetic nanoparticles in biological and biomedical applications [1, 2], magnetic samples for magnetic sensing [3], or for high resolution imaging [4–6] and as logic devices [7]. Furthermore, in the last few years a proposal to improve magnetic data storage by increasing the density of information with a rapid access by designing a race track memory has received a lot of attention [8]. For this proposal and also for many other ongoing research projects focusing on magnetic storage media, nanowires (NWs) and nanotubes (NTs) are promising structures. Due to their shape, they would be easier to implement compared to bulk samples and also their quality is higher due to less stacking faults and impurities. In addition, the relative small size of those structures increases the potential for higher information density. NTs are also of interest because of the formation of flux-closure configurations, which produce a minimal stray-field and therefore reduce the interaction to neighbouring structures [9]. The information in NTs could be transmitted by the control of domain wall motion [10].

Another promising carrier of information in high density magnetic storage media are the 2009 experimentally discovered magnetic skyrmions [11–13]. They have a number of favorable properties, including their stability, nanometer-scale size, and the ultra-low electrical current density required to move them [14]. The threshold for moving these vortex-like spin configurations is only around 10^6 A/m^2, compared to the 10^{12} A/m^2 required to move a domain wall [15, 16], allowing potential skyrmion-based memory devices to count on negligible ohmic heating. Whether skyrmions are suitable as nanobits and therefore could increase the density of information in memory devices depends on several aspects: the thermal stability range, the size, and the external controllability by electrical fields or small electric currents [14,17–19].

Before embedding any kind of magnetic material into applications, a fundamental knowledge obtained both experimentally and theoretically is necessary. Finding a suitable technique for the study of magnetic materials, especially for nano-scale samples, is a challenge. Conventional techniques are often not sensitive enough to measure the magnetic moment of single nano-scale or small micron-scale objects. Due to that, many techniques work on ensembles, thereby resulting in an averaging over various, inhomogeneous magnetic objects. Those measurements suffer from the complication caused by random orientation, varying sizes [20] and interactions between neighboring objects as well as by the presence of residuals on the substrate remaining from the growth process. On the contrary magnetic imaging methods provide the possibility of investigating single objects. On the other hand, sample preparation like a thinning process are often required for such measurements, which can influence the properties of materials significantly. Another option for the research of magnetic materials is the measurement of magneto-resistance. Different sized, individual samples can be measured, as long as they are conductive and it is possible to electrically contact them. Nevertheless the process of contacting can cause local changes of the sample and impurities.

A pioneering technique for the investigation of individual nanostructures is dynamic cantilever magnetometry (DCM) [21–25]. It is suitable for different shapes of the sample, various orientations of applied magnetic field can be probed, a big range of temperatures can be covered and even insulators can be studied with this non-invasive method. By choosing the mechanical oscillator according to the sample size and properties, a big sample-size range can be covered. DCM takes advantage of the high quality and sensitivity of modern nano-sized mechanical oscillators. These are currently employed in a wide range of applications as sensitive detectors of masses and various kinds of forces [26]. For instance, using a cantilever, the magnetic force of a single electron spin was measured [27]. Cantilevers were used in magnetic torque based measurements, for the investigation of various materials like different ferromagnetic nanostructures in the shape of thin films [28], nanotubes [23,25,29–31], NWs and particles [32], a superconducting ring [22] and normal metallic rings [21], and superconducting crystals [33].

In this thesis, we demonstrate the use of DCM for providing both complementary and new information about the properties of novel and also well-known magnetic materials. First we present the investigation of ferromagnetic NTs. Dynamic studies of such NTs are limited and so far did not show indications of the promising flux-closure configurations. Here we present the nucleation and disappearance of individual vortices in ferromagnetic NTs depending on the aspect ratio of the tubes and the magnetic field direction.

The presented results are in a good agreement with numerical simulations which we performed additionally and theoretical predictions [34]. In addition, we used for the first time DCM for the investigation of materials containing magnetic skyrmions. We present our contribution to the promising research on magnetic skyrmions, by showing a stabilization of the skyrmion lattice phase in single-crystal MnSi NWs over a surprisingly big range of temperature and for a certain magnetic field direction which was previously observed only for thin film samples. Furthermore we observe a stability of the skyrmion lattice in GaV_4S_8 for a unexpectedly large range of applied magnetic field directions.

The structure of this thesis is described in the following. In chapter 1 we briefly introduce different techniques suitable for the investigation of magnetic samples and we focus afterwards on cantilever magnetometry (CM). Thereby we illustrate the needed technical components: the cantilever and its properties, also analyzed through numerical simulations; we further describe the optical fiber interferometer, which was used for the read-out of the cantilever's motion. Furthermore we derive equations describing the different variations of magnetic torque based measurements, explaining the sensitivity and suitability of the variations depending on the measurement circumstances.

Chapter 2 introduces the basic concepts of magnetism. We describe the energy contributions characterizing magnetic microstructures and the material properties. The main focus is on the materials investigated during this work, providing the theoretical background for the subsequent experimental chapters. We provide a detailed description about ferromagnetic NTs and the magnetic equilibrium states caused by their shape and aspect ratio. Then we describe the properties of magnetic skyrmions, under which conditions they occur, and the mechanism of stabilization of this nontrivial spin structures.

In the following chapters the experimental results obtained by DCM measurements are presented. In chapter 3 we present the investigation of the magnetic states of CoFeB NTs depending on their aspect ratio. Besides the study with DCM, we show also the results of resonance cantilever magnetometry measurements and images obtained by X-ray magnetic dichroism photoemission electron microscopy.

Chapter 4 describes the results of the study of MnSi NWs. We observe a stabilized skyrmion lattice phase from around 29 K down to at least 0.4 K in single MnSi NWs. Thereby the stability of the skyrmion lattice depends on the orientation of the NW with respect to the applied magnetic field.

The results of the study of GaV_4S_8 are described and discussed in chapter 5. We study the stability of the skyrmion lattice in GaV_4S_8 depending on the magnitude and the orientation of the applied magnetic field. The skyrmion lattice stability depends on the uniaxial anisotropy present in these materials. In addition we compare our experimental findings with theoretical predictions.

The final chapter 6 provides a conclusion of this thesis, by summarizing the main results and giving an outlook on future experiments which could follow up on the research reported in this work.

1 Cantilever Magnetometry

Investigation of magnetic materials in various compositions and geometrical configurations attracts continuous interest in the scientific community. In order to characterize these materials various experimental methods are available. The suitability of a particular technique for a specific sample of interest depends on several different factors, like the sample size, physical conditions which are required from the sample, or time and spatial resolution, to mention just a few of them.

This chapter is dedicated to the technical aspects regarding the investigation of magnetic samples. The first part of this chapter gives an overview of suitable techniques for the characterization of magnetic materials. Afterwards the focus is on cantilever magnetometry (CM). In detail are discussed the cantilever as mechanical oscillator, its displacement detection, relevant mathematical derivations for CM, variations of the technique and numerical calculations used for the simulation of our measurements.

1.1 Techniques for the Investigation of Magnetic Materials

Various techniques are in use for the investigation of the surface of magnetic materials. In particular, different kind of magnetic imaging techniques are mainly suitable for samples in the form of thin films, since their sensitivity is reduced to the surface or to the near-surface region of the sample. In this section we provide an overview of the main available techniques.

1.1.1 Magnetic Force Microscopy

A scanning-probe technique used for the study of magnetic samples is magnetic force microscopy (MFM), which investigates the interaction between a magnetic tip attached to a sensitive cantilever and the sample. For imaging the sample, the tip is placed close to the surface and scanned above it. In this way the stray field of the sample interacts with the magnetic tip and therefore affects the cantilever. Thereby the force or the force gradient for each position is recorded [35]. The resolution of MFM depends on the tip size and the tip-sample distance and for example a resolution in the order of 10 nm was obtained by imaging domain walls [36]. In order to achieve atomic resolution, theoretically speaking, an atomically sharp tip is required, which scans the sample in the non-contact mode at a distance of about interatomic distances. Therefore cantilevers with high spring constants are needed in order to avoid jump-to-contact events, and the single atom at the tip needs to have a stable magnetic moment, just to mention some of the complications [37]. An advantage of this technique is that no special sample preparation nor special environmental conditions are necessary.

1.1.2 Electron Microscopy

Out of the big group of electron microscopy diverse techniques are suitable for the investigation of magnetic materials and in this paragraph a brief overview of this family is given by using [38] as main reference; additional references are specified whenever necessary. Electron microscopy is very sensitive even to small changes in the local magnetization. It provides high contrast and spatial resolution down to about 1 nm. The magnetic contrast is due to the phase changes or phase shifts induced by the magnetic fields in the sample when the electron wave is crossing. The various techniques of electron microscopy can be sectioned into two subgroups: scanning electron microscopy (SEM) and transmission electron microscopy (TEM).

In the case of SEM a well focused electron beam is used for scanning above the surface. One distinguishes between two types of SEM. One type detects the secondary electrons. The resulting contrast is due to the fact that these low energy secondary electrons with an energy up to 50 eV are deflected by the magnetic stray field above the surface when they eject from the sample, resulting in a surface sensitive method. In the other case the contrast is due to the detection of the backscattered electrons. Electrons with a usual energy of above 30 keV deflect due to the magnetic flux density depending on the local magnetization, which results in the backscattered electron contrast. Since no stray fields are necessary this technique is suitable for studying soft magnetic materials with a low anisotropy. The possible spatial resolution is just about 0.5 μm though a depth of 15 μm can be reached. A variation of SEM is the scanning electron microscopy with polarization analysis (SEMPA) where the magnetic contrast is obtained by the detection of the spin polarization of the secondary electrons [36]. Spin dependent scattering increases and improves the contrast with decreasing electron energies. SEMPA provides high spatial resolution and vector magnetization information about the sample surface.

Different TEMs techniques are in use for the study of magnetic materials since more than 50 years. Depending on the material and the specific method the thickness of the samples is limited between 50 Ångstrom up to a few thousands Å [36]. The most frequently used kind of TEM for the study of magnetic samples is the Lorentz TEM. This special TEM embeds two different modes, the Fresnel mode which provides contrast along domain walls and the Foucault mode which is sensitive to the domain itself. A spatial resolution in the order of 2 nm can be reached, thought the measurement is the average of the entire sample thickness. Hence just thin samples, below a thickness of 300 nm, are suitable for high resolution studies [36]. Plenty of other variations of electron microscopy is available for the investigation of magnetic materials like electron holography, spin polarized low energy microscopy, differential phase contrast microscopy, to name a few of them.

1.1.3 Neutron Scattering

A very powerful experimental tool for the investigation of magnetic materials is neutron scattering. It provides information for instance about spin structures, magnetic-excitation spectra and dynamics of magnetic phase transitions [39]. Since neutrons have no electrical charge the interaction with the sample is weak and therefore they penetrate deep into the sample. Due this property neutron scattering can be used for the study of the inner structure and dynamic processes. This technique is not sensitive to electric fields, external charges or irregularities at the surface layers and allows measurements in different kind of environments like magnets, cryostats or pressure cells [39]. Neutron sources are difficult to focus and due to that they are weak sources compared to laser or synchrotron sources, and in order to compensate for the low signals large samples of about a few milligrams are needed [40]. The second drawback is that several elements like Cadmium and Gadolinium absorb the neutrons, thus not providing further scattering information [40].

1.1.4 X-ray Scattering

Another suitable imaging technique is X-ray scattering. One distinguishes between soft X-rays (between ca. 100 eV to 2000 eV) and hard X-rays [41]. Different types of X-ray-based microscopes are in use, like photoemission electron microscope (PEEM), transmission X-ray microscope (TXM) or scanning transmission X-ray microscope (STXM), to mention some of them [42]. These kinds of magnetic imaging are mainly based on X-ray absorption spectroscopy (XAS) which investigates element-specific the density of the unoccupied electronic states [43]. XAS can be for example operated either in total electron yield mode or in transmission mode. Changing between these two modes offers the possibility to vary the sampling depth between a few nm up to 100 nm providing the possibility to probe not only the surface but also bulky materials [42]. A spatial resolution in the order of 10 nm can be achieved with soft X-ray-based imaging [44]. Depending on the sample and the required conditions different types of X-ray based techniques have advantages over others. In case an applied magnetic field is needed, STXM or TXM can be used, with the drawback that the sample must be grown on a thin SiN membrane. The PEEM for example is suitable for single crystal, very thin or diluted samples. If low temperatures are necessary the lensless imaging techniques are more useful; they have also the advantage that their spatial resolution is not limited by the optical setup [42].

1.1.5 Superconducting Quantum Interference Device

A very sensitive magnetometer is the superconducting quantum interference device (SQUID). The direct current (DC) SQUID is suitable for the detection of weak magnetic fields down to 10^{-15} T by coupling the magnetic flux into the SQUID loop [29].

A SQUID in combination with a vibrating-sample magnetometer offers the possibility to detect the hysteresis loops of magnetic objects with a high precision [45]. In this combination, the sample vibrates between two pick-up coils which are placed in an external magnetic field. By coupling the coils inductively to a SQUID, flux variations caused by the movement of the magnetic object can be detected.

Another possibility is to modify the fabrication, by making a SQUID on the tip of a pulled quartz tube provides the possibility to reduce the size of the superconducting loop, therefore the sensitivity increases, and the changed geometry allows to scan close above the surface of the sample [46]. The disadvantage of this very sensitive technique is that the sensitivity is dropping for increasing applied magnetic fields [29]. Furthermore the measurements are restricted to low temperatures due to the necessary superconductivity of the SQUID. Suitable materials and their critical temperatures for a scanning SQUID are Nb with a T_c of about 8.7 K and Pb of $T_c \approx 7$ K [46]. For standard SQUIDs the temperature range is extendable. In 1991 a standard SQUID working up to 77 K was produced by the use of the high temperature-superconductor YBCO [47]. The critical temperature for thermally evaporated YBCO films is about 87 K [48].

1.1.6 Magneto-Optical Kerr Effect

Another well established method is the investigation through the magneto-optical Kerr effect (MOKE). MOKE is based on the effect that the polarization of light is changing when it reflects from a magnetic material due to the spin-orbit interaction and the exchange coupling [49, 50]. MOKE is used for the investigation of individual nanostructures as well as assemblies of nanostructures whereat a reflective surface is needed. This surface-sensitive technique has a penetration depth of ∼25 nm.

1.1.7 Measurement of Magneto-Resistance

Besides imaging methods also non optical methods are available for the study of magnetic samples. A wide spread method is the measurement of magneto-resistance. In the measurement the change in the electrical resistance as a function of applied magnetic field is detected [51]. A big advantage of this method compared to others is that it is suitable for the investigation of NWs [52], thin films [53], multilayers [54] or bulk [55] materials as long as it is possible to contact the sample and the sample itself is conductive.

Several other techniques or variations of the above mentioned techniques are available and in use for the study of magnetic materials. Depending on the sample size, sample properties, and needed environmental conditions, some techniques have advantages compared to others. Often in order to obtain a complete or good understanding of the sample of interest one characterization method is not enough. For example it is a challenge for most of the available techniques to investigate the dependence of material properties on the size and the shape of a sample. The influences of the geometry on the physical behavior is in many cases not negligible. In the following the focus will be on CM, a method which provides the possibility to investigate samples independent of size, shape, temperature, and conductivity.

1.2 The Tools of Cantilever Magnetometry

Torque-based magnetometry is a technique suitable for various kinds of samples. It has for example been used for the study of different ferromagnetic nanostructures in the shape of thin films [28], nanotubes [23, 25, 29–31], NWs and particles [32], for the study of a superconducting ring [22] and normal metallic rings [21], for superconducting crystals [33], and to explore the skyrmion phase in single-crystal NWs [24].

All these different magnetometry experiments have several features in common. A magnetic sample is attached to a resonator and positioned in an external magnetic field. It results in a torque produced by the magnetic moment of the sample, which changes the properties of the resonator and hence the detected signal. The essential components are a magnetic sample, a mechanical oscillator, and a readout mechanism. Furthermore of course some technical and electrical equipment depending on the properties of the sample and the type of experiment like a magnet, cryostat, and so on are needed. The technical requirements and information about the used setups are described in appendixes A and B. A detailed description of the studied magnetic structures is given in the next chapter. Hence the focus in this chapter is on the resonator and the readout mechanism. The mechanical oscillator is an important component and has a strong influence on the sensitivity of the measurements. The sensitivity is also affected by the kind of torque-based method which is chosen for the investigation of the sample. The different modes introduced in section 1.3 offer access to different parameters, like the displacement or the frequency of the resonator. Depending on the extracted value, different readout mechanisms are suitable. For example, a capacitive readout is able to determine the displacement [56]. The detection of the oscillation frequency can be realized for instance with a lock-in amplifier, a gated timer, a phase-looked loop (PLL), or a frequency counter [32,57,58]. We use for the readout of the cantilever frequency an optical fiber interferometer which is described in the following. Apart from this the focus is initially on the properties of mechanical oscillators, especially in the cantilever geometry.

1.2.1 The Cantilever

Mechanical resonators find application in different areas. Especially nanomechanical resonators are very suitable sensors for the detection of mass and different kind of forces [26]. In case of magnetic-torque based measurements, a mechanical oscillator finds its use mainly as a beam clamped on one side and free on the other, in the so-called cantilever configuration. A cantilever has typically a cross-sectional area much smaller than the length. Therefore it represents a sensor with a low spring constant and typically it has also a high quality factor. These properties make cantilever suitable for precise experiments [59].

The following section gives attention where the width is much smaller than the length $w \ll l$, the cross-section is uniform throughout the length and assuming that only small deflections are performed. Taking these assumptions into account and following references [60] and [61], the motion of a cantilever at its free end and in its fundamental mode can be described by the equation of a damped simple harmonic oscillator:

$$m_e\ddot{x} + \Gamma\dot{x} + k_0 x = F, \tag{1.1}$$

where m_e, Γ, and k_0 are the effective mass, the intrinsic dissipation, and the spring constant of the fundamental mode of the resonator; $x(t)$ is the displacement as a function of time and F is the sum of a driving and a thermal

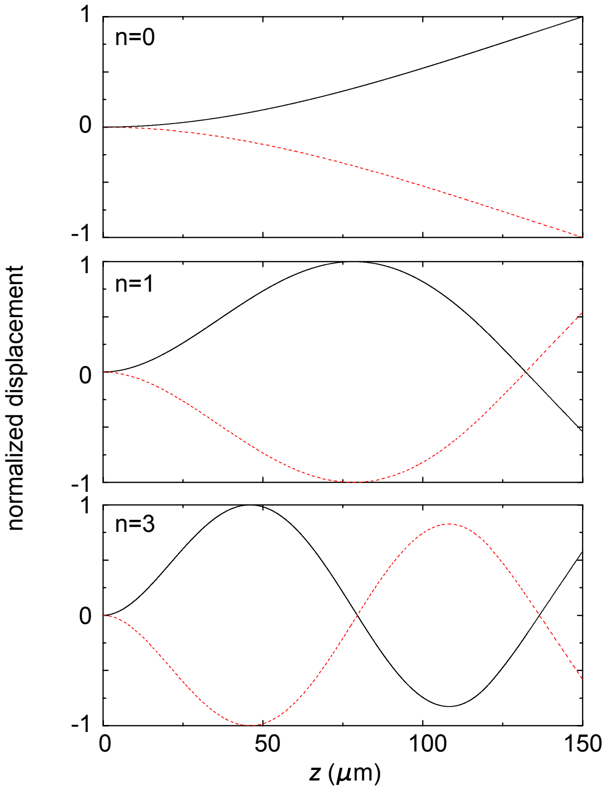

Figure 1.1: Normalized mode shapes for the first three flexural modes for a 150 μ long cantilever. In solid (black) and in dashed (red) lines are shown the positive and the negative maximum displacements. The displacement x is normalized so that the maximum is 1. We note, that the n = 2 mode for this cantilever is a torsional mode and it is not shown here, see Fig. 1.4. The plots are made with finite element model, for more details see Sec. 1.2.1.1.

force. The effective mass is a concept used due to the fact that the mode shape is a non-linear function of the position [59]. The mode shape function of one of the used cantilevers for the first three flexural modes is plotted in Fig. 1.1. These mode shapes were obtained by numerical simulations, more details about the model and the resonator are given in section 1.2.1.1.

The effective mass can be calculated out of the potential energy of each mode separately, details are given in Refs. [59] and [60]. A more widely used quantity in this frame is the effective mass ratio. This parameter gives the ratio of the effective mass at the free end to the total mass m_{tot} and is independent of the mode. In case of a beam with a thin and uniform cross-section as for instance in the shape of a cantilever, the effective mass ratio is $m_n/m_{tot} = 1/4$ [59].

Apart from the effective mass, something else has to be taken into account to approximate a thin resonator as a damped simple harmonic oscillator. CM is based on the concept that a force is acting on the cantilever, which is due

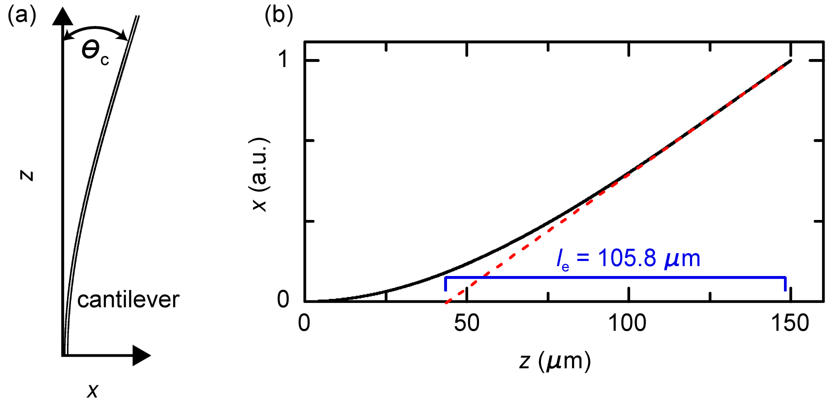

Figure 1.2: (a) Model of a vibrating cantilever in its fundamental mode with a tilting angle θ_C . (b) Fundamental mode of a 150-μm long cantilever (black) obtained by finite element calculations. The displacement x is normalized so that the maximum displacement is 1. The tangent (red) defines l_e by crossing the base line.

to the torque of the magnetic material (more details about the technique are given in the next section). Since the thermal force is in our case much smaller than the driving force, we neglect it during further derivations. Under the influence of the applied torque, the equation of motion is:

$$m_e\ddot{x} + \Gamma\dot{x} + k_0 x = \frac{\tau_m}{l_e}, \tag{1.2}$$

where τ_m is the module of the magnetic torque acting on the free end and l_e is the effective length. The concept of the effective length accounts for a non-linear shape of the vibrational modes, see 1.1. The angle of the tip of a vibrating cantilever with a displacement x is θ_C, see Fig. 1.2(a). In case of small-angle approximation, l_e can be calculated by determining the crossing point of the tangent to the tip of the cantilever with the base line [32,62]. The effective length to be determined for each mode separately. The determination of the effective length for the fundamental mode is illustrated in Fig. 1.2(b): for a 150 μm long cantilever $l_e = 105.8$ μm.

1.2.1.1 Finite Element Models of the used Cantilevers

Analytical description of the properties of nano-mechanical resonators is not always possible without resorting to approximations. For instance, the geometry is often approximated as a simple beam, which is often not applicable. In order to determine certain values, numerical simulations by finite element models (FEM) are helpful. In our case we use FEM for the calculation of the effective length. FEM calculations are done with a commercially available software (COMSOL Multiphysics).

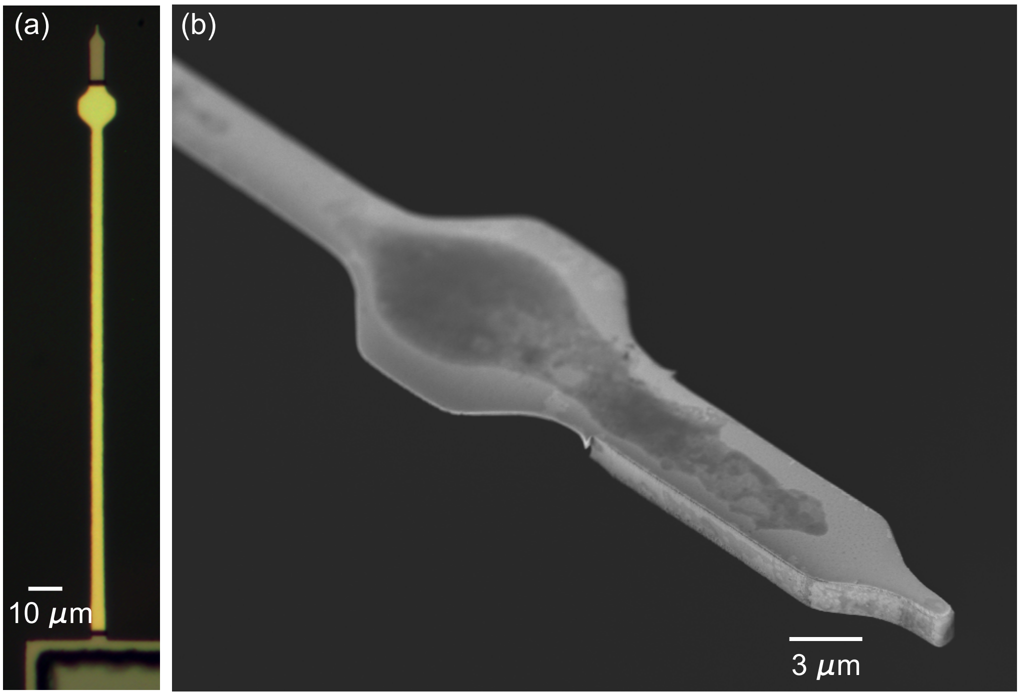

Figure 1.3: (a) An optical picture of an ultrasensitive Si 180-μm long cantilever which was used for the experiments described in chapter 3 and 4. (b) SEM of this lever with the focus on the mass-loaded tip and the paddle.

During the measurements two different types of single-crystal silicon (Si) cantilevers were used. The studies of the CoFeB NTs, Chap. 3, and the MnSi NWs, Chap. 4 were performed with ultrasensitive cantilevers of two different lengths. The cantilevers are respectively about 180 μm and 150 μm long, 4 μm wide, 135 nm thick, and have a 18 μm long and 1 μm thick mass at the tip. Close to the mass-loaded tip is a 12 μm wide paddle which acts as a reflective surface as part of the optical-fiber interferometer used for the detection of cantilever motion (Sec. 1.2.2). An example of a 180 μm cantilever is shown in Fig. 1.3. More specific details of each of the used cantilevers are given in the corresponding experimental chapters. The results of the FEM for a $150-\mu$m long ultra-soft cantilever are shown in Fig. 1.4. Presented are the first four resonance modes. The n = 2 mode is a torsional mode which is due to the asymmetrical position of the mass along the shaft. The other three modes are simple flexural modes. For this cantilever the effective length of the fundamental mode calculated from the FEM is $l_{e,150} = 105.8$ μm.

The mode shapes of the first four resonance modes for a 180-μm long cantilever show the same behavior as those presented for the 150-μm resonator. The n = 2 mode is as well a torsional mode and the others are flexural. The $l_{e,180} = 126.3$ μm determined from the FEM of the fundamental mode.

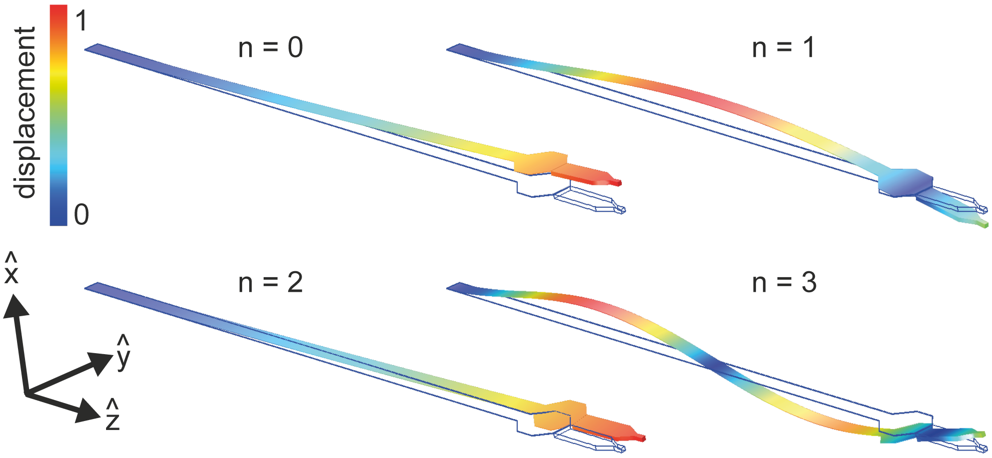

Figure 1.4: The lowest four modes calculated by FEM of an ultra-soft 150-μm long cantilever. Each mode is separately normalized so that the maximal displacement is 1.

For the investigation of GaV$_4$S$_8$, present in Chap. 5, a commercial cantilever (Nanosenors(TM) TL-Cont) was used. These tipless resonators consist of an about 440 μm long, 50 μm wide, and 2.3 μm thick shaft. The shaft ends with a triangle which prolongs the shaft by about 25 μm, see Fig. 1.5. Further details about the used cantilevers are given in the corresponding chapters. The first four modes of the resonator are presented in Fig. 1.6 which illustrates the displacement depending on the position. For this cantilevers the first three modes are flexural and n = 3 is a torsional mode. The torsional mode is caused by the large width compare to the thickness [60]. For this commercial cantilever, l_e of the fundamental mode is 340.0 μm.

1.2.1.2 Sensitivity

Nanomechanical resonators are in use for measuring small forces in different applications. An aim of this research branch is to be able to detect as small as possible forces. The fundamental limits are therefore a relevant information. Calculations performed by Yasumura *et al.* [63] show that the thermomechanical noise imposes the detection limit of small forces. If the cantilever is in thermal equilibrium with the environment, thermomechanical noise is induced. The minimal detectable force per bandwidth B for an amplitude measurement is defined by the following equation [63]:

$$F_{min} = \frac{F'_{min}}{\sqrt{B}} = \sqrt{\frac{2k_0 k_B T}{\pi f_0 Q}}, \tag{1.3}$$

where k_B is the Boltzmann constant, T is the temperature, f_0 is the fundamental frequency, and Q is the quality factor. For a cantilever with rectangular

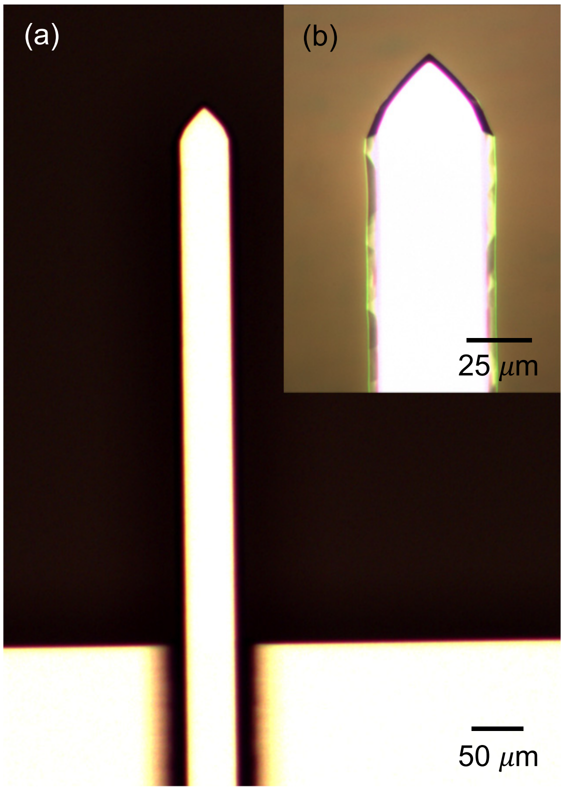

Figure 1.5: (a) An optical picture of the commercial cantilever (Nanosensors(TM) TL-Cont) and (b) a zoom in on the tip. This type of resonator was used for the experiment described in chapter 5.

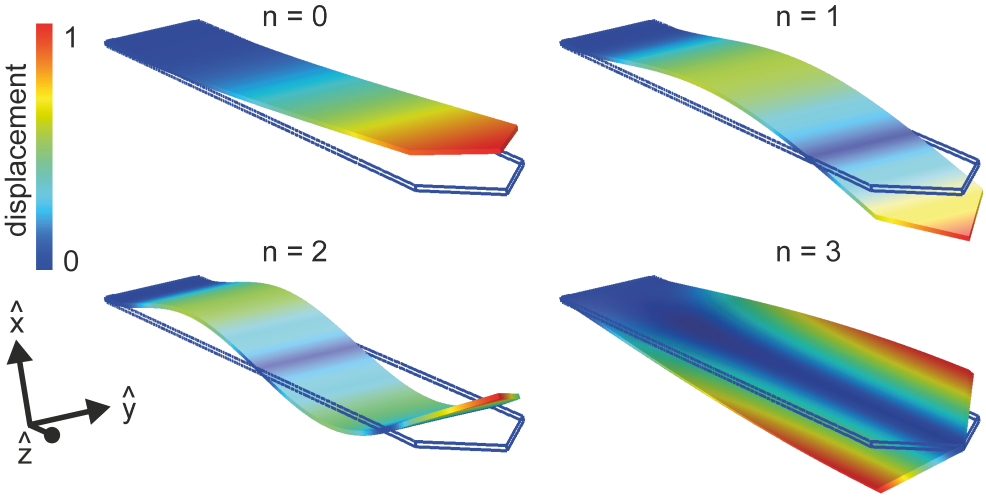

Figure 1.6: The first four modes of the commercial cantilever (Nanosensors(TM) TL-Cont). Each mode is separately normalized so that the maximal displacement is 1.

cross-section, the previous equation can be rewritten to express the minimal detectable force in terms of the cantilever‘s dimensions:

$$F_{min} = \sqrt{\frac{wt^2 k_B T}{lQ}} \sqrt[4]{E_y \rho}. \tag{1.4}$$

Here w is the width, t is the thickness, l is the length, E_y is the Young's modulus, and ρ is the mass density of the cantilever. According to this expression, in order to improve the sensitivity, respectively to reduce the minimal detectable force, T can be reduced. Furthermore, in terms of changing the shape of the cantilever, by reducing the width and the thickness and increasing the length of a resonator, the sensitivity can be increased. However the minimal detectable force can only be reduced if Q can be conserved. Q depends on the material, and surface effects will have a stronger impact for thinner resonators [63], thus reducing Q.

In the following we calculate the minimal detectable force for a cantilever which we typically use. For example, the $180-\mu$m long cantilever used in chapter 4 for NW1, has the following properties: $k_0 = 37\mu$N/m, $f_0 = 2062.8$ Hz and $Q = 4.1 \times 10^4$. By using equation (1.3) and assuming T = 4 K, we obtain $F_{min,180} = 3.9$ aN/$\sqrt{\text{Hz}}$. In our case, the detected signal is produced by a torque acting on the cantilever's free-end. We obtain from (1.3) the minimal detectable torque:

$$\tau_{min} = l_e \sqrt{\frac{2k_0 k_B T}{\pi f_0 Q}}, \tag{1.5}$$

and with $l_e = 126.3\ \mu$m , see Sec. 1.2.1.1, we obtain $\tau_{min,180} = 0.5$ zN m/$\sqrt{\text{Hz}}$.

The previous equations describe the sensitivity for parameters of amplitude measurements. However, we detect during our studies the frequency, and in this case we measure the force derivative whose sensitivity is [64]:

$$\left(\frac{\partial F}{\partial x}\right)_{min} = \frac{1}{x_{osc}} \sqrt{\frac{2k_0 k_B T}{\pi f_0 Q}}, \tag{1.6}$$

where x_{osc} is the cantilever‘s oscillation amplitude. In terms of torque we obtain:

$$\left(\frac{\partial \tau}{\partial \theta_c}\right)_{min} = \frac{l_e}{\theta_c} \sqrt{\frac{2k_0 k_B T}{\pi f_0 Q}}, \tag{1.7}$$

For the concrete example of the $180-\mu$m cantilever, we used $x_{osc} \simeq 10$ nm and hence we can reach a sensitivity of: $(\partial F_{180}/\partial x)_{min} \simeq 0.4$ nN/m$\sqrt{\text{Hz}}$ and since $\theta_c < 0.01$ rad we obtain $(\partial \tau_{180}/\partial \theta_c)_{min} > 50$zN m/rad$\sqrt{\text{Hz}}$. Note that according to Sansa *et al.*, the detection limit of frequency measurements described by the previous two equations is rarely reached [65]. They claim that on average the signal was two orders of magnitude higher as the calculated limit. This is suppose to be caused by frequency fluctuations.

1.2.1.3 Change of the Resonance Frequency due to an Additional Mass

Nanomechanical resonators react with high sensitivity to a mass variation by changing the resonance frequency. Due to this, they are useful tools for mass sensing applications [66, 67]. By detecting the change in the resonance frequency a resolution down to 1.7×10^{-24} g, which equates the mass of a proton, was achieved with a doubly clamped carbon NT [68]. When using a cantilever for investigation of magnetic materials, typically a sample is attached to its free end, which means that, depending on the size and density of the material, a significant amount of mass is added. Therefore the cantilever's resonance frequency change relevantly; in this context it is advisable to avoid shifting the resonance frequency towards the region of low frequency noise.

In order to approximate the frequency shift Δf induced by an additional mass Δm, the description of Ekinci *et al.* [67] is followed in this paragraph. The expression given below for describing the effect of an additional mass on the resonance frequency is based on the assumption that $\Delta m \ll m_e$ and as a consequence Q and k_0 do not change significantly. Therefore:

$$\Delta m \approx \frac{\partial m_e}{\partial \omega_0} \Delta \omega_0, \tag{1.8}$$

where ω_0 is the fundamental angular frequency. Since we assume that k_0 is unchanged, by using $m_e = \frac{k_0}{\omega_0^2}$, we obtain:

$$\Delta m \approx -\frac{2m_e}{\omega_0} \Delta \omega_0. \tag{1.9}$$

Using $\omega_0 = 2\pi f_0$ and solving for Δf_0, it results in:

$$\Delta f_0 \approx -\frac{f_0}{2m_e} \Delta m. \tag{1.10}$$

In our case, depending on the sample size, the assumption that $\delta m \ll m_e$ is often not fulfilled, so the properties of the cantilever change, resulting that k is not constant anymore. However for a first, rough estimation, in order to decide which cantilever is suitable for a certain sample, (1.10) is sufficient.

A change in the frequency of the cantilever can be induced by different things. A second source which also has to be considered during the preparation

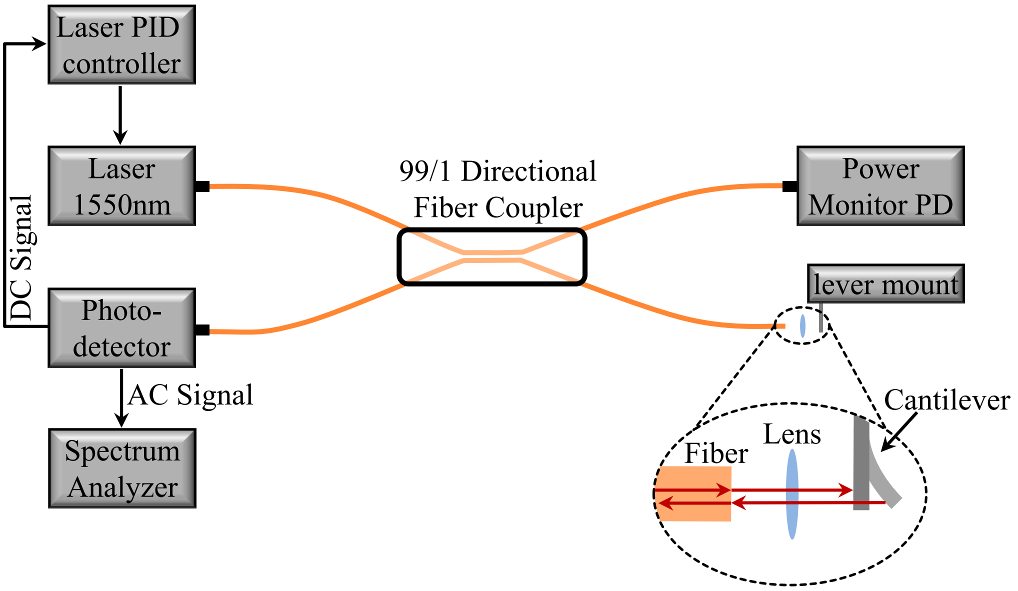

Figure 1.7: Schematic of the fiber-optic interferometer included in our experimental setups. A detailed description is given in the text.

of a sample is the frequency shift due to the magnetic torque of the attached sample. It is the desired effect for this kind of measurements, but in some situations it could be a problem for the stability of the measurement, if the shift induced by the magnetic torque is too big. Or, the other way round, if the torque is too weak, no frequency shift can be detected. So, depending on the sample, a stiffer or a softer cantilever is needed. Δf depending on the magnetization of the attached sample can be approximated by (1.37) and more details are given in section 1.4.

1.2.2 Displacement Detection

The readout of the displacement of the cantilever during our measurements is realized by the use of an optical-fiber interferometer, which is described in the following section. This optical detection technique is based on a description made more than 30 years ago by Drake and Leiner [69], which was a few years later improved by Rugar et al. [70, 71].

The interferometer configuration implemented in our systems is sketched in Fig. 1.7. We couple the coherent light of a laser diode with wavelength (λ) of 1550 nm into an optical fiber. This fiber goes to one arm of a 2 x 2 single mode directional coupler with a coupling ratio of 99 to 1. Correspondingly, 99 % of the laser power is guided to a power monitor photodetector and only 1 % of its power remains for sensing the cantilever motion. The one percent of the laser power is directed through a fiber to the cantilever. This piece of

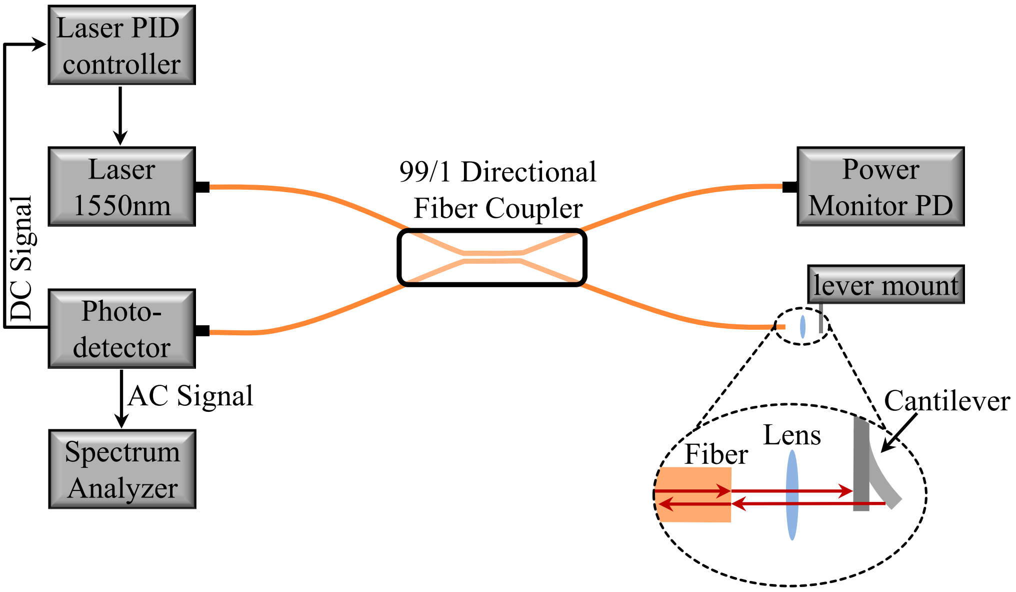

Figure 1.7: Schematic of the fiber-optic interferometer included in our experimental setups. A detailed description is given in the text.

of a sample is the frequency shift due to the magnetic torque of the attached sample. It is the desired effect for this kind of measurements, but in some situations it could be a problem for the stability of the measurement, if the shift induced by the magnetic torque is too big. Or, the other way round, if the torque is too weak, no frequency shift can be detected. So, depending on the sample, a stiffer or a softer cantilever is needed. Δf depending on the magnetization of the attached sample can be approximated by (1.37) and more details are given in section 1.4.

1.2.2 Displacement Detection

The readout of the displacement of the cantilever during our measurements is realized by the use of an optical-fiber interferometer, which is described in the following section. This optical detection technique is based on a description made more than 30 years ago by Drake and Leiner [69], which was a few years later improved by Rugar et al. [70, 71].

The interferometer configuration implemented in our systems is sketched in Fig. 1.7. We couple the coherent light of a laser diode with wavelength (λ) of 1550 nm into an optical fiber. This fiber goes to one arm of a 2 x 2 single mode directional coupler with a coupling ratio of 99 to 1. Correspondingly, 99 % of the laser power is guided to a power monitor photodetector and only 1 % of its power remains for sensing the cantilever motion. The one percent of the laser power is directed through a fiber to the cantilever. This piece of fiber ends shortly before a lens which is placed midway between the cleaved fiber end and the cantilever. The cleaved end and the cantilever form the cavity, and the collimating lens in between focuses the laser on the cantilever. From the cantilever as well as from the cleaved end of the fiber, the laser light reflects and reenters the sensing fiber. In order to obtain an optimal reflectivity in the cavity, the cleaved fiber end has a coating consisting of a thin layer of Si to match the reflection index of the cantilever [72]. This results out of the explanations and calculations done by Rugar *et al.* [70, 71].

For the detection of the displacement of the cantilever, interference between the reflected light from the cantilever and from the cleaved end is needed. Therefore the coherence length of the laser has to be longer of at least two times the cavity size [60]. This can be achieved with an appropriate design of the cavity, attuned to λ of the used laser. Since the coherence length in our setup is relatively long, we use a radio frequency modulation which reduces the coherence length, in order to avoid the formation of multiple cavities. Out of the interference of the two reflection signals, a displacement-dependent signal results. The displacement depending signal is guided back to the directional coupler and 99 % of its power is sent to a second photo detector (PD). The output of the PD is a voltage, which depends on the power of the signal.

The length of the cavity varies with the cantilever's displacement. In order to work with a constant sensitivity either the length of the cavity or the laser wavelength must be controlled [60]. In our setup, we use the DC signal of the PD for the feedback control of the wavelength-tunable laser source. A thermoelectric cooler tunes the laser temperature and with it the wavelength.

An oscillating cantilever is modulating the interferometer response at its mechanical resonance frequency and enables the measurement of the displacement. Apart from the information about the displacement, the alternating current (AC) signal of the PD is forwarded to a spectrum analyzer and is used for the determination of the cantilever's frequency. More details about the used and similar setups can be found in the following references [60, 70, 71], which were also mainly followed in this section.

An optical fiber interferometer has a high sensitivity, is mechanically stable, compact, has a good low frequency stability [71], and is relatively easy to implement. It can be used in ultrahigh vacuum and/or at low temperatures [70]. Due to these characteristics, optical fiber interferometers are suitable for the detection of the deflection of micro-sized mechanical oscillators [60]. The displacement readout of cantilevers via fiber-optical interferometers are in use for several different applications like, for instance, magnetometry measurements [23, 25, 29, 30], or magnetic resonance force microscopy (MRFM) [73, 74], in order to mention a few them. Furthermore it can be used for fundamental mechanical studies [75–77].

An optical interferometer is limited in its sensitivity by the PD shot noise [70]. Calculations for the same setup as used in chapter 4 were made by Montinaro [60]. Considering a laser power of 20 nW, the resulting sensitivity is in the order of 10^{-12} m $\mathrm{Hz}^{-1/2}$. The sensitivity can be improved by increasing the laser power. However, a higher laser power can cause a heating of the cantilever, which can be a problem for low temperature applications [78].

In all the measurements presented in this thesis, the displacement is not detected at the position of maximum deflection, due to practical reasons. Therefore it is not possible to measure the oscillation amplitude directly. In order to take that into account, we introduce a correction factor, which we call c-factor. The c-factor gives the ratio between the displacement of the cantilever at the tip to the position where the read-out takes place: $c = x_{tip}/x_{read-out}$. The values of the displacement at different positions are taken from the mode shape calculated by FEM. The read-out position in the case of the ultra-soft cantilever is the paddle, used as a reflective surface for the interferometer. For instance, the c-factors of the fundamental mode for the bare cantilevers introduced in the previous chapter are $c_{150} = 1.29$ for the $150-\mu$m long, $c_{180} = 1.24$ for the $180-\mu$m cantilever, and $c_{commercial} = 1.08$ for the commercial cantilever. In case of the commercial cantilever, we choose the read-out position to be where the rectangular shape finishes and the triangle prolongation starts. With the knowledge of the mode shape and the c-factor, the displacement at the tip can be calculated with the interferometer signal.

1.3 Cantilever Torque Magnetometry

In order to investigate the behavior of a sample by using a torque-based technique, the material of interest is attached to the end of a cantilever and positioned in an external homogeneous magnetic field, **H**. The magnetic moment of the sample $\boldsymbol{\mu}(\boldsymbol{H})$ modifies the behavior of the cantilever by producing a torque as described by the following equation:

$$\boldsymbol{\tau} = \boldsymbol{\mu}(\mathbf{H}) \times \mathbf{H} \tag{1.11}$$

Note that this equation is just valid if the magnetic moment is rigidly fixed with respect to the direction of the sample, consequently the direction of the magnetization sticks to the magnetic object and not to the cantilever oscillation. Using such torque-based technique, the average of the entire magnetic volume is investigated. Compared to other techniques, it has the advantage that it is a non-invasive method. For instance, due to the sample preparation or the measurement itself, no disturbance to the magnetization of the sample should occur as it may be the case for current-driven magneto-resistance studies or with other techniques.

According to Jang *et al.* [79] three different modes of CM can be distinguished: in the 1st mode the constant deflection of a cantilever in a static or a low-frequency magnetic field is detected, in the 2nd mode the cantilever's resonance frequency is measured in a static magnetic field, and in the 3rd mode, by applying a magnetic field at the resonance frequency of the cantilever, its resonance displacement is detected. In the following we discuss the characteristics of these three different modes in the mentioned order. In this work we refer to the 2nd mode as dynamic cantilever magnetometry (DCM) and we focus on this technique. By starting with the characteristics of the combined system of the nanomechanical resonator and a magnetic sample, we derive expressions to describe and differentiate the three different modes. We conclude this chapter with a description of how we use numerical calculations in order to simulate or measurements, see Sec. 1.7. The properties of the magnetic sample and of the nanomechanical resonator as independent objects are separately discussed in chapter 2 and section 1.2.1, respectively.

1.3.1 The Magnetic Torque

In this section we describe a system composed of a soft silicon cantilever and an individual magnetic nanostructure. The latter is attached with a nonmagnetic epoxy (G1) to the resonator‘s free end by the use of micromanipulators. The focus in the remaining part of this chapter is devoted to the description of deriving expressions for this combined system investigated in the different CM modes mentioned above. Parts of the derivations which are presented in the following sections were published similarly as shown by us in the appendix of reference [24]. Furthermore the main reference for this part are Gross *et al.* [25] and [80].

The energy of such a combined system can be described by the sum of a mechanical energy term and a magnetic energy term. In doing so, we approximate the cantilever‘s free-end motion as a simple harmonic oscillator and obtain the following equation for the energy:

$$E = \frac{1}{2}k_0(l_e \sin\theta_c)^2 + E_m, \tag{1.12}$$

where θ_c is the angle of the cantilever‘s free-end with respect to $\mathbf{H}$ and E_m is the magnetic energy. The Si cantilever and the epoxy which is used to attach the sample are assumed to be not magnetic, therefore E_m depends only on the properties of the attached sample. For the moment we treat E_m as a general term but we specify it later on and derive an expression for it. In order to calculate the torque acting on the free-end of the cantilever we can use the first derivative of the total energy, given in (1.12) [57]. The coordinate system which is used in the following is illustrated in Fig. 1.8. The cantilever

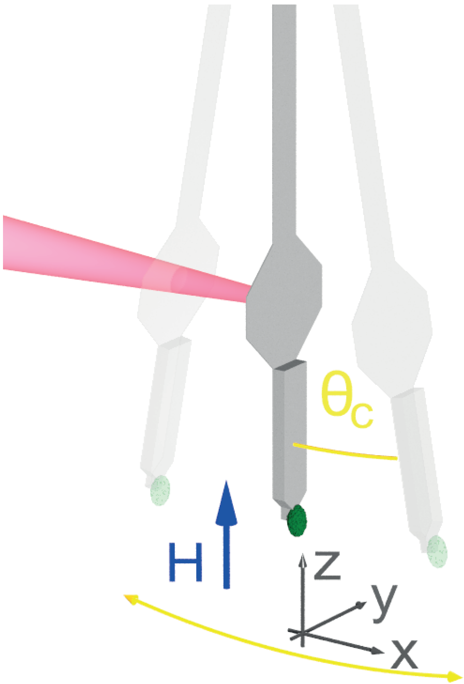

Figure 1.8: Schematic diagram of the experimental setup.

oscillates in $\hat{\mathbf{x}}$ direction, $\mathbf{H}$ is applied in $\hat{\mathbf{z}}$, while $\hat{\mathbf{y}}$ is coincident with the cantilever's axis of rotation. Therefore the measured cantilever deflection θ_c depends on the $\hat{\mathbf{y}}$ component of the torque, which is given by:

$$\tau_y(\theta_c) = -\frac{\partial E}{\partial \theta_c} = -k_0 l_e^2 \sin\theta_c \cos\theta_c - \frac{\partial E_m}{\partial \theta_c} \tag{1.13}$$

Since during the measurement $\theta_c \ll 1°$, we can expand E_m as a function of θ_c around $\theta_c = 0$:

$$E_m(\theta_c) = E_m|_{\theta_c=0} + \left(\frac{\partial E_m}{\partial \theta_c}\bigg|_{\theta_c=0}\right)\theta_c + \frac{1}{2}\left(\frac{\partial^2 E_m}{\partial \theta_c^2}\bigg|_{\theta_c=0}\right)\theta_c^2 + \ldots \tag{1.14}$$

From the previous two equations we can note down an expression for $\tau_y(\theta_c)$. By keeping only terms up to the first order in θ_c, we obtain:

$$\begin{aligned}\tau_y(\theta_c) &= -k_0 l_e^2 \theta_c - \left(\frac{\partial E_m}{\partial \theta_c}\bigg|_{\theta_c=0}\right) - \left[\left(\frac{\partial^2 E_m}{\partial \theta_c^2}\bigg|_{\theta_c=0}\right)\right]\theta_c, \\ &= -\left(\frac{\partial E_m}{\partial \theta_c}\bigg|_{\theta_c=0}\right) - \left[k_0 l_e^2 + \left(\frac{\partial^2 E_m}{\partial \theta_c^2}\bigg|_{\theta_c=0}\right)\right]\theta_c,\end{aligned} \tag{1.15}$$

where $\frac{\partial E_m}{\partial \theta_c}\Big|_{\theta_c=0}$ and $\frac{\partial^2 E_m}{\partial \theta_c^2}\Big|_{\theta_c=0}$ are the first and second derivatives of the magnetic energy with respect to θ_c. Treating the cantilever as a damped harmonic oscillator, the equation of motion can be written as:

$$m_e\ddot{x} + \Gamma\dot{x} = \frac{\tau_y(\theta_c)}{l_e}. \tag{1.16}$$

The position of the free-end of the cantilever is given by $x = l_e \sin\theta_c$. Since as mentioned before $\theta_c \ll 1^\circ$, we can approximate $x \approx l_e\theta_c$. By replacing (1.15) into (1.16), we find the following expression:

$$m_e\ddot{x} + \Gamma\dot{x} + \left[k_0 + \frac{1}{l_e^2}\left(\left.\frac{\partial^2 E_m}{\partial\theta_c^2}\right|_{\theta_c=0}\right)\right]x = -\frac{1}{l_e}\left(\left.\frac{\partial E_m}{\partial\theta_c}\right|_{\theta_c=0}\right). \tag{1.17}$$

It results that the first term in (1.15) produces a constant deflection of the cantilever, while the second term proportional to θ_c defines the spring constant of the cantilever. Accordingly we can introduce a magnetic spring constant $k_m = \frac{1}{l_e^2}\left(\left.\frac{\partial^2 E_m}{\partial\theta_c^2}\right|_{\theta_c=0}\right)$ and a driving force $F_m = -\frac{1}{l_e}\left(\left.\frac{\partial E_m}{\partial\theta_c}\right|_{\theta_c=0}\right)$ originating from the magnetic sample. The magnetic spring constant causes to shift the angular mechanical resonance frequency of the cantilever from its original value, in absence of a magnetic interaction, $\omega_0 = \sqrt{\frac{k_0}{m_e}}$, to $\omega_m = \sqrt{\frac{k_0+k_m}{m_e}}$.

To obtain a general equation describing the frequency as a function of the applied magnetic field we solve the equation of motion of the combined system given by (1.17) and find the angular resonance frequency of the cantilever to be:

$$\omega = \sqrt{\frac{k_0}{m_e} + \frac{1}{m_e l_e^2}\left(\left.\frac{\partial^2 E_m}{\partial\theta_c^2}\right|_{\theta_c=0}\right) - \frac{\Gamma^2}{4m_e^2}}. \tag{1.18}$$

By defining the angular resonance frequency in the fundamental mode as $\omega_0 = \sqrt{\frac{k_0}{m_e}}$ and solving the previous equation for the angular frequency shift $\Delta\omega = \omega - \omega_0$ we find:

$$\Delta\omega = \omega_0\left(\sqrt{1 + \frac{1}{m_e\omega_0^2 l_e^2}\left(\left.\frac{\partial^2 E_m}{\partial\theta_c^2}\right|_{\theta_c=0}\right) - \frac{\Gamma^2}{4m_e^2\omega_0^2}} - 1\right). \tag{1.19}$$

For $k_m \ll k_0$, we expand (1.19) to the first order in k_m and obtain:

$$\Delta\omega = \frac{\omega_0}{2k_o}\left[\frac{1}{l_e^2}\left(\left.\frac{\partial^2 E_m}{\partial\theta_c^2}\right|_{\theta_c=0}\right) - \frac{\Gamma^2}{4m_e}\right]. \tag{1.20}$$

If $k_m \ll \frac{\Gamma^2}{4m_e}$, the last term of the previous equation can be neglected. Using $\Gamma = \frac{m_e\omega_0}{Q}$ and $\omega_0^2 = \frac{k_0}{m_e}$, we obtain $k_m \ll \frac{k_0}{4Q^2}$. In the case of high-quality cantilevers which we use for our measurements, the term depending on Γ is negligible compared to the spring constant terms, resulting in:

$$\Delta\omega = \frac{\omega_0}{2k_o l_e^2}\left(\left.\frac{\partial^2 E_m}{\partial\theta_c^2}\right|_{\theta_c=0}\right), \tag{1.21}$$

and we obtain for the change in the angular frequency:

$$\Delta\omega = \frac{\omega_0}{2k_0} k_m. \tag{1.22}$$

This equation is valid for DCM measurements (2$^{\text{nd}}$ mode), more details are given in Sec. 1.4.

Considering in (1.17) frequency components of the form $\tilde{x}e^{i\omega t}$ and $\tilde{F}_m e^{i\omega t}$ [72], taking the Fourier transform and rewriting it in terms of the angular driving frequency ω, we find:

$$-m_e\omega^2\tilde{x}(\omega) + i\omega\Gamma\tilde{x}(\omega) + [k_0 + k_m]\,\tilde{x}(\omega) = \tilde{F}_m(\omega). \tag{1.23}$$

Where $\tilde{x}(\omega)$ is the Fourier transform of the displacement and $\tilde{F}_m(\omega)$ of the magnetic driving force. We obtain the equation for the displacement response induced by the driving force as a function of ω:

$$\tilde{x}(\omega) = \frac{\tilde{F}_m(\omega)}{(k_0 + k_m - \omega^2 m_e) + i\omega\Gamma}. \tag{1.24}$$

For $k_m \ll k_0$ and a constant magnetic force F_m, (i.e $\omega = 0$, $\tilde{F}_m(\omega) = 2\pi F_m\delta(\omega)$, $\delta(\omega)$ being Dirac's distribution), the equation results in a constant displacement of the resonator of:

$$x(t) = \frac{F_m}{k_0}. \tag{1.25}$$

This expression is valid for 1$^{\text{st}}$ mode type of studies.

CM based on conventional static measurements traces the constant deflection term. This method is sensitive to low-frequency noise and does not take advantage of the high mechanical quality factor Q of nanomechanical oscillators. Instead, if a magnetic force $F_m(t)$ is applied at the mechanical resonance of the cantilever ω_m, the amplitude of the cantilever response is:

$$x(t) = \frac{-iQ}{k_0} F_m(t), \tag{1.26}$$

where the dissipation is given by $\Gamma = \frac{m_e\omega_m}{Q}$. Comparing (1.25) with (1.26), i.e. the displacement in the 1$^{\text{st}}$ mode with the 3$^{\text{rd}}$, we find that by modulating the magnetic interaction at the cantilever's resonance frequency, the cantilever's response – and therefore the measurement sensitivity – is enhanced by a factor of Q. More details about the resonant cantilever magnetometry are given in the section 1.5.

1.4 Dynamic Cantilever Magnetometry

CM can provide information about the saturation magnetization, anisotropy and switching behavior [25]. DCM-based measurements compared to constant deflection studies are not so sensitive to low frequency noise. During DCM experiments the cantilever's resonance frequency as a function of the applied magnetic field **H** is detected. In order to extract precisely and fast the frequency from the deflection signal, the cantilever can be driven at its resonance frequency. For this self-oscillation process we use in our setup a piezo-electric actuator to mechanically drive the cantilever with a constant oscillation amplitude, controlled by a feedback loop implemented by a field-programmable gate array (FPGA), see Sec. 1.6. The oscillation amplitude is chosen to be $x \ll l_e$, so that the cantilever can be treated as a simple harmonic oscillator and the small angle approximation remains valid. From the DCM measurements we have access to the resonant frequency shift with respect to its intrinsic value as a function of the applied field: $\Delta f(H)$.

From Eq. (1.21) and given that the resonance frequency is $f_0 = \frac{\omega_0}{2\pi}$ and $\Delta f = \frac{\Delta\omega}{2\pi}$, it follows:

$$\Delta f = \frac{f_0}{2k_o l_e^2} \left(\left. \frac{\partial^2 E_m}{\partial \theta_c^2} \right|_{\theta_c = 0} \right). \tag{1.27}$$

This equation shows that by extracting Δf we investigate the curvature of the magnetic energy with respect to the cantilever angle. Generally speaking, a positive value of Δf means that $E_m(\theta_c)$ is in a local minimum with respect to θ_c, and therefore by changing the cantilever angle, E_m increases. Put differently, given the alignment of the nanomagnet's net magnetization, its physical orientation in the xz-plane is energetically preferred. In this case, the cantilever is exposed to a spring-like magnetic restoring force originated from the sample, which stabilizes this orientation. Therefore an effective hardening of the cantilever's spring constant is generated by this "magnetic spring". The result is an increase of the resonant frequency.

In the other case where a negative value of Δf is observed, the system is in a local maximum of $E_m(\theta_c)$. This is, given the alignment of the net magnetization of the sample, its physical orientation in the xz-plane is energetically unfavorable. Therefore the cantilever is under influence of an anti-restoring force, resulting in an effective softening of the cantilever spring constant and therefore in a reduction of the resonance frequency.

Eq. (1.27) describing Δf was derived without making assumptions regarding the sample specification. Hence it is a generally valid result and can be applied to different kind of samples. But for a better understanding and interpretation of the measured DCM (Δf) signal it is necessary to find a more precise expression for E_m and to differentiate it with respect to θ_c. This information is also needed to make analytical or numerical prediction of the expected signal. Therefore we approximate E_m with a sum of a Zeeman term and an anisotropy term [32,57] (a detailed description about the contributions to the magnetic energy is given in Chap. 2):

$$E_m = -\mu_0 V \mathbf{M} \cdot \mathbf{H} - KV(\hat{\mathbf{m}} \cdot \hat{\mathbf{n}})^2, \tag{1.28}$$

where μ_0 is the vacuum permeability, V is the volume of the sample, and $K > 0$ is an easy-axis crystalline anisotropy. Furthermore $\mathbf{M}$ describes the net magnetization averaged over the sample and $\hat{\mathbf{m}}$ is its associated unit vector, see Fig. 1.9(b). $\hat{\mathbf{n}}$ is the associated unit vector of the magnetic object, see Fig. 1.9(a). $\mathbf{M}$ and $\mathbf{m}$ described in terms of spherical coordinates are:

$$\mathbf{M} = M_s \begin{pmatrix} \sin(\theta_m)\cos(\phi_m) \\ \sin(\theta_m)\sin(\phi_m) \\ \cos(\theta_m) \end{pmatrix} \qquad \hat{\mathbf{n}} = \begin{pmatrix} \sin(\theta_n)\cos(\phi_n) \\ \sin(\theta_n)\sin(\phi_n) \\ \cos(\theta_n) \end{pmatrix} \tag{1.29}$$

where M_s is a constant called saturation magnetization. See Fig. 1.9 for the illustration of orientation of the sample (a) and its average magnetization (b), respectively θ_n, ϕ_n and θ_m, ϕ_m. In order to probe the magnetization during the measurements we use an oscillating cantilever. This oscillation, see Fig. 1.8, results in a rotation of the sample orientation $\hat{\mathbf{n}}$ around $\hat{\mathbf{y}}$. The consequence is an additional dependence of the sample orientation on θ_c and therefore also E_m depends on θ_c.

By implementing (1.28) and the vectors defining the orientation of the sample and of the average magnetization into a *Mathematica* script we can solve the system for certain limits. In the following, two different cases are investigated, therefore (1.28) is evaluated for small applied fields and afterwards for high fields.

1.4.1 The Low-Field Limit

In the range of low applied magnetic fields where $H \ll K/M$, the crystalline anisotropy dominates the magnetic energy. Due to that, the net magnetization $\mathbf{M}$ remains either parallel or anti-parallel to the crystalline axis $\hat{\mathbf{n}}$. Therefore, due to the cantilever's oscillation, only the curvature of the first term 1.28 in the magnetic energy is probed, resulting in:

$$E_m = -\mu_0 V M_s H \left[\cos(\theta_c)\cos(\theta_n) - \sin(\theta_c)\cos(\theta_n)\sin(\theta_n)\right] - KV. \tag{1.30}$$

Taking the second derivative with respect to θ_c:

$$\frac{\partial^2 E_m}{\partial \theta_c^2} = -\mu_0 V M_s H \left[\cos(\theta_c)\cos(\theta_n) - \sin(\theta_c)\cos(\theta_n)\sin(\theta_n)\right], \tag{1.31}$$

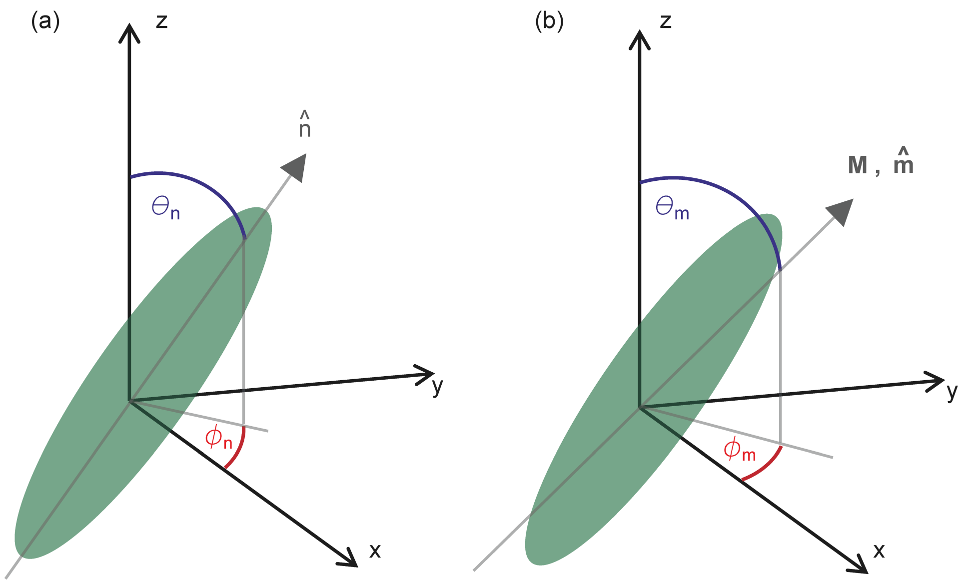

Figure 1.9: Schematic diagram illustrating (a) the angles θ_n, ϕ_n defining the orientation of the sample and (b) θ_m, ϕ_m defining the orientation of the magnetization. Adapted from [81].

and by using $\theta_c \ll 1°$, we obtain:

$$\left.\frac{\partial^2 E_m}{\partial \theta_c^2}\right|_{\theta_c=0} = \mu_0 V M_s H \cos(\theta_n). \tag{1.32}$$

Solving (1.27), it results in:

$$\Delta f = \frac{f_0}{2k_0 l_e^2}\mu_0 V H M_s \cos(\theta_n) = \frac{f_0 \mu_0 V}{2k_0 l_e^2} H M_z. \tag{1.33}$$

Accordingly, this low-field regime results in a special case, where it is possible to determine M_z from the measurements of Δf. Solving this previous expression for M_z, we find:

$$M_z = \frac{2k_0 l_e^2}{f_0 \mu_0 V}\frac{\Delta f}{H}. \tag{1.34}$$

1.4.2 The High-Field Limit

Now we examine the case of a high applied magnetic field where $H \gg K/M$. Here the orientation of the sample does not have an influence on the direction of $\mathbf{M}$, since $\mathbf{M}$ is forced to be parallel to $\mathbf{H}$. By applying this limit and evaluating (1.28) we obtain:

$$E_m = -\mu_0 V M_s H - KV\left[\cos(\theta_c)\cos(\theta_n) - \sin(\theta_c)\cos(\phi_n)\sin(\theta_n)\right]^2. \tag{1.35}$$

By taking the second derivative and using $\theta_c \ll 1^\circ$, it comes:

$$\left.\frac{\partial^2 E_m}{\partial \theta_c^2}\right|_{\theta_c=0} = 2KV\left[\cos^2(\theta_n) - \sin^2(\theta_n)\cos^2(\phi_n)\right], \tag{1.36}$$

By solving (1.27), we find that Δf approaches a horizontal asymptote given by:

$$\Delta f = \frac{f_0}{k_0 l_e^2} VK\left(\cos^2(\theta_n) - \sin^2(\theta_n)\cos^2(\phi_n)\right), \tag{1.37}$$

In this high field limit, Δf is a measure of the anisotropy energy of the sample, multiplied by a factor depending on its orientation relative to $\mathbf{H}$. By applying an high enough field so that $\mathbf{M}$ and $\mathbf{H}$ are forced to be parallel, the cantilever oscillation only probes the curvature of the second term in the magnetic energy shown in (1.28).

1.5 Resonant Cantilever Magnetometry

DCM is a suitable technique for the investigation of different types of magnetic samples. But, if for instance the sample size is decreasing, also the signal is reduced significantly. By improving the geometry, up to a certain point a higher sensitivity can be achieved (see Sec. 1.2.1.2). But as the geometry gets optimized, other influences like surface effects or more difficulties in the read out become more pronounced. Another disadvantage is that according to (1.33) the sensitivity scales with H and is therefore smaller for low applied fields. In order to improve the technique a few changes have to be made.

In this section a variation of the 3rd CM mode is presented. Therefore, we apply a magnetic field at the cantilever‘s resonance frequency and measure the amplitude of the magnetically driven response. As shown in the following, by using this method, we obtain access to the first derivative of the magnetic energy with respect to the cantilever angle. In order to do so, two small coils are mounted close to the cantilever, see Figs. 3.6 and B.1(b). The angular resonance frequency $\omega_m(H)$ is measured and afterwards H_{AC} at ω_m is applied while determining the response amplitude $\tilde{x}(\omega_m)$. An AC magnetic field $\mathbf{H}_{AC}$ ($H_{AC} \simeq 10\ \mu$T) along either $\hat{\mathbf{x}}$ or $\hat{\mathbf{z}}$ is applied. According to (1.23) and by the use of $F_m = -\frac{1}{l_e}\left(\left.\frac{\partial E_m}{\partial \theta_c}\right|_{\theta_c=0}\right)$ we obtain:

$$\tilde{x}(\omega_m) = \frac{iQ}{k_0 l_e}\left(\left.\frac{\partial E_m(\omega_m)}{\partial \theta_c}\right|_{\theta_c=0}\right). \tag{1.38}$$

The resonant magnetic driving of the cantilever oscillation is called resonant cantilever magnetometry (RCM).

As it was the case for the DCM signals, for a better understanding and the possibility to perform analytical or numerical predictions of the expected RCM signal, the exact expression for E_m at ω_m should be found and differentiated with respect to θ_c. As before we will investigate the behavior for certain limits which can be derive from (1.28).

1.5.1 The Low-Field Limit

For low applied magnetic fields, where $H \ll K/M$, the crystalline anisotropy dominates the magnetic energy. Under this condition, the net magnetization $\mathbf{M}$ points either parallel or antiparallel to the crystalline axis $\hat{\mathbf{n}}$. Applying this condition to (1.28) and expressing $\mathbf{M} = \boldsymbol{\chi}\mathbf{H}$ in terms of the magnetic susceptibility $\boldsymbol{\chi}$, we obtain for the magnetic energy at ω_m:

$$E_m(\omega_m) = -\mu_0 V(\mathbf{M} \cdot \mathbf{H_{AC}} + \bar{\boldsymbol{\chi}}_{\boldsymbol{AC}} \cdot \mathbf{H_{AC}} \cdot \mathbf{H}). \tag{1.39}$$

Here $\bar{\boldsymbol{\chi}}_{\boldsymbol{AC}}$ is the AC magnetic susceptibility tensor. By use of (1.38), we obtain an amplitude response given by the following two expressions for the coils oriented along $\hat{\mathbf{x}}$ and $\hat{\mathbf{z}}$:

$$\tilde{x}_{x\text{-coil}}(\omega_m) = -\frac{i\mu_0 VQ}{k_0 l_e} H_{AC} \left(\left.\frac{\partial M_x}{\partial \theta_c}\right|_{\theta_c=0} + H \left.\frac{\partial\left(\hat{\mathbf{z}} \cdot \bar{\boldsymbol{\chi}}_{\boldsymbol{AC}} \cdot \hat{\mathbf{x}}\right)}{\partial \theta_c}\right|_{\theta_c=0} \right); \tag{1.40}$$

$$\tilde{x}_{z\text{-coil}}(\omega_m) = -\frac{i\mu_0 VQ}{k_0 l_e} H_{AC} \left(\left.\frac{\partial M_z}{\partial \theta_c}\right|_{\theta_c=0} + H \left.\frac{\partial\left(\hat{\mathbf{z}} \cdot \bar{\boldsymbol{\chi}}_{\boldsymbol{AC}} \cdot \hat{\mathbf{z}}\right)}{\partial \theta_c}\right|_{\theta_c=0} \right). \tag{1.41}$$

If the magnetization that does not respond to the small AC drive field when for example $\bar{\boldsymbol{\chi}}_{\boldsymbol{AC}} = 0$ or the susceptibility is isotropic, there will be no contribution of the last terms of (1.40) and (1.41). For instance, these assumptions would be valid for ferromagnetic samples. Additionally, if no or a very small external magnetic field is applied, the second term of the previous two equations also gives no contribution to the detected amplitude response. Furthermore, $\mathbf{M}$ will be fixed to the anisotropy axis during the cantilever oscillation and as a result, $\left.\frac{\partial M_x}{\partial \theta_c}\right|_{\theta_c=0} = M_z$ and $\left.\frac{\partial M_z}{\partial \theta_c}\right|_{\theta_c=0} = -M_x$, we obtain:

$$\tilde{x}_{x\text{-coil}}(\omega_m) = -\frac{i\mu_0 VQ}{k_0 l_e} H_{AC} M_z; \tag{1.42}$$

$$\tilde{x}_{z\text{-coil}}(\omega_m) = \frac{i\mu_0 VQ}{k_0 l_e} H_{AC} M_x. \tag{1.43}$$

According to these expressions, the direct determination of M_z and M_x from the cantilever's driven response is possible. Solving (1.42) and (1.43) for M_z and M_x respectively:

$$M_z = \frac{ik_0 l_e}{\mu_0 VQH_{AC}} \tilde{x}_{x\text{-coil}}(\omega_m); \tag{1.44}$$

$$M_x = -\frac{ik_0 l_e}{\mu_0 V Q H_{AC}} \tilde{x}_{z\text{-coil}}(\omega_m). \tag{1.45}$$

1.5.2 The High-Field Limit

For the other extreme where a large field is applied , i.e. $H \gg K/M$, $\mathbf{M}$ is forced to be parallel to $\mathbf{H}$. Applying this limit to (1.28) and solving (1.38), it results that the driven displacement amplitude approaches zero: $\tilde{x}(\omega_m) = 0$.

By comparing the detectable signals for the RCM with the DCM we find that under certain conditions each method can have advantages compared to the other. In the high-field limit where $H \gg K/M$ the amplitude response of the RCM approaches zero. Therefore, by using DCM, see (1.33), more information can be obtained compared to RCM, which is not really suitable for the investigation at high magnetic fields. Instead if $H \ll K/M$, RCM provides information about M_z (1.44) and M_x (1.45) of the sample, while DCM is only sensitive to M_z (1.33). Especially if $H = 0$, according to (1.37) we cannot measure any magnetic response by using DCM. Therefore, RCM is a useful supplement to the DCM technique especially at small applied magnetic fields.

1.6 Dissipation Magnetometry

As described before, in order to read-out the frequency in an accurate and fast way, the cantilever can be driven at its resonance frequency. Together with a better and more time-efficient read-out, compared to non-driven measurements, we also gain access to another quantity, the dissipation.

For driving the cantilever mechanically with a constant oscillation amplitude a piezo-electric actuator is used. The control of the applied voltage to the piezo V_p is realized via a feedback loop which is implemented through a field-programmable gate array (FPGA). To ensure that a constant oscillation amplitude is retained, all the losses occurring during the measurement have to be compensated. The force of the piezo drive which is necessary to compensate for the losses caused by dissipation can be described by:

$$F_p = \Gamma \dot{x}. \tag{1.46}$$

If the self-oscillation process is running, we can read-out V_p. The voltage applied to the piezo is proportional to F_p and as a consequence of (1.46) also proportional to the dissipation Γ. That is why by detecting V_p we simultaneously keep track of $\Gamma(H)$. The dissipation can be described by the sum of Γ_0, due to the mechanical energy losses intrinsic to the cantilever (at zero field), and a term covering any other extrinsic non-conservative forces.

The mechanical energy losses Γ_0 for a cantilever in vacuum are mainly due to clamping losses and internal friction. The internal friction can be caused by the relaxation effects due to adsorbates, dislocations, motions of lattice defects, etc. [62, 63]. Since for DCM studies the extrinsic losses are due to the applied magnetic field **H**, we can express this term in the dissipation with $\Gamma_m(H)$, a magnetic dissipation which depends on H [32]:

$$\Gamma(H) = \Gamma_0 + \Gamma_m(H). \tag{1.47}$$

Γ_m depends on the magnetic anisotropy of the sample and due to that it can be described in terms of the magnetic relaxation. We calculate from (1.28) the change of the energy induced by Γ_m using $\theta \ll 1$. By using $M(t) = M_0(1 - e^{t/T_1})$, where T_1 is the magnetic relaxation time, we calculate the derivative $\frac{dM}{dt} = -\frac{M(t)-M_0}{T_1}$ and obtain T_1 and then Γ_m as [57]:

$$\Gamma_m \propto \frac{T_1}{(1 + \omega_0^2 T_1^2)^2}. \tag{1.48}$$

T_1 has a different value for each magnetic state. Big changes are experienced during phase transitions. If $T_1 \simeq 1/f_0$, according to (1.48) Γ_m(H) will be peaked and in any other circumstance Γ_m(H) will be smaller. As a consequence, also the magnetic dissipation should reflect the phase transitions. In the other regions, where no phase transition happens, T_1 and therefore also Γ_m(H) should stay more or less constant. As a result, by keeping track of V_p, we obtain a signal which provides information about occurring phase transitions.

Besides assigning phase transition, the dissipation sets also a limit to the minimum detectable magnetic moment. By taking into account the minimal detectable force of a cantilever (1.3), Stipe *et al.* calculated for their DCM measurements that the minimal detectable magnetic moment is below 10^4 μ_B, μ_B being Bohr's magneton [32].

1.7 Numerical Calculations

In addition to our measurements, we perform numerical calculations in order to estimate the expected frequency shift for DCM measurements. We compare two different software packages, *Nmag* [82] which is based on the finite element method, and $mumax^3$ [83], based on the finite difference method. Both software packages use micromagnetic formalism and solve numerically the Landau-Lifschitz-Gilbert equation. For both *Nmag* and $mumax^3$ we obtain the same results.

The procedure is as follows: First we calculate the magnetization configuration of the sample, when the cantilever is in its equilibrium position $\theta_c = 0$.

From these calculations we obtain $E_m(0)$ for each value of H. In addition we obtain for each value of H a map of the magnetization, which allows us to analyze the magnetic state in detail. Afterwards we tilt the sample by a small but finite angle $\delta\theta_c \lesssim 1°$ in both directions from the equilibrium position, corresponding to the direction of the cantilever motion. We repeat solving for the magnetic energy for the other two configurations. Having $E_m(0)$, $E_m(\delta\theta_c)$, and $E_m(-\delta\theta_c)$ for each value of H, we can calculate the DCM frequency shift by using the differential quotient for a second order derivative and insert it into equation (1.27), and we obtain:

$$\Delta f \approx \frac{f_0}{2k_o l_e^2} \frac{E_m(\delta\theta_c) + E_m(-\delta\theta_c) - 2E_m(0)}{(\delta\theta_c)^2} \tag{1.49}$$

We then compare the results of our numerical analysis with those from our experiments, as shown and described in detail in chapter 3.

2 Magnetism

In the previous chapter the technical aspects regarding the investigation of magnetic samples by DCM are described. There we discuss the important components like the cantilever and the displacement detection, and derive the equations in order to analyze the data. Until now an important component has not yet been addressed in detail: the magnetic sample itself. So far, we have made generally valid assumptions regarding a magnetic object attached to a nanomechanical oscillator. In this chapter we provide information regarding the magnetic materials studied in this thesis.

The research of this work includes the investigation of three different types of materials by DCM. The behavior of ferromagnetic (FM) NTs made of CoFeB, is studied depending on the aspect ratio (see Sec. 2.2 and Chap. 3). Furthermore, we explore the existence of a skyrmion lattice in MnSi NWs as a function of temperature and applied magnetic field, depending on the orientation of the wire with respect to the field direction (see Sec. 2.3.1 and Chap. 4). In the third set of measurements, we investigate the angle dependence of the applied magnetic field for GaV_4S_8 single-crystal (see Sec. 2.3.2 and Chap. 5).

This chapter is intended to give the necessary theoretical background in order to understand the results presented later on. Only the aspects which are relevant for the investigated materials are discussed.

2.1 Energy Terms in a Magnetic Object

In order to describe the behavior of a microsized magnetic object it is necessary to know what contributes to the magnetic energy. The interaction between the different energy contributions define the realized magnetic structure. In the following we give an overview about the different energy terms and in doing so we use the following references [84–89].

Different energies contribute to the total free energy E_{tot} of a magnetic microstructure. The four main energies are the Zeeman energy E_Z, the exchange energy E_{ex}, the anisotropy energy E_K, and the magneto-static energy E_{ms}. These energies add up to:

$$E_{tot} = E_Z + E_{ex} + E_K + E_{ms} \tag{2.1}$$

These contributing energy components are each separately described in detail in the following.

2.1.1 Zeeman Energy

The magnetic moments of a permanent magnet with volume V placed in an external field $\mathbf{H}$ try to align parallel to the field in order to minimize the energy. The interaction between the magnetization and an external applied magnetic field is described by the Zeeman energy and given by:

$$E_Z = -\mu_o \int \mathbf{M} \cdot \mathbf{H} \, dV \tag{2.2}$$

2.1.2 Exchange Energy

Magnetic ordering is associated with the exchange interaction: the latter imposes an order to the magnetic moments, but it does not impose a favored direction. In general, the exchange interaction can be of symmetric and asymmetric nature. Depending on the material composition, asymmetric interaction can have a significant influence (see Sec. 2.3), or has a negligible contribution compared to the symmetric term. This is for example the case of FM objects, on which we focus in the following.

The symmetric exchange interaction E_{ex} describes the Coulomb interaction between two neighboring spins $\mathbf{S_i}$ and $\mathbf{S_j}$ and is given by:

$$E_{ex} = -2 \sum_{i<j} J_{ij} \mathbf{S_i} \cdot \mathbf{S_j} \tag{2.3}$$

where J_{ij} is the exchange integral. The nearest neighbors align parallel with each other if J_{ij} has a positive value and therefore the resulting material is FM. If J_{ij} instead is negative, the spins align anti-parallel and end up anti-ferromagnetic. J_{ij} depends on the distance of the interacting spins, and with increasing distance J decays exponentially.

Under the assumption of a continuous material and a not too high temperature, E_{ex} can be described by the following equation (for a detailed derivation see [84]):

$$E_{ex} = \frac{A}{M_s^2} \int (\nabla \mathbf{M})^2 dV, \tag{2.4}$$

where A is the material-dependent exchange stiffness or also called coupling parameter, related to J_{ij}, and M_s is the saturation magnetization. M_s is an

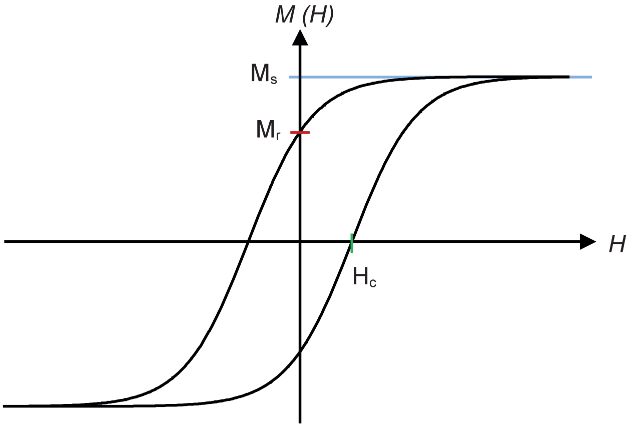

Figure 2.1: Schematic of the hysteresis curve of a typical FM material, with M_s, M_r and H_c assigned. Adapted from [84].

intrinsic property of the material, and it dependency on T. The temperature at which M_s is zero is defined as the Curie temperature T_c (also refereed to as the critical temperature): at this point a magnetic object loses its permanent magnetic properties. For instance, FM objects are paramagnetic above T_c. M_s is characteristic for FM and ferrimagnetic materials and can be most clearly seen in the magnetization as a function of applied magnetic field. For instance in Fig. 2.1, $M(H)$ for a standard FM sample is shown. As H increases, M approaches its maximum value, M_s. It is not given that M is 0 at $H = 0$; the magnetization which is present at $H = 0$ is called remanence or remanent magnetization M_r. The point in field where $M = 0$ is called coercivity or coercive field H_c.

2.1.3 Magnetostatic Energy

The result of the interaction of the sample‘s magnetization with its own stray-field is described by the magnetostatic energy and given by:

$$E_{ms} = -\frac{\mu_0}{2}\int \mathbf{M}\cdot\mathbf{H}_{dm} dV, \tag{2.5}$$

where $\mathbf{H}_{dm}$ is the demagnetization field. $\mathbf{H}_{dm}$ is the field caused by volume and surface charges of the object, as illustrated in Fig. 2.2. Adding $\mathbf{H}_{dm}$ and $\mathbf{H}$, we can calculate $\mathbf{H}'$, i.e. the total, internal magnetic field:

$$\mathbf{H}' = \mathbf{H} + \mathbf{H}_{dm}. \tag{2.6}$$

$\mathbf{H}_{dm}$ for a random shaped object is difficult to determine. In order to calculate $\mathbf{H}_{dm}$ it is necessary to solve the magnetostatic Maxwell equations. The result for a uniformly magnetized ellipsoid, is the following [85]:

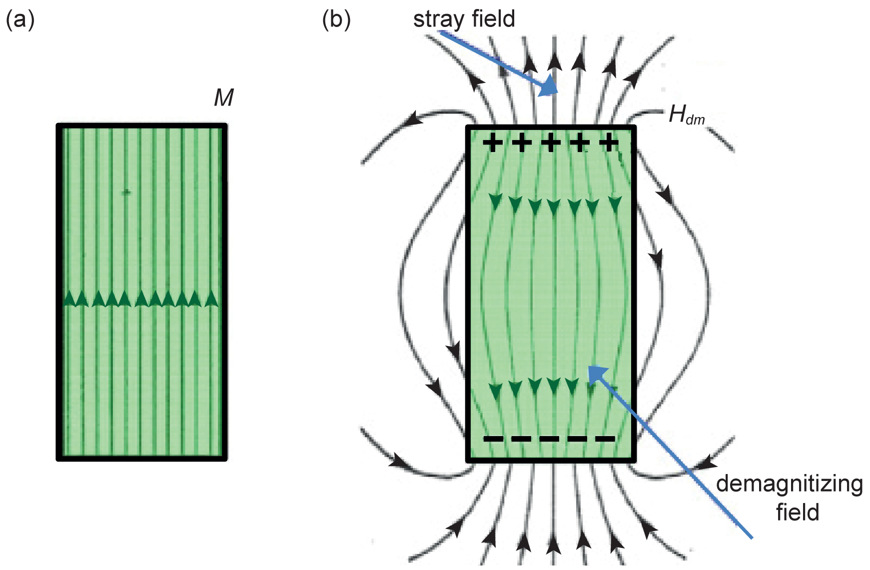

Figure 2.2: Schematic of a uniformly magnetized object in shape of a bar where (a) represents $\mathbf{M}$ pointing in the opposite direction of (b) the corresponding $\mathbf{H}_{dm}$ and the stray field. Adapted from [89].

$$\begin{pmatrix} H_x^{dm} \\ H_y^{dm} \\ H_z^{dm} \end{pmatrix} = - \begin{pmatrix} D_\perp & 0 & 0 \\ 0 & D_\perp & 0 \\ 0 & 0 & D_\parallel \end{pmatrix} \begin{pmatrix} M_x \\ M_y \\ M_z \end{pmatrix} . \tag{2.7}$$

The matrix elements $D_\perp$ and $D_\parallel$ are the demagnetization factors, with $2D_\perp + D_\parallel = 1$. By considering an average magnetization, it is possible to determine the demagnetization factors for a random shaped object with a uniform magnetization. However, this is just possible by assuming a uniform magnetization and neglecting details near edges and surfaces, resulting in an average demagnetizing field. More details can be found in several literature references, like [84, 85, 87, 89]

2.1.4 Magnetic Anisotropy

If the magnetization has the preference to point along a fixed direction, it is caused by anisotropy. Due to it, additional energy is necessary in order to turn the magnetization in any direction which differs from the preferred axes, called the easy axes. Therefore it has an important contribution to the hysteresis of a sample.

Magnetic anisotropy can have different origins. The only anisotropy intrinsic to the material, which is the most common one, is the crystal anisotropy. This type of anisotropy arises from spin-orbit interaction. Due to the non-spherical shape of the electron orbits, they prefer to align in a certain direction in the crystalline structure. The magnetocrystalline anisotropy is usually small compared to the exchange interaction and depends on the crystal lattice structure. The strength of the magnetization is mainly due to the exchange, but the direction is determined by the anisotropy. The direction in which the energy of the anisotropy has a local minimum is defined as the easy axis. If instead it has a local maximum it is a hard axis.

A kind of anisotropy, occurring in all our investigated samples, is the shape anisotropy. It is due to the fact that a magnetic object does not have a perfect spherical shape. Under this circumstance, the demagnetization fields will not be equal in all directions, hence creating an easy and a hard direction to align for the net magnetization. Therefore, the shape anisotropy is linked to the magnetostatic energy. It is the strongest anisotropy component for non-crystalline, non-spherical magnetic samples.

Another anisotropy is the surface-induced anisotropy, caused by physical processes on surfaces and/or interfaces. The symmetry at the boundary is reduced, since for instance a spin at the surface has a neighbor on one side, but none on the other. Therefore the exchange energy cannot be the same as in bulk. Furthermore, the contact of the magnetic object to the substrate can induce a strain due to lattice mismatch. These additional anisotropies are sensitive to the thickness of the sample. The influence is increasing for decreasing sample size as is the surface-to-volume ratio.

2.2 CoFeB Nanotubes

The focus in this section is on FM NTs, especially on CoFeB NTs. FM NTs have a non-magnetic core and therefore provide a promising shape and magnetic states. Especially the flux-closure configurations are of special interest for instance for being implemented in high density storage media. The reason is that this is the configuration which produces the smallest stray field and therefore minimizes interactions with close-by structures [9]. According to theoretical prediction, three stabilized equilibrium states can be hosted by this tubular structures [34]. A uniform axial, a mixed, and a vortex configuration are the predicted magnetic equilibrium states, illustrated in Fig. 2.3. These equilibrium states include vortex-like flux-closure configurations in which the magnetization is pointing along the NT circumference. In comparison, in magnetic NWs a non flux-closure configurations like a uniform axial alignment is always favored [25].

Landeros *et al.* made predictions about the stability of the states by dimension-based simulations [34]. By minimizing the total energy for these three different equilibrium states and the use of an analytic model, a phase diagram depending on the tubular geometry results. This phase diagram is

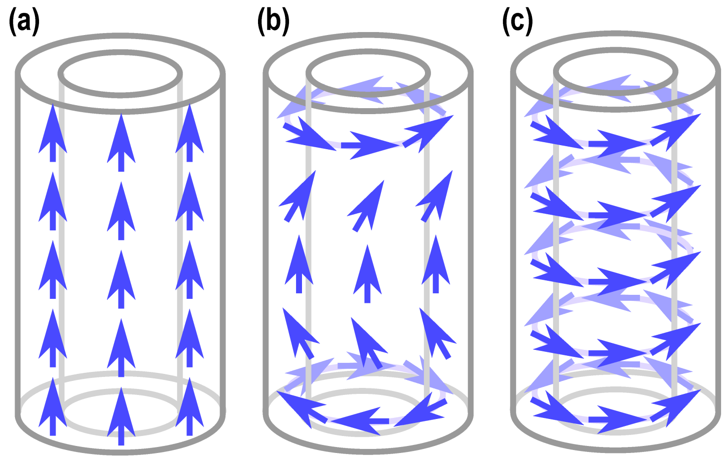

Figure 2.3: The predicted equilibrium states for a FM NT are (a) a uniform axial state,(b) a mixed, and (c) a vortex state. Figure adapted from Ref. [90].

presented in Fig. 2.4, in which the transitions between the different states are marked for three different tube sizes. The following definitions are used for the plot: $\beta = r_i/r_o$ is the ratio between the inner r_i and the outer r_o radius, L is the length of the tube, and λ_{ex} is the spin exchange length, defined as $\lambda_{ex} = \sqrt{\frac{2A}{\mu_0 M_s^2}}$.

Several other theoretical works investigated also the behavior of idealized FM NTs [10, 91–94]. Due to the similarity to the studied FM NTs, we use CoFeB NTs, see Chap. 3 for a more detailed description. These tubes have a 30-nm thick amorphous CoFeB shell around a non-magnetic core which has a hexagonal cross-sectional shape. Moreover they are free of defects, have a smooth surface with a roughness of only a few nm, and they have a rather high saturation magnetization [95]. With these characteristics these tubes provide a strong magnet with stable magnetic order, imposed by their geometry [25].

Landeros *et al.* assumed for their study a round cross-section, which is not given for our samples, but the model should be suitable for a better understanding and a first approximation of our samples. In order to reproduce the phase diagram for the CoFeB NTs, we use $A = 2.8 \times 10^{-11}$ J/m [96] and a saturation magnetization of $\mu_0 M_s = 1.29\ T$ [25]. The resulting theoretical phase diagram depending on the geometry is shown in Fig. 2.5. From this phase diagram we can read out a tendency, under which size-ratio a certain state is more probable then others. For our studied NTs, β is between 0.78 and 0.8. Due to the fact that the diameter of the core structure of our NTs is above 200 nm, it is rather unlikely to end up in an axial configuration. To end up in an axial magnetized state either a very small diameter of the non-magnetic core or even no core at all would be necessary. From Fig. 2.5

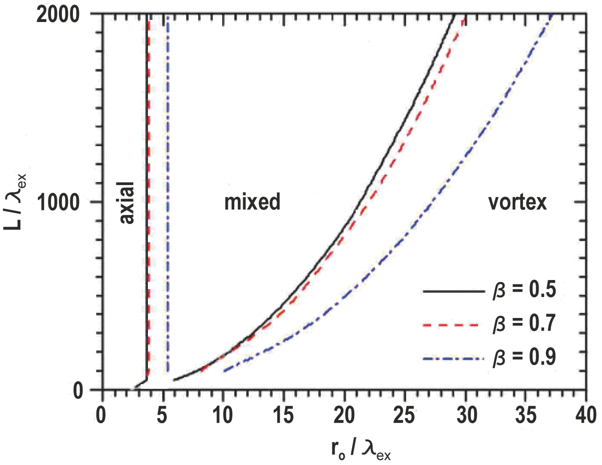

Figure 2.4: The phase diagram for FM NTs showing the transitions from axial to mixed and to vortex state as a function of the normalized tube length L/λ_{ex} and the normalized outer radius r_0/λ_{ex}. The transitions for $\beta = 0.5, 0.7$, and 0.9 are assigned. The plot is adapted from [34].

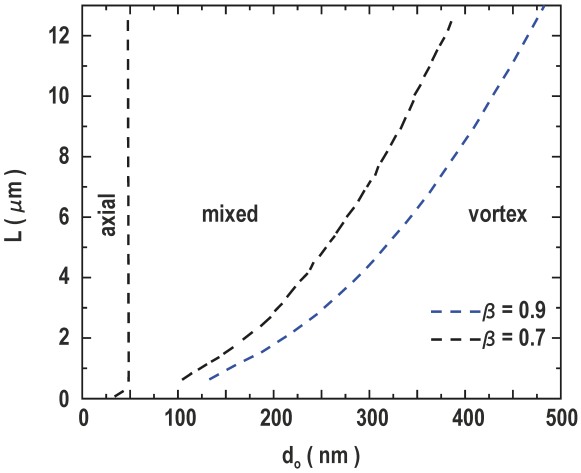

Figure 2.5: The phase diagram adapted from [34] for CoFeB NTs as a function of tube length L and the outer diameter d_0. The transitions for $\beta = 0.7$, and 0.9 are assigned.

we can see that for shorter and wider NTs a vortex state is favored, and the longer and thinner ones prefer the mixed state. Additionally to the three described equilibrium states, Chen *et al.* describe another configuration based on calculations [94]. In case of short tubes, instead of the vortex state shown in Fig. 2.3(c), a vortex configuration which is composed of two vortices with opposing chirality and a Nèel domain in between may also be stable. Experimentally, confirmations about the different states were reported based on MFM studies [97] and on x-ray magnetic dichroism photoemission electron microscopy (XMCD-PEEM) measurements [98].

Up to this point, only the static properties of ferromagnetic tubes were described. But of interest, in terms of applications, is also the dynamical behavior. For instance how these equilibrium states evolve, how stable and reproducible they are. Of special interest, as mention before are the flux-closure configurations due to the minimization of the interaction with close-by structures [9]. Given that FM NTs avoid an axial singularity, a fast and reproducible magnetization process should take place [34]. The magnetic reversal process seems to nucleate often at surfaces due to the magnetostatic charge, for instance. Therefore, the form of surfaces and edges - including any imperfections or roughness - can influence this process. A high surface-to-volume ratio as present in tubular structures, weakens the effects of surface imperfections by forming flux-closure configurations. Different theories exist about how the reversal event proceeds. It seems that the magnetization reversal process is driven by the nucleation event of a vortex followed by the propagation along its length, where the motion can be for example induced by a changing magnetic field or a current [99]. According to the theoretical prediction of reference [93], the reversal of the magnetization in long FM tubular structures can be caused by two different mechanisms. It could be achieved by a propagation of a transverse domain wall (DW), or by the propagation of a vortex DW. In order to identify which mechanism is favored, they introduced a critical radius $r_c(\beta)$, which depends on the material properties and the ratio of the radii. $r_c(\beta)$ defines the situation, at which the energy barrier for both propagation processes are equal. If $r_o < r_c(\beta)$ the process of the transverse DW is preferred and otherwise the vortex DW. According to these theoretical calculations, for our investigated CoFeB NTs $r_o > r_c(\beta)$, hence the magnetic reversal should be driven by the propagation of a vortex DW. For the sake of completeness, if the tube has a length being in the range of the size of a domain wall, a coherent rotation during the magnetic reversal can occur [93]. The shortest tube which we investigated is 640 nm long, therefore we should be out of this regime.

In order to obtain a better understanding of the nucleation of the vortex at the tube end, the propagating process, and the magnetic reversal, measurements of single tubes are required to confirm the theoretical predictions. Until now the investigation of the magnetic reversal has mainly be performed on big ensembles [100–106]. For measurements based on ensembles, controlling the distribution of size, shape and orientation can be difficult. Furthermore, the interaction between the different tubes has to be taken into account, which complicates the interpretation of the data.

A few dynamic studies of long single FM NTs were published recently. By the investigation with anisotropic magnetoresitance and anomalous Nernst effect techniques, the reversal process via domain wall movements and additionaly, a chirality switching process was observed [107]. Other studies describe the investigation of single tubes by the use of DCM [23, 25] and in combination with a SQUID [29, 30, 108]. Along with the previous DCM measurements numerical simulations were performed, describing the resulting feature in the frequency shift in occasion of a vortex nucleation and extinction at the end of a ferromagnetic tubular structure [25]. However the data collected with different FM tubes with length between 6 to 20 μm, did not show the features, which the theoretical calculations predicted. Hence, we repeated the measurements with shorter NTs and, in contrast to the previous samples, the ends of these tubes were well defined, in addition we had the freedom of changing the direction of the applied magnetic field. Chapter 3 is dedicated to the tracking of the nucleation and the vanishing of the vortex features for three different sample sizes. Furthermore, we trace the formation of a vortex configuration close to the magnetic reversal. Besides that, detailed description about the samples and cantilever properties, the measurement conditions as well as the results of our studies are provided.

2.3 Magnetic Skyrmions

In section 2.1.2 we mention that magnetic ordering is due to the exchange interaction, which has mainly a symmetrical character. On the other hand, the interaction between two neighboring spins in certain materials can be significantly influenced by an asymmetric exchange component. This additional exchange term contributes as well to the equation (2.1) describing the total magnetic energy and is defined by:

$$E_{DM} = -2\sum_{i<j} \mathbf{D_{ij}} \cdot (\boldsymbol{S_i} \times \boldsymbol{S_j}). \tag{2.8}$$

More common is the definition of this interaction by the term in the Hamiltonian [14]:

$$H_{DM} = -\mathbf{D_{ij}} \cdot (\boldsymbol{S_i} \times \boldsymbol{S_j}), \tag{2.9}$$

where $\mathbf{D_{ij}}$ is the Dzyaloshinskii vector. This asymmetric exchange contribution is also known as the Dzyaloshinskii-Moriya interaction (DMI). DMI occurs in

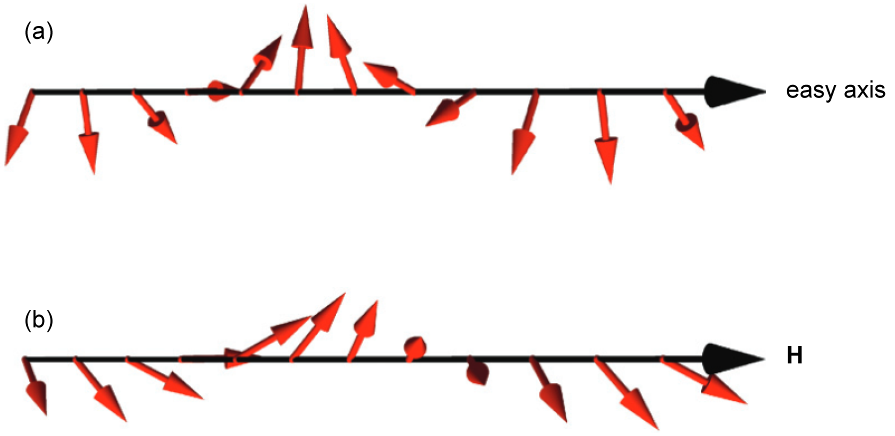

Figure 2.6: Schematic of the magnetization in (a) the helical phase and (b) the conical phase. Illustration adapted from [112]

non-centrosymmetric crystals with low symmetry, where the coupling (2.9) is not negligible [109]. DMI is responsible for the attempt to align the neighboring spins perpendicular to each other, which, in combination with the symmetric interaction, results in a slight tilt of the magnetic spins, in contrast to the perfect ferromagnetic alignment. The occurrence was first described by Dzyaloshinskii (1957) [110] and a mechanism was found by Moriya (1960) [111]. In magnets with a certain class of symmetry, the DMI causes, under special conditions, to form some chiral spiral structures which minimize the energy [14]. The most interesting structures are called magnetic skyrmions. They were experimentally observed the first time in 2009 in bulk MnSi, by means of small angle neutron scattering (SANS) [11]. More details about the special conditions and the arrangement of the spins are given in the course of this section.

We follow in this paragraph Levatić *et al.* [113] to describe the stability of the different states in skyrmion carrying materials and the transitions between them. In bulk skyrmion-containing samples, the strength of anisotropy K, DMI and symmetric exchange interaction J are in the relationship: $K \ll DMI \ll J$. The anisotropy due to the spin orbit interaction is the weakest interaction. Below a critical temperature T_c, the DMI prefers a perpendicular alignment between neighboring spins, while the symmetric exchange interaction favors a parallel alignment. This competition between the much stronger symmetric exchange and the DMI results in a spin spiral phase as a ground state, which is magnetically compensated. The chirality of the helical modulation is due to the missing inversion symmetry in the structure of the crystal and depends on the properties of the electronic structure [114]. The length of the modulation can be estimated as $L_D \sim J/DMI \gg a$, where a is the inter-atomic distance. L_D is determined by these two competing exchange energies but this is not the case for the direction of the modulation [112]. The direction is instead determined by K, which pins the helices along a preferred direction, hence the ordering wave vector q points in one direction, illustrated in Fig. 2.6(a). In case a magnetic field is applied, q turns in the direction of the magnetic field, which is energetically preferred [112]. Above a certain field H_{c1}, the spins start tilting and forming a cone-like arrangement, ending up in the conical phase, shown in Fig. 2.6(b). The value of H_{c1}, at which the phase transition between the helical and the conical phase takes place, depends on K, in a way that if K is higher, also H_{c1} needs to be higher. By increasing the external applied field even further, the spins align with the field at H_{c2}, where the transition from conical to FM takes place. Single skyrmions form a regular arrangement in which the central magnetic spin points in the opposite direction of $\mathbf{H}$. Several of them set up in stacks, one above another, in tubular structures and build the so called skyrmion lattice phase or A phase. The energy for the conical phase is always lower than for the skyrmion lattice in an intermediate magnetic field range and therefore favored. But if $\approx H_{c2}/2$ is applied at a temperature close to T_c the energy difference between these two phases is very small and due to thermal fluctuations, the skyrmion lattice is stabilized over the conical phase [11, 17]. Above T_c the magnet is a paramagnet, like a standard ferromagnetic sample. In some compounds like GaV_4S_8, the orientation of the skyrmions is determined by the magnetic easy axis and not by the direction of the applied magnetic field, more details about this and similar compounds are given in Sec. 2.3.2.

For completeness, we mention that skyrmions can be caused by four different mechanisms which can also act simultaneously. In this paragraph we follow the descriptions by Nagaosa and Tokura [17]. (1) Skyrmions can be caused by DMI as mentioned before. DMI occurs in non-centrosymmetric magnets like FeGe, MnSi, $Fe_{1\text{-}x}Co_xSi$, etc.. Skyrmions of this kind have sizes between 5 to 100 nm. (2) Skyrmions can arise from long-range magnetic dipolar interactions, which occur in magnetic thin films with perpendicular easy-axis anisotropy. There, the dipolar interactions prefers the in-plane magnetization in contrast to the anisotropy, which prefers the magnetization out-of-plane. These two different preferences competing with each other result in periodic stripes, where the magnetization rotates in a plane perpendicular to the film. If a magnetic field is applied perpendicular to the thin film, a periodic array of magnetic bubbles or skyrmions is formed out of the stripes. The originating structures have sizes of 100 nm up to 1 μm. Furthermore, skyrmions can be caused by (3) frustrated exchange interactions or (4) four-spin exchange interactions. (3) and (4) result in skyrmions having a size in the range of the lattice constant a of the material. The materials investigated in this thesis MnSi and GaV_4S_8 belong to the group of non-centrosymmetric crystals [17, 115] and therefore skyrmions are caused by DMI (mechanism

(1)). More information and properties about these specific crystals are given in the following two sections.

In materials in which the magnetic skyrmions are caused by DMI, mechanism (1), the orientation of the Dzyaloshinskii-Moriya vector can differ. The various orientations produce different types of skyrmions with an unequal rotation of the magnetic spins [14]. To describe the different types of magnetic skyrmions, we follow in this paragraph Bogdanov and Hubert [116]. As mentioned before, in order for magnetic skyrmions to occur, a combination of easy-axis FM and DMI is required, which is given only in certain crystal symmetries. Such a crystal symmetry is given in the C_n class with its subclasses C_{nv} and D_n (n = 3,4,6). The symmetry requirements are also fulfilled in the tetragonal classes S_4 and D_{2d}, but in these classes of crystals the interaction is intrinsically anisotropic, therefore the conditions are not in favor of forming skyrmions. Hence, we focus on the classes C_{nv} and D_n, for which the energy connected to the DMI w_D is given by:

$$\begin{aligned} w_D &= D_1 w_1 + D_2 w_2 + D_3 w_3 \\ &= D_1 \left(M_z \frac{\partial M_x}{\partial x} - M_x \frac{\partial M_z}{\partial x} + M_z \frac{\partial M_y}{\partial y} - M_y \frac{\partial M_z}{\partial y} \right) \\ &\quad + D_2 \left(M_z \frac{\partial M_x}{\partial y} - M_x \frac{\partial M_z}{\partial y} - M_z \frac{\partial M_y}{\partial x} + M_y \frac{\partial M_z}{\partial x} \right) \\ &\quad + D_3 \left(M_x \frac{\partial M_y}{\partial z} - M_y \frac{\partial M_x}{\partial z} \right), \end{aligned} \tag{2.10}$$

where D_i are arbitrary coefficients and we refer here to a coordinate system where the magnetization in the center points along the z-axis. The last term of the equation causes spiral structures propagating along the crystal axis (here along the z-axis). This term is not relevant for the materials investigated in this work and therefore we will focus only on the other two. Furthermore we will focus on the cases where the simultaneous existence of D_1 and D_2 is excluded. Two cases are remaining, resulting in two different types of skyrmions, occurring in the two different samples investigated in this work. The case in which only D_1 gives a contribution to the energy $(D_2, D_3 = 0)$ occurs in crystals with C_{nv} symmetry. Here only w_1 contributes to the DMI, which causes a rotation along the propagation direction of the spiral structure, resulting in Néel-type skyrmions, also referred to as vortex skyrmions. This type of skyrmion where the magnetization rotates in radial direction from the core outwards is illustrated in Fig. 2.7(b). A member of the C_{nv} symmetry class is for instance GaV_4S_8 [117]. Furthermore, Néel-type skyrmions have also been observed, for example, in PdFe/Ir(111) bilayers, which have a strong uniaxial anisotropy [19].

In the second case only $D_2 \neq 0$, representing a special case within the D_n

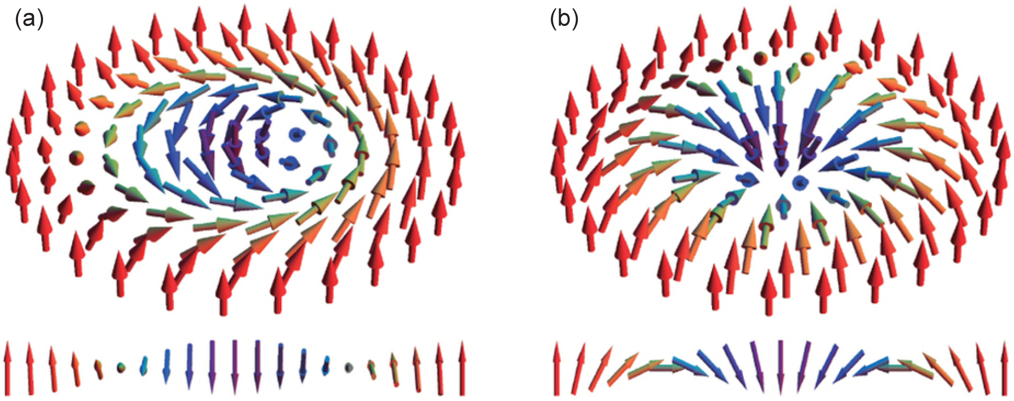

Figure 2.7: Differences in the spin rotation for (a) the Bloch-type skyrmion and (b) the Néel-type skyrmion. The spins rotate in the tangential plane in case of Bloch-type and in the radial plane for Néel-type skyrmions. The cross-section of the vortex is shown underneath for each type. Illustration from [117].

symmetry class. In this case Bloch-type skyrmions, also referred to as the hedgehog skyrmions, are favored. In the cubic materials like MnSi or FeGe an additional uniaxial anisotropy has to be present to stabilize vortex structures. The external stress or the growth anisotropy can cause an easy axis to occur and in this case these materials are examples of the D_n crystal class. The most common and most investigated structure is the Bloch-type skyrmion. In this type, the magnetic spins rotate perpendicular to the radial direction from the center outwards, as shown in Fig. 2.7(a). Bloch-type skyrmions are hosted in materials with a B20 crystal structure, like FeGe [118], MnSi, [11, 119], $\mathrm{Fe_{1\text{-}x}Co_xSi}$ [120] or $\mathrm{Cu_2OSeO_3}$ [121]. The alignment of these skyrmions is determined by the applied field direction. In contrast, in Néel-skyrmions is the orientation determined by an uniaxial anisotropy instead of an externally applied magnetic field. Furthermore, the relative size of the skyrmion lattice region in the phase diagram for Néel-skyrmions is significantly larger as for the Bloch-type [113].

The skyrmion lattice in bulk samples is typically present only in a small temperature field region, but different mechanisms can induce a stabilization of this phase. In case of spatial confinement, where the thickness of the sample is in the range of L_D or below, the skyrmion energy changes a lot, so that an extended skyrmion lattice down to low temperature results [122]. L_D in thin films is significantly reduced, therefore the exchange coupling must have different values. A stabilization can also be achieved by a uniaxial magnetic anisotropy, which is suppressing the helical phase and hence supporting the skyrmion lattice [123]. A uniaxial anisotropy can arise from the shape, interfaces, surfaces, crystal directions or pressure, but not all of them seem to show an effect on the skyrmion region. So far it seems that uniaxial

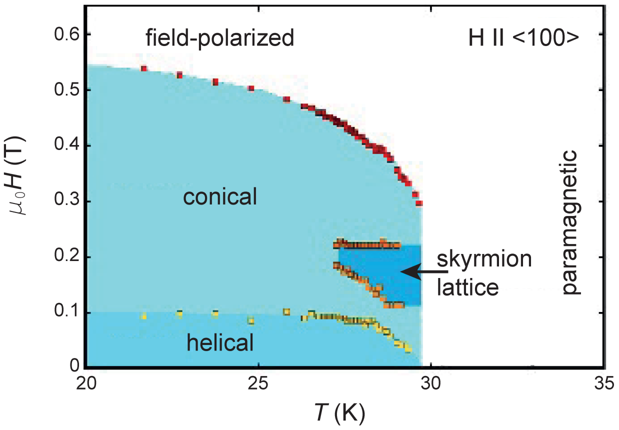

Figure 2.8: $\mu_0 H$ vs T phase diagram for bulk MnSi, where H is parallel to $\langle 100 \rangle$. The transitions were determined from SANS experiments. The plot is adapted from [11].

anisotropy due to pressure [113] and surfaces [24] has a stabilization effect. Furthermore, if a strain is induced due to a lattice mismatch or an effective negative pressure, T_c shifts to higher values and hence the skyrmion phase is stabilized up to higher temperatures [124].

2.3.1 Characteristics of MnSi

This section is dedicated to MnSi, which belongs to the class of B20 crystals and hosts Bloch-type skyrmions. The crystal lattice constant is $a \approx 4.56\AA$, it has skyrmion lattice constant of $L_D \approx 18$ nm in bulk and 8.5 nm in thin films [11, 17]. MnSi is one of the most studied skyrmion-containing samples and was investigated with various methods and in different shapes.

For a bulk single crystal, the region of the stabilized skyrmion lattice is limited to a small pocket close to T_c, where $T_c = 29.5$ K [11]. In Fig. 2.8 a typical phase diagram for a bulk sample is shown, where fields were applied parallel to $\langle 100 \rangle$. From another study it results that the skyrmion phase stability has a dependency on the crystal orientation with respect to the magnetic field direction [119]. If $\mathbf{H}$ is parallel to $\langle 100 \rangle$ the skyrmion phase is the largest and about double as big as for $\mathbf{H}$ applied parallel to $\langle 111 \rangle$. The stable region for H parallel to $\langle 110 \rangle$ has a size in-between the two others. T_c is constant for all the three configurations.

As mentioned previously, the stability of the skyrmion lattice phase depends strongly on the shape. A stabilization is achieved due to spatial confinement in thin films and a typical phase diagram for a free-standing, about 50-nm thick film is shown in Fig. 2.9. The conical phase is suppressed and the skyrmion lattice extends to low temperatures. By comparing Fig. 2.8 and 2.9 besides an extent of the phase, also a decrease in T_c of 7 K occurs,

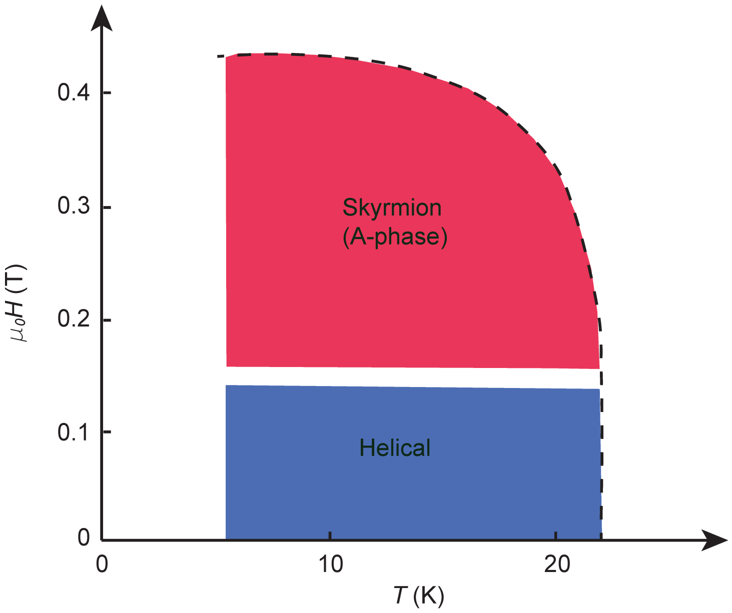

Figure 2.9: Phase transitions of a 50 nm thick MnSi film, detected with TEM measurements. The plot is adapted from [125].

which implies that T_c is thickness dependent. Furthermore, an increase of T_c was also observed in a 50-nm thick MnSi grown on top of Si(111). Hence the film was not free-standing and the lattice mismatch introduced a stress which raises T_c up to about 45 K [124].

Besides thin-film and bulk samples, also MnSi NWs were investigated. For example a skyrmion stabilization comparable to thin film samples was observed with a NW, which was thinned down to 50 nm [126]. Furthermore, some surprising results were obtained with NWs which have a thickness well above 200 nm. It seems that the size of the skyrmion region depends on the orientation of the NW with respect to $\mathbf{H}$ [24, 52, 127, 128]. More details are given in the experimental chapter 4, which is focused on the measurements performed during the work of this thesis.

In order to assign phase transitions, often the magnetization as a function of $\mathbf{H}$ is used. For explanation of the assignment of phase boundaries, we follow in the next paragraph the description of reference [119]. $M(H)$ has a characteristic shape for MnSi, visualized in Fig. 2.10. The skyrmion lattice phase is represented in form of a slightly tilted plateau. At the edges of this plateau M changes discontinuously (first order). Trace (i) in Fig. 2.10 illustrates $M(H)$ at a constant T. By following this trace, two first-order transitions are crossed. According to this description the phase transitions can be assigned, even if the steps are smeared out in experimental data.

The focus in our experimental work is on the determination of the occur-

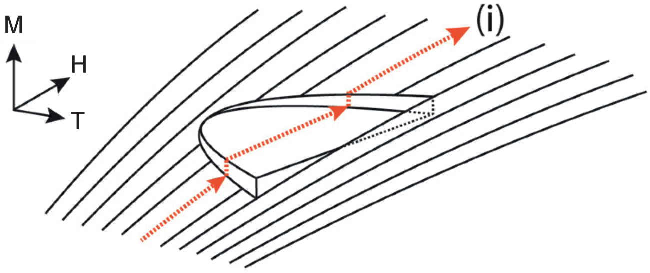

Figure 2.10: Illustration of $M(H,T)$. The plateau depict the skyrmion lattice phase and the trace (i) represents a measurement of $M(H)$ at a constant T. The plot is adapted from [119].

rence of a skyrmion lattice in single MnSi NWs, depending on the orientation of the wire with respect to the applied magnetic field. The results of the measurements and more details about the studied NWs are given in Chap. 4.

2.3.2 Characteristics of GaV_4S_8

The skyrmion phase was further investigated in a GaV_4S_8 single crystal, (see Chap. 5). This section gives some background information about the general characteristics of this material. For this purpose, the following references are mainly used: [115, 117, 129].

GaV_4S_8 is a member of the lacunar spinal family of ternary chalcogenides with composition of AM_4X_8, where A = Ga and Ge; M = V, Mo, Nb, and Ta; X = S and Se. The compounds containing Ga are magnetic semiconductors and have at room temperature a non-centrosymmetric cubic structure. In GaV_4S_8 $a = 9.661$ $\mathring{A}$ at room temperature. It undergoes a cubic to rhombohedral transition of the structure at $T_s = 42$ K driven by a cooperative Jahn-Teller distortion. This structural transition produces a stretching of the V_4 tetrahedra along one of the four $\langle 111 \rangle$ crystal directions, as shown in Fig. 2.11(a) and (b). That results in a multi-domain crystal, carrying four different rhombohedral domains. Besides the structural transition, the magnetic properties change from antiferromagnetic to ferromagnetic exchange interaction at $T_c = 13$ K. Hence a single crystal piece can have four regions in which the q vector of the cycloidal phase can point in four different directions. At the same time these four directions can be differently populated. These four different directions are illustrated in Fig. 2.11(c), where the crystal directions are additionally assigned.

Due to a different symmetry of the DMI, GaV_4S_8 hosts Néel-type skyrmions and does not host a conical phase, which is the strongest competing phase in Bloch-type magnets. Therefore, the relative size of the skyrmion lattice in the phase diagram is broader. The periodicity of the skyrmion lattice in GaV_4S_8 is $L_D = 22$ nm. Kézsmárki *et al.* detected the temperature

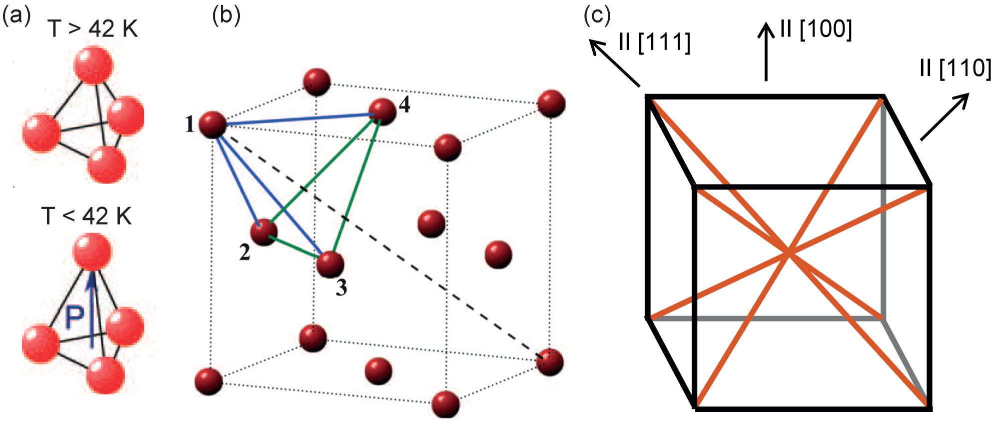

Figure 2.11: Schematic of (a) the structural transition from cubic to rhombohedral of the V_4 cluster (red spheres), (b) the crystal structure of the rhombohedrally distorted structure along one of the body diogonals (dashed line). (c) The four different body diagonals with the various crystal directions assigned. The figures are adapted from [115, 117].

and field dependence by atomic force microscope (AFM) imaging and SANS, and mapped the occurring phase transitions [117]. The phase diagram for three different crystal orientations with respect to the applied magnetic field are shown in Fig. 2.12(a)-(c). Since the direction of the Néel-skyrmions in GaV_4S_8 is given by the magnetic easy axis and not by the field direction, different magnetic field values are observed for the same phase transition in the various orientations. In GaV_4S_8 the magnetic easy axis and the $\langle 111 \rangle$ crystal directions are the same. As mention before, four different crystal directions can be present to the same time in a single crystal sample, caused by the structural transition. The angles between the $\langle 111 \rangle$-axes are 70.5°. Crucial, at which applied magnetic field a phase transition of a certain axis occurs, is the projection of the applied magnetic field on this axis. Since, the projection of the magnetic field on the various axes is different depending on the orientation of the crystal, multiple switching of the same phase transition at different values can occur, as in the case shown in Fig. 2.12(a). In order to account for this behavior, the transitions can be plotted as a function of the projection of the applied field on the magnetic easy axis, as shown in Fig. 2.12(d).

These results from some of the few existing studies show the complexity of these materials. In general, magnetic materials which are hosting Néel-type skyrmions are not yet studied intensively but they are of interest indeed, since skyrmions in GaV_4S_8 have a sizeable electric polarization, they could be controlled with an electric field, which makes them a suitable candidate for potential applications, as for instance as a carrier of information in a magnetic storage media. GaV_4S_8 is a material characterized by a complex

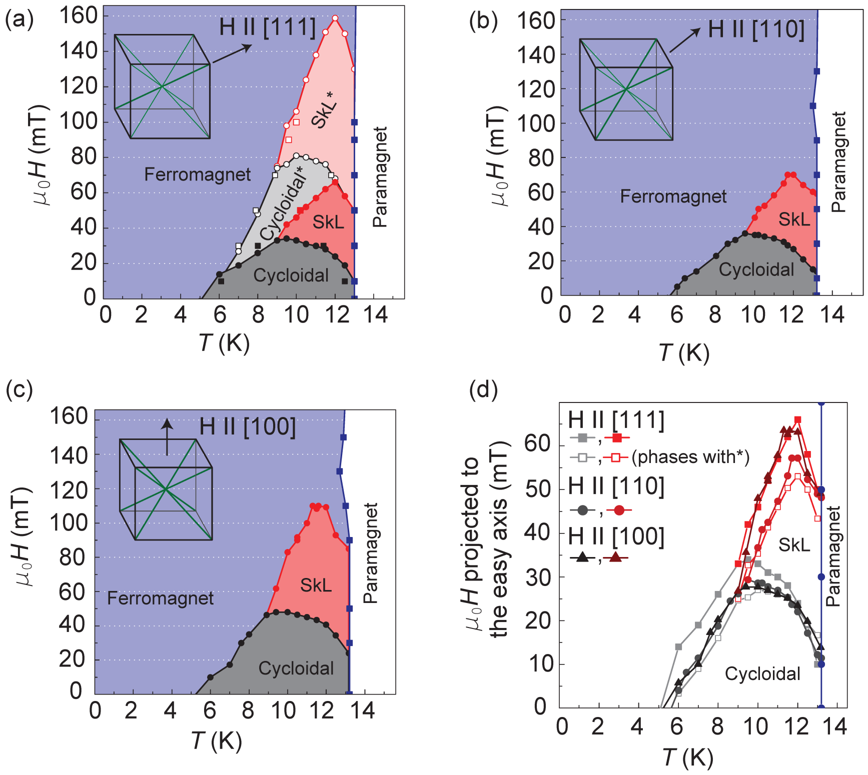

Figure 2.12: (a) -(c) phase diagram as a function of temperature and applied magnetic field for GaV_4S_8 for different orientations of the crystal with respect to the applied magnetic field. Information were obtained via AFM imaging and SANS measurements. (d) phase diagram as a function of temperature and the projection of the applied magnetic field to the easy axis calculated from (a)-(c). The plot is adapted from [117].

interaction between microstructure and chiral magnetism. For instance, it is not yet resolved what is the maximum field angle under which the skyrmion lattice is still formed. This depends on the strength of the uniaxial anisotropy, which to the author‘s knowledge, is still unknown.

In order to quantify and understand the role of the anisotropy in materials hosting Néel-type skyrmions, we perform DCM on a single crystal samples of GaV_4S_8. Furthermore, we compare DCM results with a theoretical model of the magnetic phase diagram as a function of applied magnetic field magnitude and direction. By collecting magnetic torque signal for a series of applied field orientations, DCM reveals the magnetization, anisotropy, and magnetic phase diagram of our sample. The samples and experimental results are presented in detail in chapter 5.

3 Observation of Magnetization Reversal Nucleation Induced by Vortices in Individual Ferromagnetic Nanotubes

The previous chapter introduces the technical aspects regarding the investigation of magnetic samples by DCM, including numerical simulations. The focus in this chapter is on the investigation of the magnetic behavior of CoFeB NTs, depending on their aspect ratio. FM NTs are of interest due to their shape and relative small size, as they would be easier and denser to implement compared to bulk samples in applications like high-density magnetic storage media [8]. Their quality is also higher due to less stacking faults and impurities. Furthermore, FM NTs form flux-closure configurations, which produce a minimal stray-field and therefore reduce the interaction to neighboring structures [9].

In the following, we first present the study of different sized NTs by DCM, then we show the first data obtained by RCM measurements, and afterwards we present the data collected with XMCD-PEEM studies. The results obtained by DCM and XMCD-PEEM studies are compared to corresponding numerical simulations.

3.1 DCM of CoFeB Nanotubes

Due to their high surface-to-volume ratio, magnetization reversal in magnetic nanostructures is often dominated by the influence of surface and edge domains. As a result, surface imperfections and roughness can impede a controllable, reproducible, and fast reversal process [130,131]. Nanomagnets in flux-closure magnetization configurations, however, are less sensitive to the shape of boundaries, since these configurations close magnetic flux lines within the magnet [132]. In FM NTs, reversal of a uniform axial magnetization has been predicted to nucleate and propagate through flux-closure vortex domains, whose magnetization curls around their axis [34,93,99,133]. Using DCM [25], we observe the distinctive signatures of the appearance and disappearance of these vortices at the beginning and end of magnetization reversal in individual CoFeB NTs. We show that these signatures depend on sample geometry, as expected from numerical simulations. Control of the appearance and circulation of these vortices is promising for producing FM NTs with both tailored and favorable reversal properties. Such developments may have practical consequences in the design of nanomagnetic elements required for future high-density magnetic storage devices.

The results presented in the first part of this chapter are adapted from the following work:

Observation of Magnetization Reversal Nucleation Induced by Vortices in Individual Ferromagnetic Nanotubes
A. Mehlin, B. Gross, M. Wyss, G. Tütüncüoglu, F. Heimbach,
A. Foncuberta i. Morral, D. Grundler, and M. Poggio;
to be published (2017)

3.1.1 Introduction

The study of magnetization reversal in magnetic nanostructures is a topic of major fundamental and practical interest. In particular, a controllable, fast, and reproducible reversal process is crucial for applications in high density magnetic storage. This process, however, is often conditioned by the presence of edge and surface domains. Near borders, magnetization tends to change direction in order to minimize stray field and therefore magnetostatic energy. As a result, the form of surfaces and edges – including any imperfections or roughness – can determine the configuration of the magnetization in their surrounding. The resulting magnetization inhomogeneities tend to affect the reversal process by acting as nucleation sites for complicated switching processes [132]. Furthermore, small differences in the initial configurations of edge and surface domains can lead to entirely different reversal modes, complicating the control and reproduciblity of magnetic switching [131].

The high surface-to-volume ratio of magnetic nanostructures weakens these effects, which is essential in the design of high-density memory elements. One way to reduce the effect of edges and surfaces on magnetic reversal is to use magnetic structures that support flux-closure magnetization configurations. Since these configurations minimize stray fields, edges and surfaces play a minimal role in determining both their equilibrium state and their dynamics. FM NTs are one type of nanostructure supporting such states. In particular, reversal of uniform axial configurations in such NTs has been predicted to nucleate and propagate through vortex configurations, which appear at the tube ends and whose magnetization curls around the axis [34,93,99,133] (more details about the properties of FM NTs are given in Sec. 2.2). Magnetization reversal in FM NTs offers some potential advantages over the equivalent well-understood process in FM NWs: in particular, the core-free geometry of FM NTs has been predicted to favor uniform switching fields and high reproducibility [92, 93, 134]. Here, we show the experimental signatures of this nucleation and show how it depends on the angle of the FM NT ends. Understanding and possibly controlling the switching process in FM NTs is a crucial step in enabling practical applications.

We study magnetization reversal in individual CoFeB NTs using DCM. This technique involves a measurement of the mechanical resonance frequency f of a cantilever, to which the NT of interest has been attached, as a function of an externally applied magnetic field H. The frequency shift $\Delta f = f - f_0$, reveals the curvature of the magnetic energy with respect to sample rotations about the cantilever oscillation axis, as given by Eq. (1.27) (more details in Sec. 1.4). Exploiting the high torque-sensitivity of ultrasoft Si cantilevers, DCM provides information on the saturation magnetization, anisotropy, and the switching behavior of individual FM NTs. We compare these measurements with micromagnetic simulations, predicting both DCM signal and magnetization configuration for the experimental conditions. This comparison allows the identification of features in the DCM data with changes in the magnetization configuration, including the nucleation of end vortices marking the beginning of the magnetization reversal. The hybrid finite/boundary element simulations are carried out using the software package *mumax*^{3}, which numerically solves the Landau-Lifschitz-Gilbert equation [82].

3.1.2 Samples and Experimental Setup

Individual CoFeB NTs are used to study the magnetic reversal driven by the nucleation and propagation of vortices in FM NTs. These tubes have a CoFeB shell with a thickness of $t_s = 30$ nm, surrounding a GaAs core. The hexagonal GaAs core is grown by molecular beam epitaxy on a Si (111) substrate by using Gallium (Ga) droplets as catalyst. The amorphous and homogeneous CoFeB shell is deposited around the core via magnetron-sputtering [95]. SEMs of the studied NTs reveal continuous and defect-free surfaces, whose roughness is less than 5 nm. The resulting NTs have typically a vertex-to-vertex diameters between 250 and 300 nm and are about 10 μm-long or longer. A sketch of such a NT is shown in Fig. 3.1. Similar NTs were previously studied by anisotropic magnetoresistance measurements [95, 107] and NTs from the same growth chip were investigated by DCM [25], using longer NTs without any sample processing step, in contrast to the tubes we used. Along with the previous DCM measurements, numerical simulations were performed, describing the

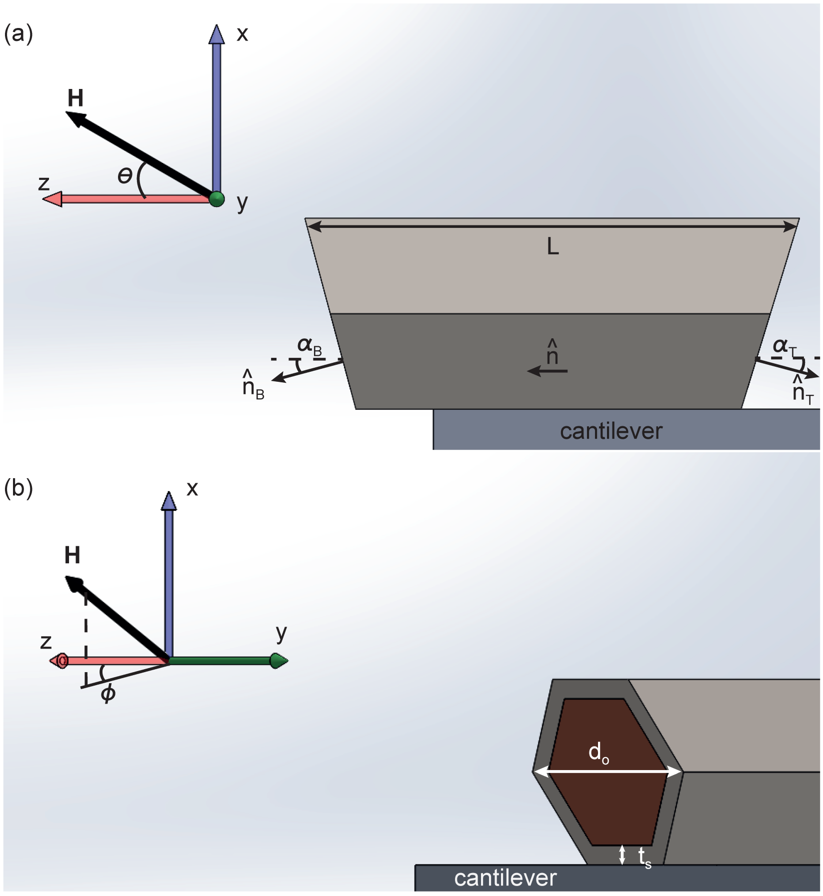

Figure 3.1: Schematic of a CoFeB NT attached to the tip of a Si-cantilever, including the definitions of the direction shown in (a) from the side and in (b) with a slight tilt. The cantilever oscillates in x-direction while the tube axis $\hat{n}$ is assumed to be parallel to $\hat{z}$, as well as to the long axis of the cantilever. The magnetic field direction can be changed in the xz-plane (considering a small misalignment of ϕ), where θ is the angle between the $\hat{z}$-axis and the applied field direction. The top (bottom) end of the NT lies in a plane perpendicular to $\hat{n}_T$ ($\hat{n}_B$) at an angle α_T (α_B) from $\hat{n}$ ($-\hat{n}$)

.

resulting feature in the frequency shift in occasion of a vortex nucleation and extinction at the end of a FM tubular structure. However, the data collected with tubes of length above 6 μm did not show the features, which the numerical calculations predicted. Hence, we repeated the measurements with shorter NTs and, in contrast to the previous samples, the ends of these tubes were well defined. Additionally we have the freedom of changing the direction of the applied magnetic field. In parallel to this work, we investigated the behavior of the CoFeB NTs at remnance by XMCD-PEEM measurements, the results of this study are presented in Sec. 3.3.

We prepared for our studies two samples with different sized ferromagnetic

	Nanotubes	
	NT_a	NT_b
CoFeB NTs		
Length [μm]	2.18 ± 0.03	0.64 ± 0.02
Diameter [nm]	279 ± 6	284 ± 8
Si Cantilever		
Length l [μm]	183 ± 3	151 ± 3
Effective Length l_e [μm]	128 ± 2	106 ± 2
Resonant Frequency f_0 [Hz]	1'954.1	2'799.4
Quality factor Q	10'800	8'000
Spring constant k [μN/m]	~70	70

Table 3.1: Properties of the NTs and the Si cantilevers of both investigated samples. Cantilever properties were determined at around 280 K.

NTs. In order to do that, we placed the tubes by the use of a micromanipulator under an optical microscope on a gold surface. Afterwards we defined the ends and the length under a milling process with a focus ion beam (FIB). This procedure produces tubes with smooth and well-defined ends, which – in general – are tilted relative to the plane normal to the NT axis, as shown in Fig. 3.1(a). In the next step of sample fabrication, we picked up a 2.18 μm-long NT, NT_a, from the surface and attached it to the tip of a ultrasoft Si cantilever with epoxy (Gatan G1) by using precision micromanipulators. Thereby the long axis of the tube was aligned with the long axis of the cantilever. The single-crystal Si cantilever is about 183 μm-long, 4 μm-wide, and 0.1 μm-tick with a 18 μm-long, and 1 μm-thick mass at the tip. Next to the mass-loaded tip is a 12 μm-wide paddle, which serves as a reflective surface in a fiber interferometer used for the detection of the cantilever motion [71], general information about the cantilever is given in Sec. 1.2.1. In order to prepare the second sample NT_b, a FIB-treated CoFeB NT was attached to the end of an about 151 μm-long Si cantilever and oriented so that the long axis of the tube is parallel to the the long axis of the lever. Afterwards a second milling step was performed to shorten the tube to a length of about 640 nm. The second milling step was necessary, since it is nearly impossible to place such a short NT at the tip of a cantilever in the wanted orientation under an optical microscope. The details of the NTs and the corresponding cantilevers are listed in Tab. 3.1.

The DCM measurements are performed in a setup composed of two independent closed-cycle cryostats. We mount the cantilever on a sample stage which is hanging from springs for additional vibration isolation. Such a stage is contained in a vacuum chamber with a pressure below 10^{-4} mbar, at the bottom of a temperature controllable cryostat. This vacuum chamber is surrounded by an independent system, a rotatable 4.5-T magnet. The orientation of the magnetic field can be changed in the xz-plane around the cantilever, whereby the long axis of the cantilever is parallel to the $\hat{z}$-axis and the cantilever oscillates in $\hat{x}$ direction, as illustrated in Fig. 3.1. During the measurement the cantilever's motion is read-out with an optical-fiber interferometer. The laser light of a temperature-tunable laser diode is focused on the 12 μm-wide paddle of the cantilever. The laser diode has a wavelength of 1'550 nm and is operated with a power of about 100 nW. During the measurements, the interferometric deflection signal is fed through an FPGA circuit back to a piezoelectric element, which is mechanically coupled to the cantilever. This provides the possibility to self-oscillate the cantilever at its resonance frequency with a constant amplitude of $x_{rms} \simeq 30$ nm, for which $\theta_c \ll 1°$. The self-oscillation allows faster and accurate detection of the cantilever's resonance frequency.

The Q factors of the Si cantilevers are around 10'000 at T = 280 K, determined through a ring-down measurement. In doing so, we mechanically excite the cantilever with the attached piezoelectric transducer and measure the natural decay of its oscillation amplitude. This decay follows an exponential behavior, with argument inversely proportional to Q [60]. By fitting the data, we obtain Q. The fundamental resonance frequencies are 1.95 and 2.80 kHz, the spring constants are around 70 μN/m, as determined from measurements of the thermal motion. More details about the implemented optical fiber interferometer are given in Sec. 1.2.2, and the used setup and its handling are in detail described in appendix A.

For the numerical simulation corresponding to the investigated samples, we set $\mu_0 M_S$ to its measured value of 1.3 T [25] and the exchange coupling parameter to $A_{ex} = 28\,\mathrm{pJ/m}$ [96]. In the simulations, space is discretized to 5 nm and thermal fluctuations are not included. We obtain for each value of H a map of the magnetization and the expected frequency shift for the DCM measurements (more details are given in Sec. 1.7).

3.1.3 Measurements and Simulations

The aspect-ratio of a magnetic NT has a determining influence on the magnetic reversal process. In particular, FM NTs with a radius larger than a critical value reverse via nucleation of vortex, rather than transverse domain walls [34, 99]. Since this critical radius is about 20 nm for CoFeB (see Fig. 2.5), all experimentally fabricated FM NTs are expected to reverse through vortex domains. For long FM NTs, i.e. 2 μm or longer for our cross-sectional geometry, the expected progression of the magnetization for $\mathbf{H} \parallel \hat{\mathbf{n}}$ (up to a few degrees of misalignment) can be summarized as illustrated in Fig. 3.2 by numerically

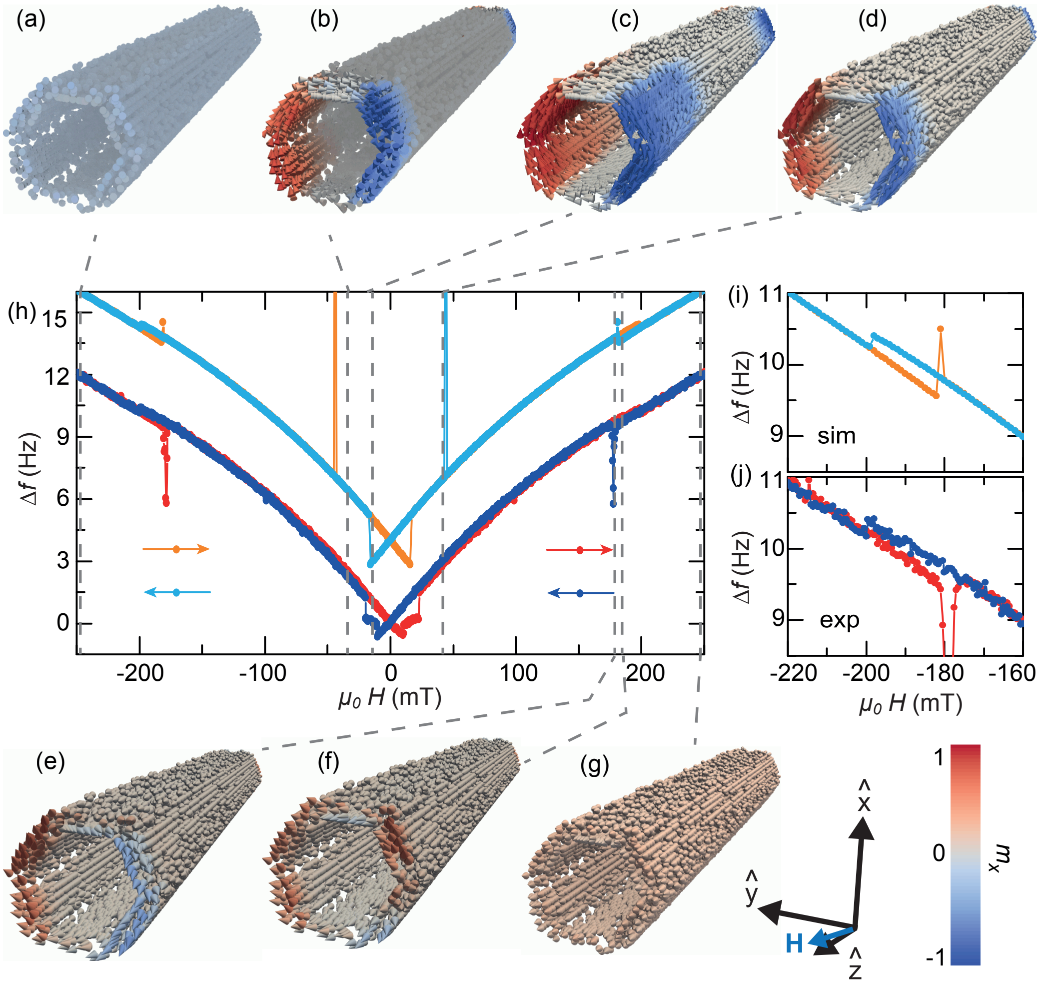

Figure 3.2: (a)-(g) Visualization of the magnetization configuration of a NT, having the same dimensions as NT$_a$. The color-scale corresponds to the normalized magnetization in x-direction. The arrow heads indicate the local magnetization direction. The field values to which the simulations correspond are marked in (h) Δf (H) with gray lines. The detected (simulated) frequency for positive to negative sweep direction is plotted in blue (light blue) and for negative to positive in red (orange). A zoom-in on the region of the vortex nucleation –respectively disappearance– is shown in (i) for the numerical calculations and in (j) the measured signal.

calculated magnetic states. Starting from full saturation at positive H (Fig. 3.2(g)), initially the magnetization at the ends starts to turn (Fig. 3.2(f)), till the first vortex penetrate at the tube ends at a nucleation field [34] of $\mu_0 H \approx 200\,\mathrm{mT}$ (Fig. 3.2(e)) and the second $\mu_0 H \approx 50\,\mathrm{mT}$ (Fig. 3.2(d)). In such long tubes, both relative circulation directions of the end domains have equal energy [98] and which one occurs in experiment is likely driven by imperfections or defects. As H is reduced and reversed, the vortices grow along the tube axis towards the center (Fig. 3.2(c)). Nevertheless, a significant axial domain remains at the switching field of $\mu_0 H \approx -25\,\mathrm{mT}$. At this point, the central axial domain inverts its magnetization direction while the end vortices preserve their configuration. From here on, the vortices shrink in size with progressively larger negative H (Fig. 3.2(b)), until they disappear around $\mu_0 H \approx -50\,\mathrm{mT}$ respectively $-200\,\mathrm{mT}$ and the magnetization approaches saturation (Fig. 3.2(a)).

Fig. 3.2(h) shows DCM measurements of a 2.18 μm-long CoFeB NT, NT$_a$, for $\mathbf{H} \parallel \hat{\mathbf{n}}$ (up to a few degrees of misalignment). Before we collected this data, the system reached a constant temperature and we applied a large external magnetic field, in order to magnetize the CoFeB NT and initialize it in the saturated state. The measurements presented in the following were all performed at T $\approx$ 280 K. Together with the experimental data, Δf (H) obtained numerically is also plotted, and corresponds to the magnetic configurations described before (Fig. 3.2(a)-(g)). For the simulated frequency shift we use Eq. (1.49). Hysteretic step features, highlighted in Fig. 3.2(i) for the simulation and in (j) for the experimental data, indicate the entrance and exit of vortices at the ends in the NT, and therefore define the reversal nucleation field. The measured and simulated features correspond well and their amplitude and the field at which they occur depend on material properties and the geometry of the NT – in particular on the tilt angle of the top α_T and bottom α_B ends with respect to the FM NT axis $\hat{n}$, as illustrated in Fig. 3.1. Note that NT$_a$ measured in Fig. 3.2 has $\alpha_T \neq \alpha_B$, resulting in two distinct entrance and exit fields corresponding to the two different end vortices. One entrance and exit pair is barely visible in both experiment and simulation due the corresponding end's unfavorable orientation with respect to $\mathbf{H}$, as discussed in further detail later. Although simulations of such DCM vortex entrance and exit signatures were already carried out by Gross *et al.* [25], they observed no such features in the measured data, likely because of their imperfect FM NT ends or inappropriate orientation of the ends with respect to $\mathbf{H}$, which could not be adjusted in their case. The overall features of the measured and simulated $\Delta f(H)$ match, including the asymptotic behavior at large $|H|$, and the overall signature of magnetization switching, which occurs around the same value of $H = \pm 20$ mT. Nevertheless, the measured switching response shows two distinct steps interrupted by a plateau-like feature, rather than the single step of the simulations. We return to this difference in our analysis of reversal in a shorter CoFeB NT and suggest potential reasons for this discrepancy.

For shorter tubes – here, CoFeB NTs less than 2-μm-long – a different reversal process emerges, since the two end vortices meet at the center of the tube prior to the magnetization switching. In this case, the two relative vorticities of the end domains lead to two different reversal progressions. Given that end vortices with equal vorticity represent the lower energy configuration in short tubes [98], this configuration and its resulting reversal process should be favored. Nevertheless, images of the remnant magnetization configuration in similar FM NTs by Wyss *et al.* show that both configurations can occur experimentally [98], perhaps due to the influence of sample imperfections, see Sec. 3.3 for more details. As a result, we consider both reversal progressions in our simulations.

For opposing vorticity, as illustrated in Fig. 3.3 (b)-(f), simulations show that after the entrance of the vortices, the central axial domain shrinks until only a domain wall remains to separate the two vortex domains. As H becomes increasingly negative, the axial wall reverses in a series of steps, the vortex domains recede, and finally disappear on the way to magnetization saturation. Magnetization configurations for some notable values of H are shown in Fig. 3.3(b)-(f) and labeled in the corresponding plot of Δf (H) in black in Fig. 3.3(a). Note the large step appearing in Δf close to $\approx -14\,\mathrm{mT}$ (e) to (d), followed by a plateau-like feature including a small step (d) to (c), and a final large step around $-24\,\mathrm{mT}$ (c) to (b). The first discontinuity marks the replacement of the axial domain wall with a Bloch-type vortex wall in the top and bottom facet and Néel-type vortex walls in the four side facets, as shown in detail in Fig. 3.3 (g) and (h). The small intermediate step represents the disappearance of the Néel-type walls, while the final step marks the disappearance of the Bloch-walls and the full reversal of the axial domain wall.

In case of matching vorticity, simulations show a progression, illustrated in Fig. 3.3 (j) to (m), in which the two vortex domains merge at the center of the FM NT, without the need to form a domain wall. The resulting global vortex configuration progressively rotates toward the applied magnetic field, until the vortex domains eventually split and disappear as the FM NT tends towards saturation. Δf (H) for this type of magnetic reversal is plotted in red in Fig. 3.3(a). Between ±25 mT a series of six steps occurs. Each of these features correspond to the inversion of the magnetization along one of the 6 tube edges from parallel to anti-parallel with $\mathbf{H}$. Such a change in configuration is illustrated in Fig. 3.3 (j) to (l) for the step around 6 mT.

Simulations therefore predict distinct reversal modes for short FM NTs with different relative vorticities, resulting in two different shaped Δf (H)

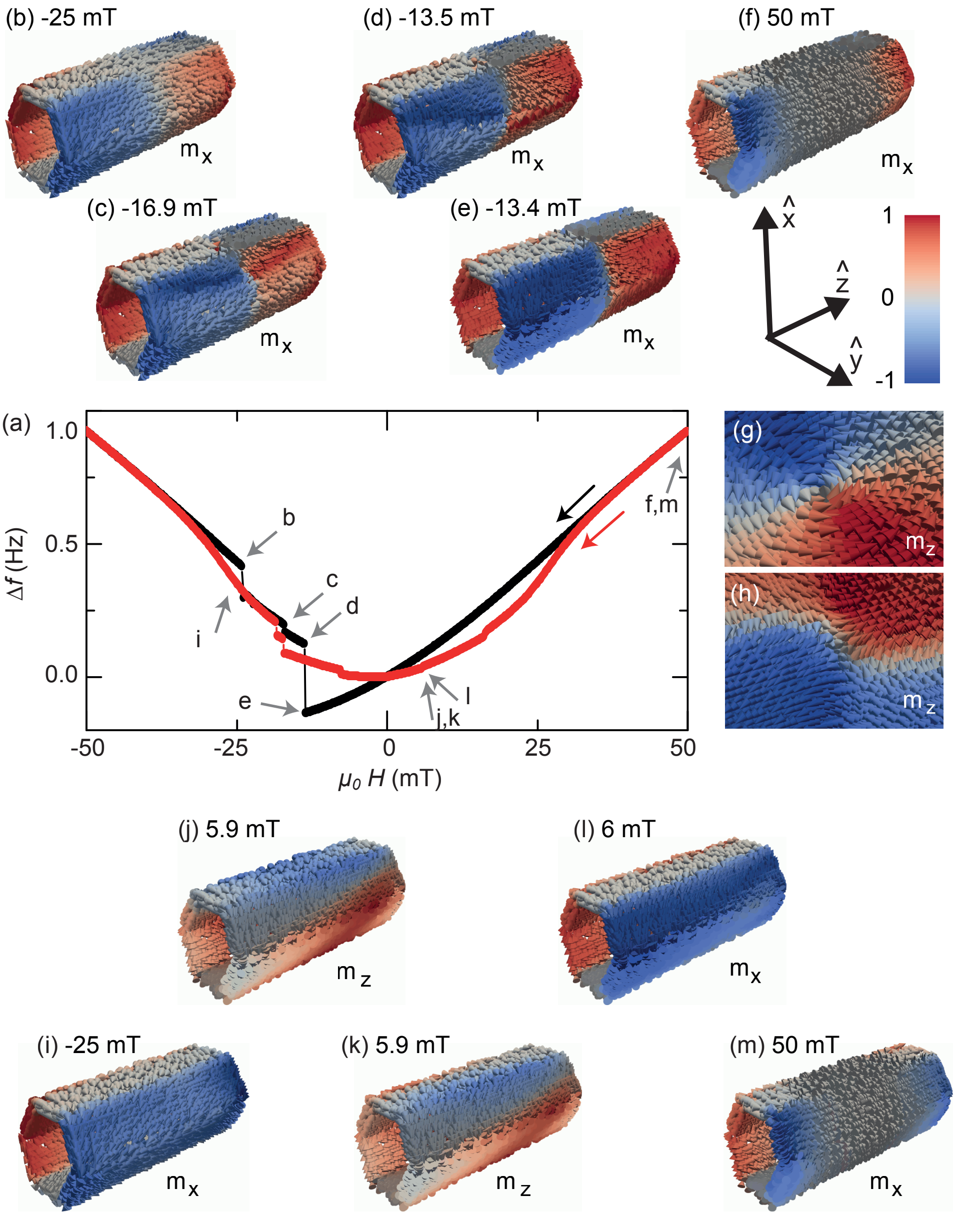

Figure 3.3: (a) Δf (H) numerically calculated in case of opposing vortex (black) and for a global vortex (red) for a tube with the same dimension as NT$_b$. Assigned are the different magnetic configurations, which are visualized in (b)-(e) when the tube passes trough an opposing vortex configuration and in (i)-(m) trough a global vortex. Visualization of (g) a Bloch type and (h) a Néel-type vortex wall. The color-scale corresponds to the normalized magnetization in x-direction, respectively in z-direction. The arrow heads indicate the local magnetization direction.

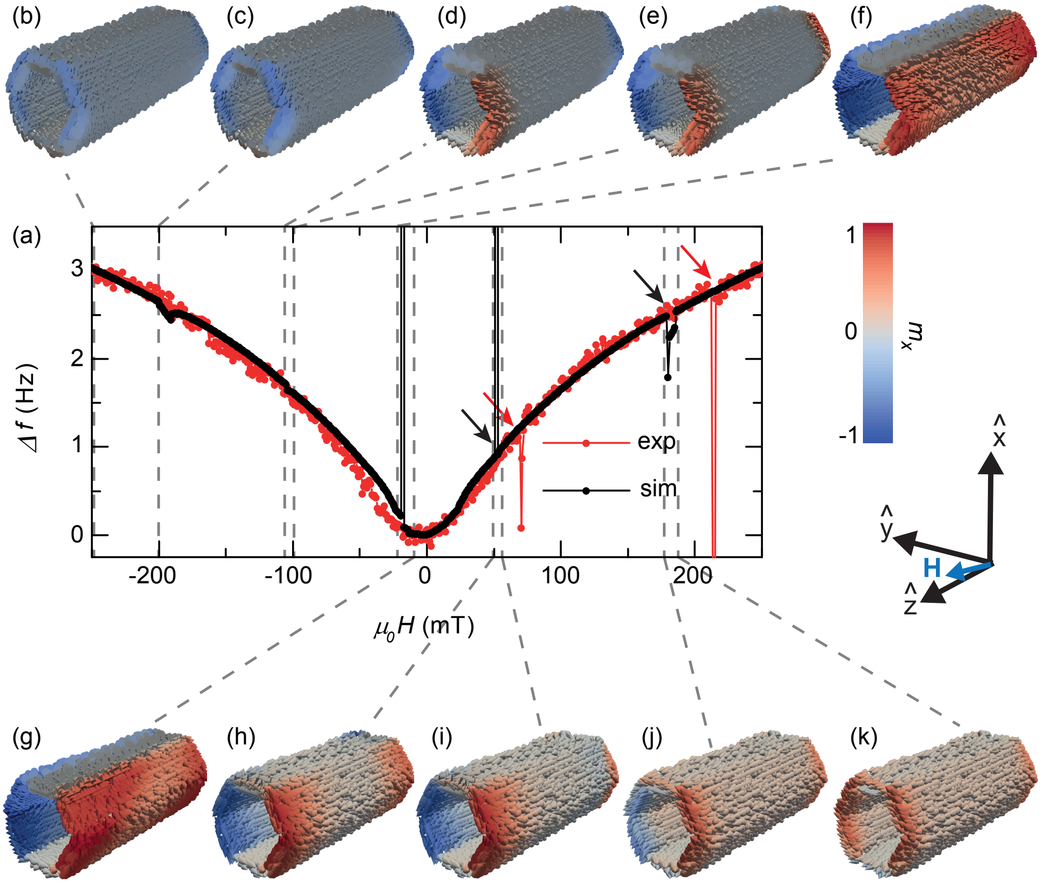

Figure 3.4: (a) Dependence of the frequency shift on an applied magnetic field, sweeping from positive to negative field. Δf (H) for NT$_b$ at T = 280 K in red and in black the result of the corresponding simulation. The arrow in the corresponding colors mark the nucleation of the first vortex at ~200 mT and the second at ~75 mT. (b)-(k) Visualization of the magnetization configuration of a NT, having the same dimensions as NT$_b$. The color-scale corresponds to the normalized magnetization in x-direction. The arrow heads indicate the local magnetization direction. The field values to which the simulations correspond are marked in (a) Δf (H) with gray lines.

for both cases, see Fig. 3.3(a). For the study of the magnetic reversal of a shorter tube we investigate the behavior of a 640 nm-long CoFeB NT, NT$_b$. Figure 3.4(a) shows the measured (red) DCM response of NT$_b$ by sweeping the magnetic field from positive to negative in combination with the results of the corresponding simulations (black). In addition for a few interesting field values the corresponding numerically calculated magnetic states are shown in (b)-(k). The magnetic progression of this 640 nm-long NT can be summarized as follows: starting from full saturation at positive H, at some point the magnetization at the ends starts to turn (Fig. 3.4(k)) and the first vortex penetrates at one tube end at a nucleation field of $\mu_0 H \approx 180$ mT (Fig. 3.4(j)). This vortex grows along the tube axis towards the center (Fig. 3.4(i)) and after a while the second vortex penetrates at $\mu_0 H \approx 50$ mT (Fig. 3.4(h)). Both vortices continue growing towards the center till a global vortex is formed (Fig. 3.4(g)). The step around -20 mT is illustrated in Fig. 3.4(g) to (f), and corresponds to the inversion of the magnetization along one of the tube edges from parallel to anti-parallel with $\mathbf{H}$, as described previously. Afterwards the two vortex domains split (Fig. 3.4(e)) and one (Fig. 3.4(d)) after the other disappears (Fig. 3.4(c)). The behavior matches the progression starting with matching vorticity, passing through a global vortex state. Most notably, the measured $\Delta f(H)$ never drops below zero, as expected for the progression with equal vorticity, in contrast to the case of opposing vorticity. Less pronounced, but also recognizable, is the round shape of the experimental curve around zero field, again agreeing with equal rather than opposing case. Entrance and exit of the two end vortices in the measurements also follows expectation, as indicated by the arrows. Although a reversal mode nucleated by opposing vortices was not observed by repeating the measurements several times, it cannot be ruled out as a possibility in similar samples, since Wyss *et al.* observed remnant opposing vortex states in similar-sized FM NTs by XMCD-PEEM imaging [98], as presented in Sec. 3.3. Note, however, that the plateau-like feature present in $\Delta f(H)$ in the simulations of short CoFeB NTs with opposing vortices, resembles a feature observed in experiments on long tubes, e.g. the 2.18-μm-long NT in Fig. 3.2. These features, which were not present in corresponding simulations of long FM NTs, had previously been speculated to indicate a global vortex configuration. Given that simulations on short NTs with matching vortices show that the switching via global vortex state shows an always positive and roughly parabolic $\Delta f(H)$ near $H = 0$, this hypothesis can be ruled out. On the other hand, the resemblance of these plateaus to those in simulations of reversal in short FM NTs with opposing vortices may indicate the formation of Bloch and/or Néel-type vortex walls similar to those depicted in Fig. 3.3(g) and (h).

As mentioned previously, one entrance and exit pair of vortices is barely visible in both experiment and simulation of the 2 μm-long NT, as shown in

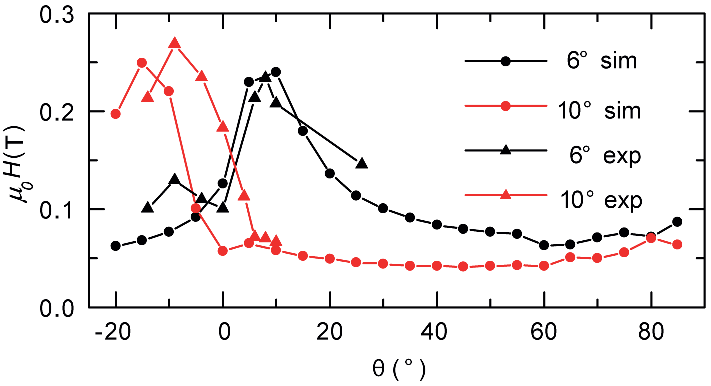

Figure 3.5: Entrance field of the vortices in the two different slanted ends as a function of applied magnetic field angle resulting from simulations (●●) and experiments (▲▲).

Fig. 3.2(f). It seems that the ends of the CoFeB NT determine the vortex entry process and thus the reversal nucleation field. In particular, we observe that the orientation of the plane in which the ends lie ($\hat{n}_T$ and $\hat{n}_B$) with respect to $\hat{n}$ and $\mathbf{H}$ sets the entrance and exit fields as well as the magnitude of its signature in $\Delta f(H)$. We studied this effect in more detail by measuring DCM in the 640 nm-long FM NT as a function of θ, the angle of $\mathbf{H}$ with respect to $\hat{z}$. We chose the shortest measured NT, since vortex entry and exit features are more prominent in this sample, likely due to the larger relative sample volume occupied by the vortex domains compared to longer FM NTs. Fig. 3.5 shows the experimentally determined and simulated entrance fields H_{en} of the top (bottom) vortex domain in black (red) as a function of θ. Note that the corresponding exit fields H_{ex}, which are not shown, are slightly higher, but behave analogously. In the simulations, we tune the geometrical parameters of the FM NT to match the measurements within the range of what is reasonable by the SEMs of NT$_b$ in question, resulting in: $d_o = 284\,\text{nm}$, $t_s = 30\,\text{nm}$, $\phi = 0°$, $\alpha_T = 6°$, $\alpha_B = -10°$ (see Fig. 3.1 for the definition of the angles).

Measurements and simulation show that H_{en} peaks near $\theta \simeq \alpha_{T/B}$, i.e. $\mathbf{H} \parallel \hat{n}_{T/B}$. Upon slight tilting of $\mathbf{H}$ from this condition, H_{en} reduces and eventually approaches about one fifth of its maximum value at large misalignment angles. The magnitude in Δf of the entrance features also depends on θ, as shown by both experiments and simulation. The features vanish as soon as θ deviates from the alignment with α_T and α_B. The excellent agreement of the dependence of these features on the direction and size of $\mathbf{H}$ suggests that the simulated reversal nucleation is an accurate description of the process occurring in the measured CoFeB NT samples.

3.1.4 Discussion and Conclusion

The presented DCM measurements, in combination with the corresponding numerical simulations, confirm that the magnetic reversal is driven by vortex nucleation at the end of FM NTs, as theoretically predicted by Landeros *et al.* [93]. Additionally we have shown the importance and influence of the shape of the ends on the vortex nucleation event, which has not been observed until now. Furthermore, the presented measurements and numerical simulations are in good agreement to previous theoretical predictions [34] and experimental work [98]. We have found the 2 μm-long tube in a mixed state, with vortices at the end and an axial domain in the center and the shorter 640 nm-long NT in a global vortex state.

In conclusion, our findings highlight the importance of the NT ends in determining the reversal process. Since even slightly tilted ends shift the nucleation fields, control of their geometry is crucial for achieving a predictable reversal process. Nevertheless, if nearly ideal nanostructures can be achieved, it is now clear that by simply tuning the geometry of a FM NT, one can tailor its magnetization reversal process, which occurs – as predicted – through vortex configurations. This experimental confirmation sets the stage for the realization of FM NTs with fast and highly reproducible switching behavior. The detailed understanding of the reversal process and equilibrium magnetization configurations gained here, may also allow for the programming of stable flux-closure magnetization configurations through structural asymmetries [135]. Information encoded in arrays of FM NTs in such configurations could achieve unprecedented densities for magnetic storage, due to the absence of stray field interactions [9].

In the following sections, we describe the investigation of NT$_a$ performing RCM measurements, obtaining direct access to the magnetization in two directions. Afterwards we present the results of the XMCD-PEEM studies made with CoFeB NTs from the same growth chip, investigating the remnant magnetic state.

3.2 Resonance Cantilever Magnetometry

In section 1.5 we showed that by implementing in the setup two coils generating an AC magnetic field at the cantilever's resonance frequency and detecting the amplitude of the magnetically driven response, we obtain access to M_z and M_x, and increase the setup's sensitivity at low magnetic field. In this section we describe in detail how we implement RCM and show the first

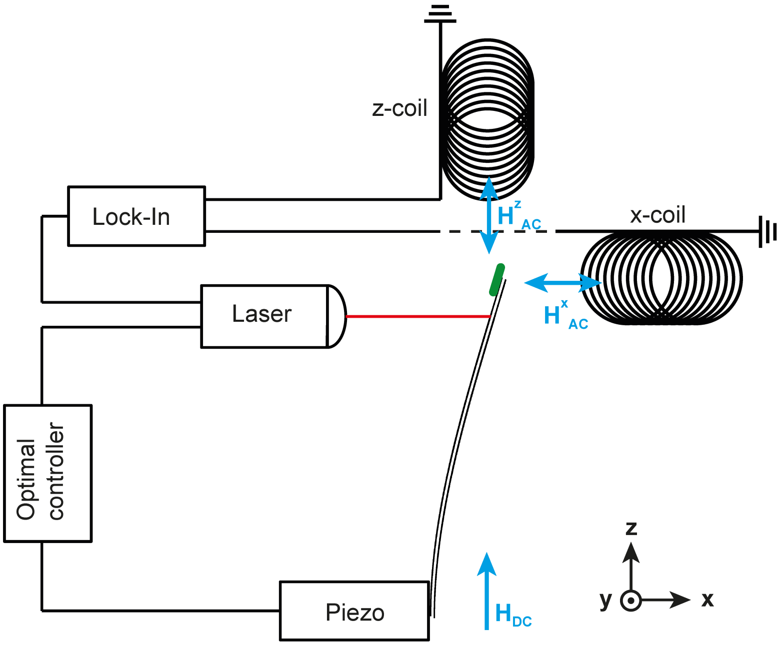

Figure 3.6: Schematics of the implemented RCM setup. A detailed description is given in the text. Information about the implemented fiber-interferometer is given in Sec. 1.2.2.

results obtained with this method.

3.2.1 Setup Description

The same setup as for the DCM studies is used, with the addition of two small coils mounted close to the cantilever, as shown in Fig. B.1(b). A schematics of the experimental arrangement used for RCM measurements is shown in Fig. 3.6, which we illustrate in detail in the following.

Before we start measuring, we bring the system to a constant temperature and apply a large external magnetic field, so that the magnetization of the NT points completely along the field direction. In this situation we start to measure: first we determine the angular resonance frequency $\omega_m(\mathrm{H})$ by detecting the thermal motion via an optical fiber interferometer, as described in Sec. 1.2.2. The next step would be to apply an AC magnetic field $\mathbf{H}_{AC}$ at ω_m and determine the response amplitude $\tilde{x}(\omega_m)$. Since the cantilever acts like a sharp frequency filter, it is necessary to apply precisely the AC field at its resonance frequency: this is difficult because, by applying $\mathbf{H}_{AC}$, a small resonance shift of the cantilever can occur due to a non-matching phase of $\mathbf{H}_{AC}$ and ω_m, or through the reaction of the magnetic sample on $\mathbf{H}_{AC}$. In order to overcome this problem, we damp the cantilever's motion, resulting in a broaden spectrum. For this procedure we use an optimal controller, which amplifies the detected interferometer signal [136, 137]. The concept of the optimal cantilever control was developed for an improved time response of cantilevers used for force microscopy, as for instance in MRFM studies [136, 137]. In our experiment optimal controller is implemented in an FPGA, generating a transfer function based on the measured cantilever properties [60]. The transfer function is sent to a piezoelectric element, which is mechanically coupled to the cantilever. The phase of the optimal control feedback is chosen so that the cantilever's motion is damped.

Due to the damping the cantilever acquires an effective Q of about 600, which is kept constant during a set of measurements. The cantilever's spectrum results therefore broadened and it is easier to hit the cantilever's resonance frequency with the applied AC field. For optimization reasons we repeat the following procedure: we read-out ω_m(H) of the damped cantilever and update the parameters of the optimal control feedback loop. Afterwards we apply via a lock-in amplifier $\mathbf{H}_{AC}$ to the x-coil, which generates a small field in $\hat{\mathbf{x}}$ direction, the coordinate system to which we refer is shown in Fig. 3.6. We obtain the amplitude response $\tilde{x}_{x-coil}(\omega_m)$ by reading-out the interferometer signal with a lock-in amplifier. The same procedure is repeated for the second coil. We apply $\mathbf{H}_{AC}$ to the z-coil, generating a small field in $\hat{\mathbf{z}}$ direction and determine with the lock-in amplifier $\tilde{x}_{z-coil}(\omega_m)$.

The coil amplitude has to be chosen wisely, since a too high value results in losing signal into higher harmonics of ω_m. For instance we observed, that if a sinusoidal curve result for $\tilde{x}_{coil}(H)$, the amplitude is most probably too high. This setup could also be used for phase-locked cantilever magnetometry (PLCM) measurements which is a variation of the 3$^{\text{rd}}$ mode [79]. For PLCM measurements the cantilevers response to an externally applied field which has a well-defined phase with respect to the cantilevers position. In contrast to RCM no damping of the cantilever but a well-controlled phase is needed and similar results should be obtained. In our setup the PLCM measurements were more sensitive to noise, hence we focused on RCM.

In the next section we present our first experimental results, which we obtained by the use of RCM on the 2 μm-long CoFeB NT, NT$_a$, previously investigated by standard DCM.

3.2.2 RCM Measurements

In this section we present our first results obtained by embedding RCM measurements in our study of magnetic samples. Using this method we investigate the longer of the two tubes which was studied by DCM and presented at the beginning of this chapter. We focus only on the low-field range (±50 mT), since this is the region in which RCM provides additional information, since in the high field range the signal is supposed to approach

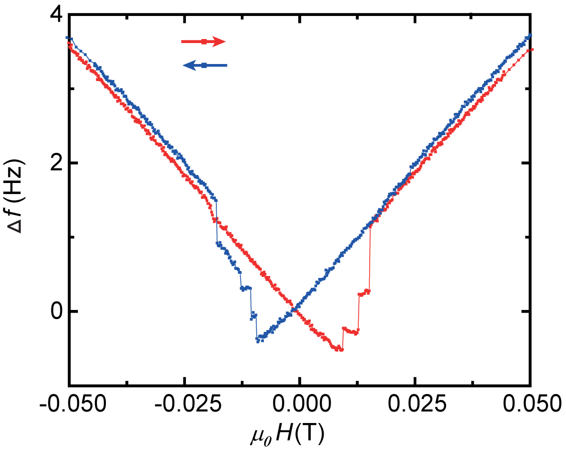

Figure 3.7: Δf(H) with $\mathbf{H}$ parallel to the long axis of the 2.18-μm long CoFeb NT at T = 278 K for the low magnetic field range.

zero, for more details see Sec. 1.5.

For the measurements the long axis of the NT is parallel to the DC magnetic field and T = 278 K. We follow the procedure described in the previous section. By applying a current at ω_m to both coils, successively, we reach an AC magnetic field of about 24 μT at the cantilever's position. Before we start damping the cantilever's motion, additionally for each value in H, we collect data in the normal DCM mode. A full set of data consist of Δf(H) determined by standard DCM, plus $\tilde{x}_{x-coil}(\omega_m)$ and $\tilde{x}_{z-coil}(\omega_m)$ as a function of the applied magnetic field obtained by RCM measurements. Δf(H) obtained by DCM is plotted in Fig. 3.7, looking similar to what we have seen before for the same NT (Fig. 3.2(h)), and is collected to double-check if the measurement is running without any disruption. The slight differences in the plots can be caused by a slightly different orientation of the tube with respect to the applied magnetic field and also T can differ by a few Kelvin. According to the equations (1.44) and (1.45), the amplitude response of the applied AC field at ω_m of $\tilde{x}_{x-coil}(\omega_m)$ and $\tilde{x}_{z-coil}(\omega_m)$ is proportional to M_z and M_x, respectively. Hence we obtain directly access to two directions of the sample's magnetization. Figure 3.8 shows in (a) M_z(H) as a response of the x-coil and in (b) M_x(H) as a response of the z-coil. M_z for our FM tube has the behavior expected from the literature, as shown in Ref. [25]. The easy axis of the tube is parallel to the applied magnetic field and this configuration, combined with the strong shape anisotropy of the NT, keeps all the magnetic moments parallel to $\mathbf{H}$ for the majority of the magnetic field range. The magnetic reversal for this sample occurs at about ±15 mT. The reversal takes place over three (red) respectively four (blue) distinct steps ending with a final irreversible magnetization switch, as shown in Fig. 3.8(a).

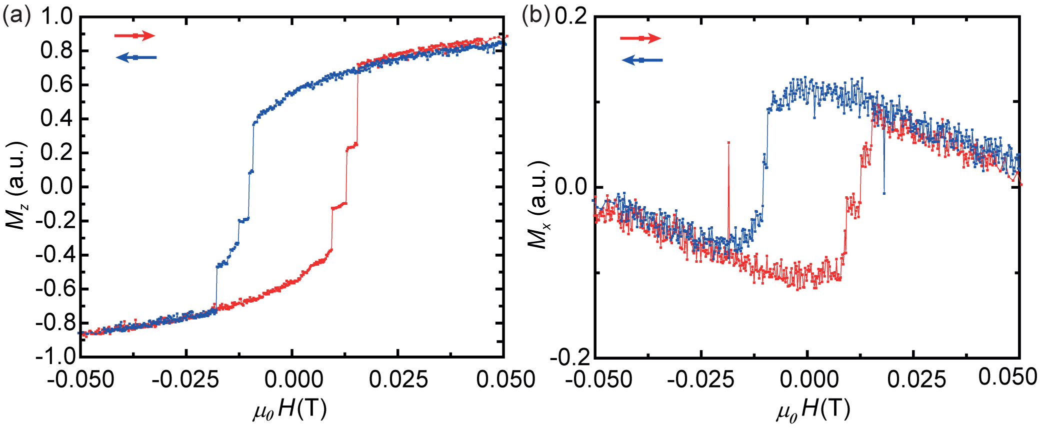

Figure 3.8: (a) M_z (H) measured as the amplitude response of the x-coil and (b) M_x (H) the response of the z-coil of a 2.18 μm long CoFeB NT at T = 278 K. Both signals were normalized by using the same parameters.

The M_z-hysteresis curve in the low-field regime is similar to the one presented by Gross *et al.* [25], which is directly calculated from Δf(H) for a longer CoFeB NT originating from the same growth chip.

The response of the z-coil is shown in Fig. 3.8(b). For M_x for a FM tube in this configuration, no or only a small signal would be expected, but instead we obtain a significant signal. Comparing Fig. 3.8 (a) and (b), respectively M_x and M_z, we observe that the overall shape is similar at low field. The strength of M_x is more than 7 times lower than M_z, so significantly reduced, but the same features appear at the same field values. Furthermore M_x(H) and as well M_z(H) (for higher fields, here not shown) do not approach a horizontal line as expected for a standard hysteresis curve of a FM and also do not approach 0 as expected for this method, as described in Sec. 1.5.2. Instead the response of both coils (for high enough fields) shows a linear behavior with a negative slope crossing zero, as visible in the signal obtained by the z-coil, plotted in Fig. 3.8(b). For the x-coil this behavior appears at $\mu_0 H \approx 0.1$ T, above the field region shown here.

Several factors could cause the unexpected behavior which we observe. The peculiar amplitude response of the z-coil resulting in a signal in M_x(H) can occur due to a misalignment of the coils with respect to the sample. The coils are in a fixed position which we cannot correct easily and a misalignment of a few degrees is possible. Another reason can be a non-homogeneous AC field of the coils caused by a non-perfect shape. The coils are winded by hand, so small irregularities can easily occur. Furthermore the cantilever is placed in front of the coils and not in the center so that the field direction and intensity differ from what expected.

The unexpected linear response at higher field could be due to para- or diamagnetic contribution, probably originating from the GaAs core of the NT. Furthermore magnetic impurities of any kind can influence the signal and change the high-field behavior. Impurities can be present in the cantilever and also in the sample itself. Furthermore, we assume that the cantilever's Q is constant throughout the entire field range. Since Q can have a dependence on the magnetic field also caused by the attached sample, this assumption is not always fulfilled, especially for a wider field range. Due to this, the damping is possibly not constant over a broad field range, which has an influence on the measured response amplitude, since $M_{z/x}$ is proportional to $1/Q$, as shown in Eq. (1.44) and (1.45).

Despite the disagreements, we have shown that from measurements made in RCM mode we obtain direct access to two directions of the magnetization of the sample. Using the DCM mode we obtain only information about the average magnetization. In addition, we obtain also information about para- or diamagnetic components of the sample. Especially for small samples for which the sensitivity of DCM is not sufficient, or for more complex structures, this variation could give a better understanding of the magnetization and the reversal processes at small magnetic fields.

3.3 Imaging Magnetic Vortex Configurations in Ferromagnetic Nanotubes

CoFeB NTs from the same growth chip used for the experiments presented previously in this chapter, were also investigated through XMCD-PEEM. XMCD-PEEM studies investigate the different absorption of left and right circular polarized photons of magnetic materials. This technique is sensitive to specific FM materials by selecting the photon energy depending on the FM material of interest [42]. Using this technique we image the remnant magnetization configuration of the tubes. The images provide a direct evidence for flux-closure configurations, including a global vortex state, in which the magnetization points circumferentially around the axis of the NT. In addition we performed numerical simulations, predicting that vortex states can be programmed as equilibrium remnant magnetization configurations by reducing the NT aspect ratio, and such prediction has been confirmed by our measurements.

The results presented in this section are adapted from the following publication:

Imaging Magnetic Vortex Configuration in Ferromagnetic Nanotubes

M. Wyss, A. Mehlin, B. Gross, A. Farhan, M. Buzzi, A. Kleibert, G.

Tütüncüoglu, F. Heimbach, A. Foncuberta i. Morral, D. Grundler, and M. Poggio;
Phys. Rev. B **96**, 024423 (2017) [98]

3.3.1 Sample and Measurement Setup

For the study of the size-dependence of the remnant magnetic state, we investigate FM tubes having diameters between 200 and 300 nm, and lengths from 0.5 to 12 μm. In the following we present the data of three different sized CoFeB NTs, originating from the same growth chip as the tubes studied with DCM measurements, described previously. General details about the NTs are given in Sec. 3.1.2.

The different lengths were achieved by a FIB milling process. Afterwards, the NTs were placed with precision micromanipulators under an optical microscope on a Si substrate. The three different NTs have the following lengths L and diameters d: NT1: L= 7.2 μm, d = 265 nm; NT2: L = 1.06 μm, d = 283 nm; and NT3: L = 0.83 μm, d = 236 nm. These sizes were determined by SEM.

The measurements were performed at the Surface/Interface: Microscopy beamline of the Swiss Light Source (SLS) at the Paul Scherrer Institute. The data were collected at room temperature and in remnance. Circularly polarized X-rays tuned to the L_3-edge of Fe and propagate along direction $\hat{k}$. The X-rays impinge on the Si sample substrate with an incident angle of 16°, as schematically shown in Fig. 3.9. The setup provides the possibility to rotate the sample in the plane of the Si substrate with respect to $\hat{k}$, which is fixed. In order to obtain the XMCD-PEEM images, the difference between the images obtained with X-ray of opposite helicity σ^+ and σ^- is taken and normalized to their sum: $I_{\mathrm{XMCD}} = (I_\sigma^+ - I_\sigma^-)/(I_\sigma^+ + I_\sigma^-)$, where $I_\sigma^\pm$ is the emission intensity of the photoelectrons, which is proportional to the local absorption cross-section of $\sigma^\pm$ polarized X-ray illumination. The XMCD-PEEM contrast is due to the fact that $I_\sigma^\pm$ is proportional to the intensity of the incident $\sigma^\pm$ X-rays and to their absorption. The absorption of the $\sigma^\pm$ X-rays is proportional to the projection of the magnetic moment along $\hat{k}$. Hence, positive (red) or negative (blue) I_{XMCD} depict near-surface magnetization either parallel or antiparallel to $\hat{k}$, respectively, as for example illustrated in Fig. 3.9. The photoemission signal due to X-rays which have previously passed through magnetic material is influenced by absorption in the traversed volume [138–140]. Since, as mentioned before, the absorption of $\sigma^\pm$ X-rays is proportional to the projection of the magnetic moment along $\hat{k}$, then also a proportionality exists to $\sigma^\pm$ X-rays transmitted through the NT, which reveals in the X-ray shadow of the NT on the Si substrate, which is non-magnetic. Therefore the obtained $I_\sigma^\pm$ is proportional to the magnetization

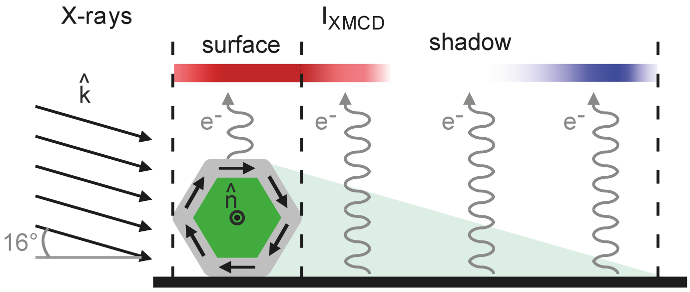

Figure 3.9: Schematics of a NT cross-section, including X-rays with an incident angle of 16°, the photoexcited electrons and the expected XMCD-PEEM contrast for a vortex state. The magnetic tube is made of a non-magnetic GaAs core (green), surrounded by a CoFeB shell (grey).

of the volume crossed by the X-rays. This proportionality has opposite sign compared to that at the magnetic surface, i.e. positive (red) or negative (blue) I_{XMCD} results from the volume magnetization either anti-parallel or parallel to $\hat{k}$, respectively, as illustrated in Fig. 3.9. From the combination of these two types of contrast, we obtain information about both the surface and volume magnetization of the measured NTs [138]. The obtained images have a spatial resolution of roughly 100 nm, which depends on the quality of the focus and the properties of the sample, including morphology and cleanliness.

3.3.2 Measurements and Simulations

In section 2.2 we have described that, according to theoretical predictions of Landeros *et al.* [34], three different magnetic configurations for FM NTs exist. Based on this work a phase diagram of those magnetic states as a function of tube length and outer diameter for CoFeB NT, having a 30 nm thick shell was shown in Fig. 2.5. In order to confirm the analytical theory with experimental studies, we investigate three different sized NTs, determining the equilibrium magnetic state by using XMCD-PEEM.

In Fig. 3.10 the XMCD-PEEM images of NT1 are shown with (a) the long axis of the NT $\hat{n}$ perpendicular to $\hat{k}$ and in (b) parallel to $\hat{k}$. The dashed contour lines indicate the position of the tube, which was determined by overlaying a SEM, a PEEM and a XMCD-PEEM image of the same NT. The I_{XMCD} in the region defined by the contour line arises from the top of the NT within 3 to 5 nm of the surface and is proportional to the projection of its local magnetization along $\hat{k}$. From Fig. 3.10(a) we see from the contrast, especially in the shadow, that the magnetization is perpendicular to $\hat{n}$ at the ends of the NT. Comparing this to Fig. 3.10(b), for which we rotated the stage to have $\hat{k} \parallel \hat{n}$, we observe a strong contrast in the central part of the NT, due to a parallel alignment of the magnetization with $\hat{n}$. A reduced contrast

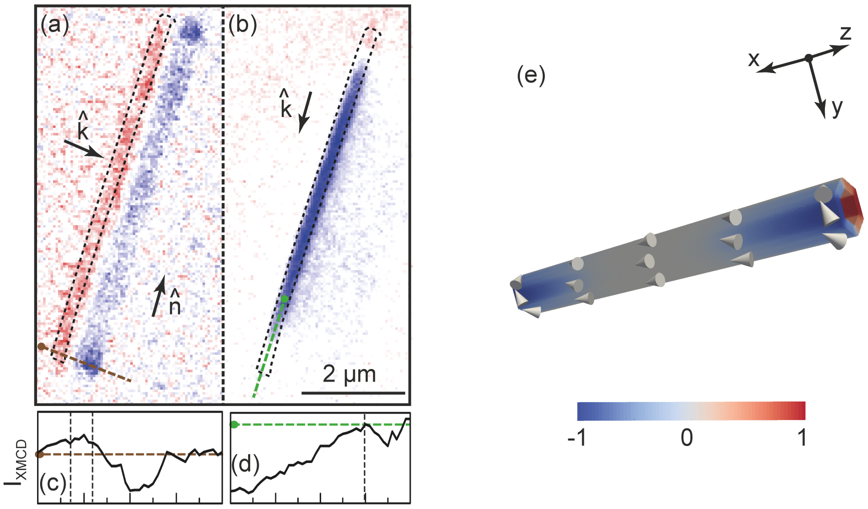

Figure 3.10: XMCD-PEEM images of NT1 for (a) $\hat{k}$ perpendicular to the long axis of the NT $\hat{n}$ and (b) $\hat{k}$ parallel to $\hat{n}$. The dashed contour lines indicate the position of the NT. The red (blue) contrast represents positive (negative) I_{XMCD} signal. (c) and (d) are 2μm-long I_{XMCD} line cuts corresponding to the colored dashed lines shown in (a) and (b). The background intensity in the line cuts is indicated by the level of the horizontal lines, and the vertical lines indicate the position of the NT. In (e) a simulation of the remnant magnetic state of a 2.1 μm-long and 245 nm-wide NT is shown. The NT is in a mixed state, having an axial central domain and vortex at the ends with matching circulation, matching with the measured NT shown in (a) and (b). The color-scale corresponds to the normalized magnetization in y-direction. The arrow heads indicate the local magnetization direction.

at the ends of the tube in this alignment, confirms that the magnetization at the ends is perpendicular to $\hat{n}$. In Fig. 3.10(a) we obtain a strong contrast in the signal only at the ends of the tubes in the shadow and not directly in the signal of the surface of the NT. This effect could be caused by an oxidation of the NT surface. Since the probing depth causing the surface contrast is limited, but the shadow contrast is related to the magnetization within the sample, we rely in such cases on the I_{XMCD} contrast of the shadow to determine the magnetization configuration.

According to Jamet et al. [139], taking the progressive absorption of the X-ray beam through the sample cross-section into account, a vortex configuration in our NTs should result in XMCD-PEEM contrast for $\hat{k} \perp \hat{n}$ as illustrated in Fig. 3.9. This contrast has a strong surface as well as a strong shadow contrast, having a different sign compared to each other. By making a line cut trough the perpendicular XMCD-PEEM image at the end of the NT, as shown in Fig. 3.10(c), it fulfills the expectations. In Fig. 3.10(d) we show a line cut through the same region but along $\hat{n}$ for the $\hat{k} \parallel \hat{n}$ study. In this case we observe a decrease in the contrast towards the end of the tube, and therefore a reduced magnetization along $\hat{n}$, which is due to the vortex

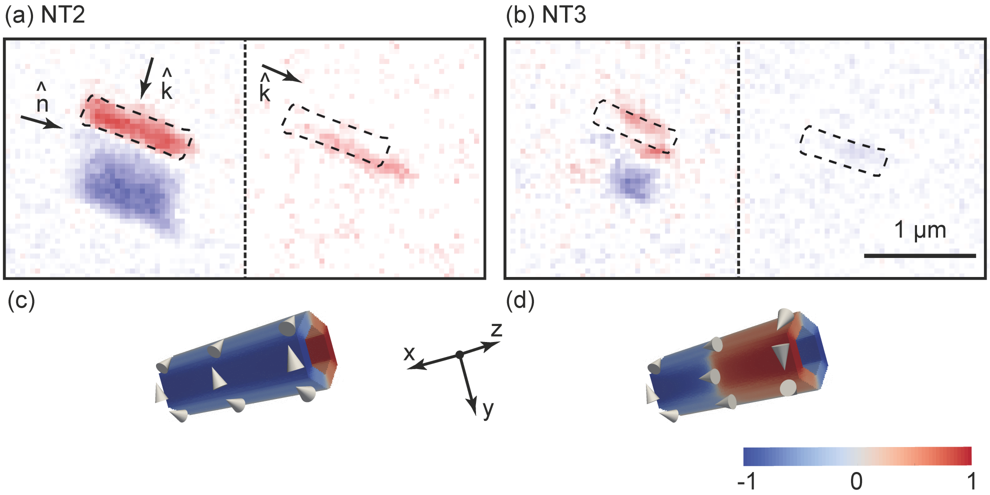

Figure 3.11: XMCD-PEEM images with $\hat{k} \perp \hat{n}$ and $\hat{k} \parallel \hat{n}$ of (a) NT2 found in a global vortex state, and (b) NT3 in an opposing vortex state. The NT of the simulated magnetic equilibrium states has $L = 610$ nm and $d = 245$ nm and shows a vortex state in (c) and an opposing vortex state in (d). The color-scale corresponds to the normalized magnetization in y-direction. The arrow heads indicate the local magnetization direction.

state at the end. Combining the information of the XMCD-PEEM images obtained by $\hat{k} \perp \hat{n}$ and $\hat{k} \parallel \hat{n}$, we obtain strong evidence that NT1 is in a mixed state with an axial alignment in the central part and vortices at the ends. By comparing the two ends of the NT, see Fig. 3.10(a), we find that the vortexes have matching circulation.

Furthermore, we repeated the measurements for two other different sized CoFeB NTs. By comparing as well the two XMCD-PEEM images obtained for $\hat{k} \perp \hat{n}$ and $\hat{k} \parallel \hat{n}$, we receive information on their remnant magnetic configuration. Figure 3.11(a) shows the XMCD-PEEM images for NT2, which is 1.06 μm long. For $\hat{k} \perp \hat{n}$ we see a strong contrast over the entire tube, indicating that nearly all magnetic moments point perpendicular to $\hat{n}$, forming a global vortex state. In the parallel image, in a small area a weak signal of axial components is visible, indicating either a slightly tilted vortex or an imperfection at the surface of the magnetic shell of the tube.

The XMCD-PEEM images of NT3 with $L = 0.83$ μm are shown in Fig. 3.11(b). From these images it seems that NT3 is in an opposing vortex state. We obtain no contrast for the parallel image, indicating that the magnetic moments are all perpendicular to the NT axis and therefore in a vortex state. In the perpendicular image we observe a changing contrast, indicating a state composed of two vortices of opposing circulation separated by a Néel domain wall.

In order to confirm our results, in addition we perform numerical simulations using the software package $mumax^3$ [83]. As described in Sec. 1.7, this package uses the Landau-Lifshitz micromagnetic formalism through a finite-difference discretization. For the simulations we assume a saturation magnetization of $\mu_0 M_s = 1.3$ T, determined by DCM measurements of NTs from the same growth chip [25] and an exchange coupling parameter $A = 2.8 \times 10^{-11}$ J/m [96]. The space in the simulations is discretized to 5 nm and thermal fluctuations are not considered. The simulations confirm that remnant long FM NTs are in a mixed configuration, having an axial central domain and vortices at the ends, as illustrated in Fig. 3.10(e). The short NTs appear in remnant as a global vortex or an opposing vortex state, as shown in Fig. 3.11(c) and (d). However, the circulation direction of the vortices at the ends predicted by the simulations does not match with the results of our measurements. The calculated energy difference between opposing and matching vortices for long NTs in remnant is small compared to the precision of the simulation, therefore both configurations are more or less equally possible. For NTs with a reduced aspect ratio, it results from simulations that the energy difference becomes larger than the thermal energy. As the central region of the axial magnetization disappears with decreasing aspect ratio of the tube, matching circulation of the vortices is eventually favored, resulting in a stable global vortex state.

We have shown that the equilibrium remnant magnetization configuration of FM NTs is programmable, in the sense that longer tubes are in a mixed state, with vortices at the ends and an axial component in between, and shorter NTs are either in a global or an opposing vortex state. Therefore we measured several different sized tubes and additionally also of a second material (permalloy (Py)), see Wyss *et al.* and the corresponding appendix [98], and for the short tubes the distribution of the relative vortex circulation sign as a function of L and d does not follow the numerical predictions. This disagreement of experimental results and numerical simulations could maybe be due to imperfections of the tubes, which favor one configuration over the other. According to the simulations, in fact, the equilibrium circulation direction is influenced by variations of the thickness of the NT and geometrical imperfections. For instance, we know that, due to the FIB milling process, the ends are not perfectly flat, which could play a role in influencing the circulation direction of the vortices. More information, the results of all the measured tubes for CoFeB and Py, and the corresponding simulations can be found in reference [98] and the corresponding appendix.

In conclusion, we imaged the remnant magnetization configuration of FM NTs of various lengths by using XMCD-PEEM. We have shown that short NTs form a stable global vortex state in remnant, which is consistent with the analytical theory of Landeros *et al.* [34] and our own numerical simulations. Since the NTs have been found in both a global vortex state and also in an opposing vortex state, we conclude that the circulation direction of vortices in real NTs is less controllable than expected from simulations and likely sensitive to sample imperfections.

3.4 Conclusion

We have presented in this chapter two different suitable techniques and a variation of one, used for the investigation of CoFeB NTs. The presented results of the different methods are in good agreement with each other and with theoretical predictions. Using RCM measurements we obtained a direct insight in the magnetization of a CoFeB NT. Additionally we confirmed previous theoretical work [34] regarding the aspect-ratio dependence of the magnetic equilibrium state of FM NT by the use of XMCD-PEEM images. These results are in agreement with DCM measurements, confirming that shorter FM NT are more likely to be found in a vortex state and instead longer tubes in a mixed state. Furthermore we have shown that using DCM measurements in combination with numerical simulations we can provide a rather complete picture of the entrance and the exit of individual vortices, and the magnetic reversal processes driven by the vortex nucleation in FM NTs.

3.5 Outlook

In this work we have shown that vortex states in FM NTs are programmable, confirming the theoretical work of Landeros *et al.* [34]. Furthermore we have presented the nucleation and disappearing of individual vortices in CoFeB NTs, indicating the begin and the end of the magnetic reversal process, depending on the sample geometry. There are indications that the magnetic equilibrium state and therefore the magnetic reversal process is strongly influenced by impurities or irregularities of the FM NT. For future applications as components in high-density storage media, the controllability of flux closure states including the circulation direction is important. A reproducible and well defined remnant state is needed for a reliable switching process, which is part of the mechanism used in magnetic storage media, including magnetic read and write heads as elements in hard drives [135].

In order to increase the reproducibility of the switching process, resulting in a global vortex state as the magnetic equilibrium state, a further decrease of the length would be favorable. Additionally the amount of irregularities in the NT would be reduced with decreasing length, thus increasing the probability of a global vortex state. On the other hand, since the defects have an influence on the vortex state, this effect could be used to program a global vortex state. For instance Kläui *et al.* present a method of controlling the vortex formation in magnetic mesoscopic rings [135]. Introducing an asymmetric pinning, they showed the possibility of controlling the circulation direction of a magnetic vortex, which forms in a uniform magnetic field switching from a near-saturated state. A similar effect – a controlled circulation direction of a global vortex state in a FM NT– could maybe be achieved by cutting a trench with the FIB along the length of the NT and creating with this a pinning side.

From the technical point of few, we have shown that DCM is a suitable technique for the investigation of magnetic reversal process of FM NTs, sensitive enough to detect the formation of individual vortices. The applicability to other materials is demonstrated in the chapters 4 and 5. In addition, we have shown that, by integrating RCM measurements, we obtain additional information about M_x and M_z instead of just the net magnetization of the sample. Especially for small samples or samples with a small magnetic moment, RCM could be useful if standard DCM is not anymore sensitive enough. However, RCM is just suitable for a small magnetic field regime. In order to reach a higher sensitivity at higher field, an improved cantilever would be necessary. An increase in the sensitivity of the mechanical oscillator for torque based measurements can be obtained by reducing the size of the resonator, assuming Q can be conserved. This appears from Eq. (1.5) and (1.7). Into consideration has to be taken that the surface oxide gives a strong contribution to the total dissipation and therefore reduces Q of a mechanical oscillator [141]. Accordingly, by reducing t the surface to volume ratio increases whereby surface effects have a stronger influence and Q should reduce. Besides that, due to a reduction of the mechanical oscillator dimension, the read-out becomes more difficult and has to be modified or improved. To overcome this problem it is possible to use a combination of two different mechanical resonators, for instance a nano-sized oscillator attached to a micro-sized oscillator. Due to the coupling of this two asymmetric oscillators, which must have nearly the same resonance frequency, access to the sensitivity of the nanomechanical oscillator is obtained by reading-out the micromechanical oscillator [142–144]. Another option is to use an improved optical detection, including a laser interferometry set-up. Using a special interferometer Ramos *et al.* were able to detect the displacement of a 50-nm wide Si-NW with a precision of 1 $\mathrm{fm/Hz^{1/2}}$ [145].

Furthermore with a few changes in the measurement set-up additional information about the magnetic sample could be obtained. For instance by implementing two radio frequency (RF) compatible loops, generating magnetic fields with perpendicular directions, the transverse RF components of precessing magnetization can be read-out [146]. This torque-mixing magnetic resonance spectroscopy allows the simultaneous read-out of spin resonance and net magnetic moment.

4 Stabilized Skyrmion Phase in MnSi Nanowires detected by Dynamic Cantilever Magnetometry

As shown in the previous chapter, DCM is a non-invasive technique compatible for the study of nanometer-scale magnetic samples. For instance, it contributes to a better understanding of the reversal process in FM NTs. Besides FM samples, it is also useful for studying more complex magnetic systems, as shown in the following. In this chapter we show that DCM is a suitable technique for the investigation of skyrmion-containing samples. We observe a stabilized skyrmion lattice phase, extending from around 29 K down to at least 0.4 K in single MnSi NWs. Although other experiments on two-dimensional thin films show that reduced dimensionality stabilizes the skyrmion phase (see Sec. 2.3), our results are surprising, given that the NW dimensions are much larger than the skyrmion lattice constant. Furthermore, the stability of the phase depends on the orientation of the NWs with respect to the applied magnetic field, suggesting that an effective magnetic anisotropy – likely due to the large surface-to-volume ratio of these nanostructures – is responsible for the stabilization.

The results presented in this chapter are adapted from the following publication:

Stabilized Skyrmion Phase in MnSi Nanowires detected by Dynamic Cantilever Magnetometry
A. Mehlin, F. Xue, D. Liang, F. Du, M.J. Stolt, S. Jin, M.L.Tian, and M. Poggio;
Nano Lett. **15**, 4830 - 4844 (2015) [24]

4.1 Introduction

Magnetic skyrmions are topologically nontrivial spin configurations that appear for example in B20 crystals with a helical ground state and arise due to DMI [111, 147, 148]. A detailed description about skyrmions containing materials and under which conditions they appear, is given in chapter 2. Since their initial observation in 2009 [11–13], they have been considered promising carriers of information in high density magnetic media due to a number of favorable properties, including their stability, nanometer-scale size, and the ultra-low electrical current density required to move them [14]. The threshold for moving these vortex-like spin configurations is only around 10^6 A/m^2, compared to the 10^{12} A/m^2 required to move a domain wall [15, 16], allowing potential skyrmion-based memory devices to count on negligible ohmic heating. Nevertheless, since the skyrmion phase in bulk helimagnets is confined to a small region of temperature and magnetic field, the possibility for applications remains limited.

Recently, however, reduction of sample dimensions from bulk to two-dimensional (2D) thin films has been shown to expand this phase [18, 124, 125, 149, 150], either because of spatial confinement [122] or uniaxial distortion effects [123]. In this study, we use DCM [32] to investigate a natural follow-up question: what is the extent of the skyrmion phase in magnetic nanowires (NWs)? Interest in these magnetic nanostructures, aside from the increased degree of confinement that they provide compared to thin films, is driven by their obvious potential for encoding information in high densities and for transmitting information from one location to another. NWs play a prominent role in a non-volatile magnetic memory proposals such as the so-called “racetrack” design based on the motion of magnetic domain walls [8]. Furthermore, they are preferable to bulk material due to the reduced presence of stacking faults in their crystalline structure.

While a measurement of NW magnetization would directly probe the skyrmion phase transition, conventional techniques such as SQUID magnetometry are not sensitive enough to measure the magnetic moment of a single NW. Measurements of ensembles are complicated by the random orientation, varying size of the NWs [20] and the interactions between neighboring NWs, as well as by the presence of polycrystalline films and other morphologies of MnSi on the Si growth substrate.

DCM, on the other hand, is an ideal method for investigating the magnetization of individual nanostructures in defined magnetic field orientations [21–23]. Here we use this sensitive technique to measure the extent of the skyrmion lattice phase in individual MnSi NWs. By mounting a single MnSi NW on the end of an ultrasensitive Si cantilever and measuring shifts in the cantilever's resonant frequency as a function of temperature, applied magnetic field, and orientation, we determine the nanostructure's magnetic phase diagram. These shifts result from the magnetic torque produced by the NW's net magnetization **M** and an externally applied magnetic field **H**. Measurements are performed with the long axis of the MnSi NWs oriented either parallel or perpendicular to the applied field, as illustrated in Figs. 4.4 and 4.11. Crucially, our non-invasive technique does not require thinning the sample to a 2D slab as in Lorentz transmission electron microscopy (LTEM) or making electrical contacts as in magnetoresistance or topological Hall effect (THE) measurements.

As a result of the different mechanism compared to previously used techniques, DCM can provide both complimentary and – as in this case – new information about skyrmion phases in nanostructures. In particular, we find strong evidence for a skyrmion lattice phase stabilized depending on the applied magnetic field orientation. This stabilization occurs despite of the fact that the dimensions of the NW are too large to confine the skyrmion lattice. There is, however, an important difference between these NWs and bulk single-crystal MnSi samples: the NWs have an especially large surface-to-volume ratio for surfaces perpendicular to the long axis. For this reason, we hypothesize that an effective uniaxial anisotropy – likely due to the demagnetization influence of the surfaces – suppresses the alternative conical phase and favors the skyrmion configuration [84, 151].

4.2 Sample and Experimental Setup

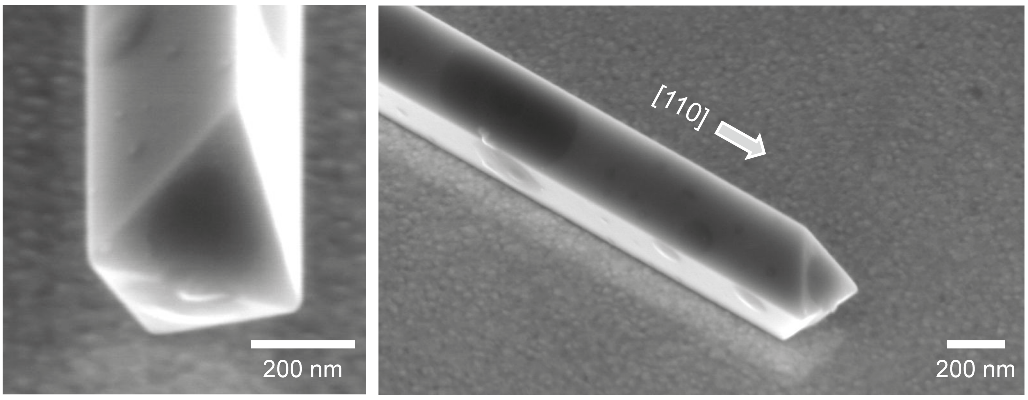

Figure 4.1: Scanning electron micrograph of one of the used single-crystalline MnSi NWs, from the front and from the side. The NW has [110] growth direction [152] and is placed on a gold surface. All surfaces are $\{111\}$.

For our study of the stability of the skyrmion lattice phase depending on the orientation of the applied magnetic field, we use single-crystal MnSi NWs. The wires are grown by chemical vapor deposition (CVD) [152] and were previously

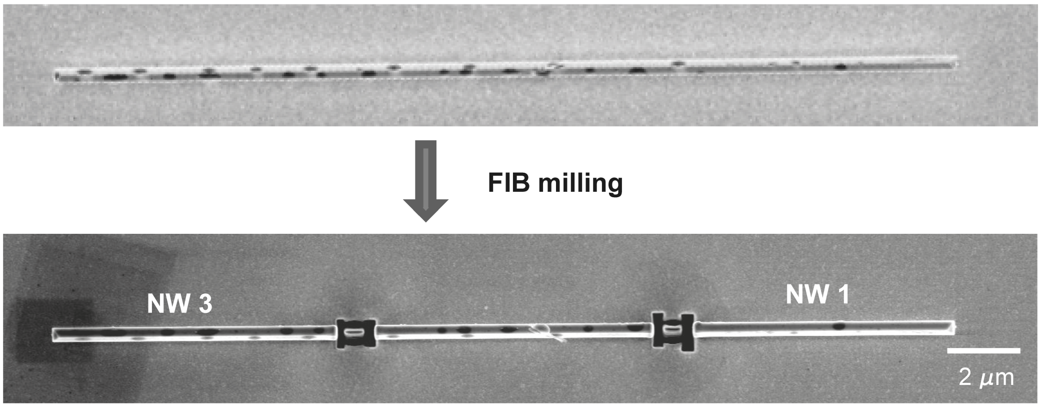

Figure 4.2: SEM of the used single-crystalline MnSi NW, before (up) and after (down) an FIB milling process. NW1 and NW3 are segments of the same MnSi NW. The labeled pieces are used in the measurements, details about the segments are given in Tab. 4.1.

studied in a thinned-down form by LTEM [126]. In parallel to this work, these NWs were analyzed through magnetoresistance measurements [52, 127], followed by THE studies [128]. The MnSi NWs are grown along $\langle 110 \rangle$ and have smooth $\{111\}$ surfaces. Their perfect B20 structure is confirmed by TEM diffraction of identically grown samples [152]. B20 crystal structures belong to the class of non-centrosymmetric crystals, carring Bloch-type skyrmions, as illustrated in Fig. 2.7(a). These kind of skyrmions align with the external magnetic field direction, as previously discussed in Sec. 2.3.

The cross-section of the NWs is a parallelogram with a width of about 470 nm as determined by SEM shown in Fig. 4.1. This cross-section is split by a merohedral twinning plane, specifically the (001) plane parallel to the $\langle 110 \rangle$ growth direction, which divides the NW into two parts with an opposite handedness. Such twinning is expected for B20 silicide NWs and was previously observed in FeSi NWs [153].

We prepared for our studies three different samples. To do that, we placed the MnSi NWs on a gold surface, by using precision micromanipulators under an optical microscope. Afterwards, we imaged them in an SEM, determining length and diameter. We split one NW under a milling process with a Focused Ion Beam (FIB) into three parts, as shown in Fig. 4.2. The FIB milling was made, in order to have availability of more than one sample from the same wire. In the last step of the sample fabrication, we attached three different NWs separately to ultrasensitive Si cantilevers with epoxy (Gatan G1) using precision micromanipulators. The used single-crystal Si cantilevers are 180 μm-long, 4 μm-wide, and 0.1 μm-thick with a 18 μm-long, and 1 μm-thick mass at the tip. Next to the mass-loaded tip is a 12 μm-wide paddle, which serves as a reflective surface in a fiber interferometer used for the detection of the cantilever motion [71], more details about the read-out

	Nanowires		
	NW1	NW2	NW3
Configuration with respect to the field	Parallel	Parallel	Perpendicular
MnSi Nanowires			
Length [μm]	7.1	26.7	7.8
Volume [μm^3]	1.06	4.11	1.16
Demagnetization field [T]	0.0049 $\pm$ 0.0002	0.0014 $\pm$ 0.0001	0.0976 $\pm$ 0.0117
Si Cantilever			
Length l [μm]	180.0	180.0	180.0
Effective Length l_e [μm]	125.9	125.9	125.9
Resonant Frequency f_0 [Hz]	2062.8	2025.9	2106.3
Spring Constant k_0 [μN/m]	37 $\pm$ 5	50 $\pm$ 10	44 $\pm$ 10
Q-Factor Q_0 at T =4 K	4.1x10^4	4.0x10^4	4.2x10^4

Table 4.1: Properties of the MnSi wires and Si cantilevers for each measured configuration.

are given later on in this section and in Sec. 1.2.2. Mechanical properties of the used cantilevers and FEM simulations are described in Sec. 1.2.1.

Short pieces of 7.1 μm (NW1) and 7.8 μm (NW3), which originated from the same NW, and a 26.7 μm (NW2) non-FIB treated NW were attached to the end of three different ultra-soft Si cantilevers. NW1 and NW2 were attached with the long axis of the wire parallel to the long axis to the cantilever (Fig. 4.3). Instead, NW3 was attached with the long axis perpendicular to the cantilever's long axis. Details about the used NWs and the corresponding cantilevers are listed in Tab. 4.1.

Cantilever magnetometry measurements are performed in a vibration-isolated ^{3}He cryostat. We mount the cantilever on a sample stage which is hanging from springs for additional vibration isolation. Such a stage is contained in a vacuum chamber with a pressure below 10^{-6} mbar and positioned at the bottom of the cryostat, (sample mount and the cryostat are shown in Fig. B.1). An external magnetic field along the cantilever axis up to $|H| = 6$ T can be applied with a superconducting magnet. For the detection of the cantilever's motion, an optical-fiber interferometer is implemented. The laser light from a temperature-tunable laser diode with a wavelength of 1550-nm, operated with a power of 100 nW, is focused on the paddle of the cantilever.

The quality factors of the Si cantilevers are 4×10^4 at $T = 4$ K and are determined by the ring-down method. The fundamental mechanical

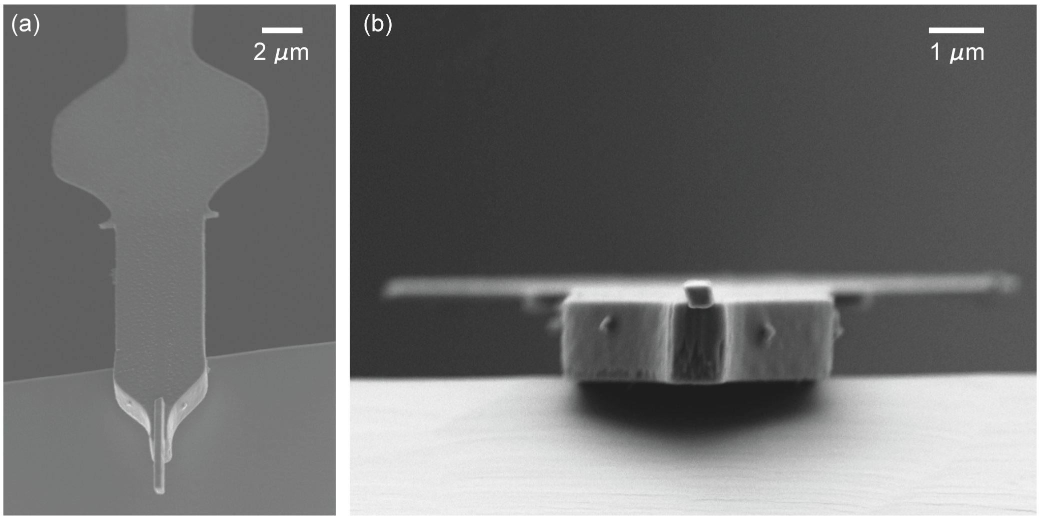

Figure 4.3: SEMs of NW1 attached to the tip of the Si cantilever, from the top (a) and the front (b).

resonance frequencies of the cantilevers are between $f_0 = 2.0$ kHz and 2.1 kHz and their spring constants are between $k_0 = 30$ μN/m and 50 μN/m, as determined from measurements of thermal motion at various temperatures (see Tab. 4.1 for the precise cantilever properties). During the measurements, the interferometric cantilever deflection signal is fed through an FPGA circuit back to a piezoelectric element which is mechanically coupled to the cantilever. In this way, we are able to self-oscillate the cantilever at its resonance frequency and at a desired amplitude $x_{rms} \simeq 10$ nm, for which $\theta_c \ll 1°$. The self-oscillation allows fast and accurate measurement of the cantilever's resonance frequency.

More details about the working principle of the implemented optical-fiber interferometer are given in section 1.2.2. Technique-related information are given in Chap. 1. A detailed description of the used setup and the handling is given in the appendix B. In the following, we present and discuss the results of NW1 and NW3 in Sec. 4.3, and in Sec. 4.4 for NW2.

4.3 Magnetic Field Parallel to the long Axis of the MnSi Nanowire

In this section we present the measurements performed with NW1 and NW2. These two NWs were attached to the cantilever with their long axis parallel to the long axis of the cantilever, as illustrated in Fig. 4.4. In this configuration, **H** is parallel to the long axis of the NW. In most magnetometry measurements, we bring the system to a constant temperature T and apply a large external

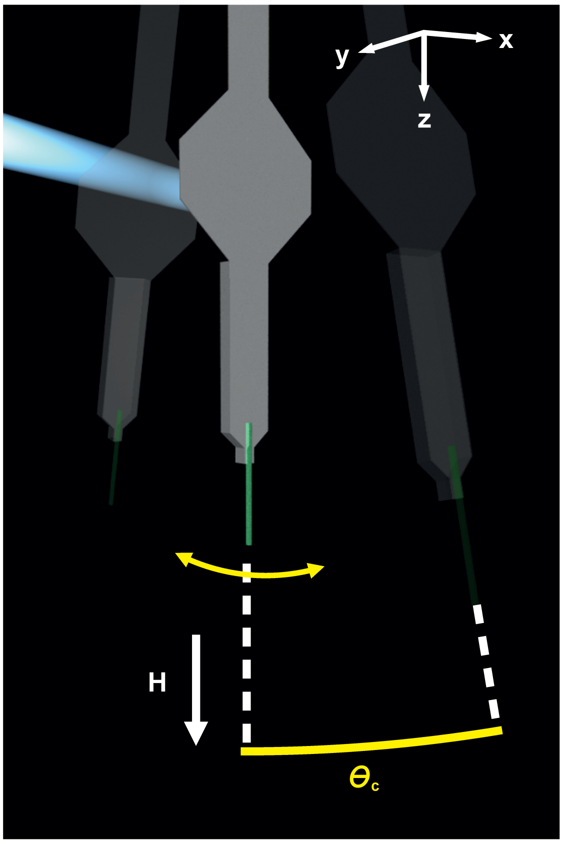

Figure 4.4: Schematic of the experimental setup. A MnSi NW (green) is attached to the end of a Si cantilever (grey), whose long axis is parallel to the applied magnetic field **H**. The cantilever oscillates in x-direction. The laser light from the fiber interferometer is shown in white.

field, $H = 1$ T, in order to magnetize the NW and initialize it in its field-induced ferromagnetic phase. We then sweep the magnetic field to 0 T, and while sweeping down, we detect the cantilever's frequency.

As shown in chapter 1, we can describe the energy of our NW-on-cantilever system by the sum of a mechanical energy term, related to the cantilever (approximated here as a simple harmonic oscillator), and a magnetic energy term, related to the attached sample (1.12). From such consideration, we have derived a generally valid equation describing the change in the resonance frequency due to the magnetic energy E_m, recalling (1.27):

$$\Delta f = \frac{f_0}{2k_0 l_e^2}\left(\left.\frac{\partial^2 E_m}{\partial \theta_c^2}\right|_{\theta_c=0}\right), \tag{4.1}$$

where $\left.\frac{\partial^2 E_m}{\partial \theta_c^2}\right|_{\theta_c=0}$ is the second derivative of the magnetic energy with respect to θ_c at the cantilever's equilibrium angle. Therefore, measurements of Δf

reveal the curvature of the magnetic energy with respect to the sample angle. Such information sheds light on the magnetic anisotropy of the sample and, under certain conditions, on the magnitude and direction of the sample's integrated magnetization **M**. By focusing on the sample's average magnetic response, we can then deduce the type of magnetic configuration and therefore its spatial dependence.

In order to relate the measured Δf, described by equation (4.1), to **M**, we derive in the next section an expression for **M**.

4.3.1 Inferring the Magnetization from the Measured Frequency Shift for M||H

Here we consider just the case of our NW-on-cantilever experiment in which **H** is parallel to the long-axis of the NW. Since our measurements respond to the samples's average magnetization **M**, we can – for the moment – ignore the spatial modulation of the magnetization within the sample and write an effective magnetic energy as if the NW were a single-domain particle. This treatment allows us to infer the behavior of the average magnetization as a function of the measured frequency shift Δf. Given the NW's high aspect ratio, this effective energy is dominated by a uniaxial shape-induced anisotropy. The magnetic energy of the system can then be expressed as:

$$E_m = -\mu_0 \mathbf{H} \cdot \mathbf{M} V + \frac{\mu_0 V}{2} \left[(\mathbf{M} \cdot \hat{n})^2 D_{\parallel} + (\mathbf{M} \times \hat{n})^2 D_{\perp} \right], \tag{4.2}$$

where μ_0 is the permeability of free space, $\hat{n}$ is the unit vector along the cantilever's long axis (in this experiment $\hat{n} \parallel \mathbf{H}$), V is the volume of the magnetic material, and $D_{\parallel}$ ($D_{\perp}$) is the demagnetization factor along (perpendicular to) $\hat{n}$. Since the long-axis of the NW is aligned along $\hat{n}$, we have $D_{\perp} > D_{\parallel}$. Given these circumstances and a magnetization **M** whose characteristic dynamics occur on time-scales much faster than $\frac{1}{f_0} \approx 500\mu s$, **H** will set the polarization axis for the average magnetization **M**, and $|\mathbf{M}|$ will tend to increase with increasing $|\mathbf{H}|$. Therefore, rewriting (4.2) in terms of θ_c with $\mathbf{M} \parallel \mathbf{H}$, we have:

$$E_m = -\mu_0 H M V + \frac{\mu_0 M^2 V}{2} \left[D_{\parallel} \cos^2\theta_c + D_{\perp} \sin^2\theta_c \right]. \tag{4.3}$$

Taking the second derivative of this equation with respect to θ_c we find:

$$\frac{\partial^2 E_m}{\partial \theta_c^2} = \mu_0 M^2 V (D_{\perp} - D_{\parallel})[\cos^2\theta_c - \sin^2\theta_c]. \tag{4.4}$$

Since $\theta_c \ll 1°$, we obtain the following result:

$$\left. \frac{\partial^2 E_m}{\partial \theta_c^2} \right|_{\theta_c = 0} = \mu_0 M^2 V (D_{\perp} - D_{\parallel}). \tag{4.5}$$

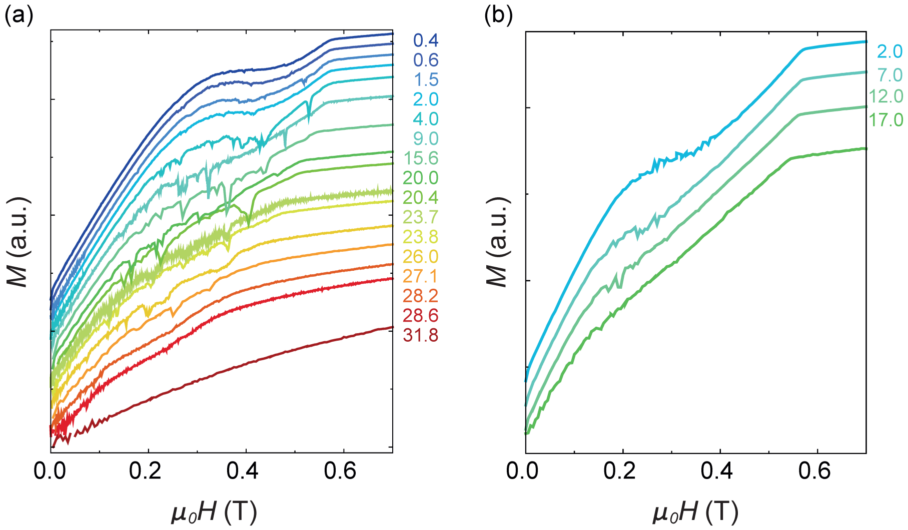

Figure 4.5: Dependence of the magnetization on an applied magnetic field with the NW parallel to the field. M(H) for (a) NW1 and (b) NW2 measured at different temperatures (labeled on the right). For clarity, M(H) at different T have been vertically shifted with respect to each other by a constant value.

Applying (4.1), we can then write,

$$\Delta f = \frac{\mu_0 M^2 V f_0}{2k_0 l_e^2}(D_\perp - D_\parallel). \tag{4.6}$$

Solving for M in terms of Δf, we arrive at:

$$M = l_e \sqrt{\frac{2\Delta f k_0}{f_0 \mu_0 V (D_\perp - D_\parallel)}}. \tag{4.7}$$

Note that the net magnetization M is the integral of the spatially varying magnetization over the entire sample, whose volume V is determined by measuring the NW dimensions by SEM. The demagnetization factors are calculated according to A. Aharoni [154], making the approximation of a rectangular cross-section. Using these, measuring Δf and applying (4.7), we are able to plot M as a function of H for various temperatures, for NW1 in Fig. 4.5(a), and for NW2 in Fig. 4.5(b).

In Fig. 4.6 we show M(H) for NW1 at a temperature of 9 K, up to a field of 6 T. Δf was collected by starting the measurement at 6 T and sweeping the field down to zero. Note that the field-polarized FM state remains unsaturated even at $H = 6$ T (also at $T = 1.5$ K), as expected, and approaches a saturation magnetization within the measurement error for what is reported in bulk (0.39 μ_B/Mn) and thin films (0.42 μ_B/Mn, i.e. per Mn atom) of MnSi [155].

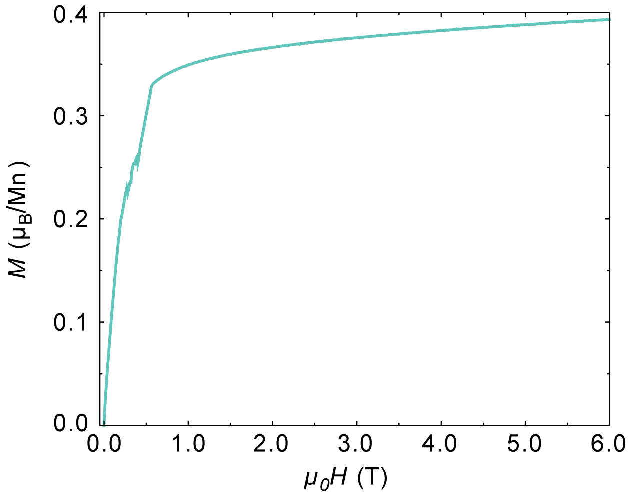

Figure 4.6: Behavior of the magnetization at high field. M(H) calculated from the measurements of Δf(H) for NW1 at T = 9K, with the long axis parallel to the field. The field-polarized ferromagnetic state remains unsaturated even at H = 6T. It approaches a saturation magnetization close to what is reported for MnSi in bulk (0.39 μ_B/Mn) and thin films (0.42 μ_B/Mn).

Having access to M (H), gives us the possibility to assign different phase transitions, as described in the next section.

4.3.2 Determination of Phase Transitions

For the moment we focus on the measurements performed with the 7.1 μm-long MnSi NW, with the long axis parallel to the applied magnetic field, NW1. In order to determine the magnetic phase transitions, we first take note of the region in H and T showing sharp discontinuous dips in M(H). The sharp dips in M(H) in Fig. 4.5 are fully reproducible and robust to changes in the direction and sweep rate of the applied magnetic field. For the moment we hypothesize that this behavior may be the signature of a mixture of skyrmion and conical or helical states. We therefore label this region in the phase diagrams shown in figure 4.8 as the "skyrmion mixed phase". We discuss the possible physical mechanisms producing this features at a later stage of the data presentation, in Sec. 4.4.

M(H) is also characterized by a tilted plateau region, identified as a skyrmion lattice phase by Bauer and Pfleiderer [119], see Fig. 4.7 (a more detailed description is given in Sec. 2.3.1). By fitting M(H) and calculating $\partial M/\partial H$, we assign the transitions between the conical, skyrmion lattice, and ferromagnetic phases of the magnetic NW, following procedures similar to those described by Bauer and Pfleiderer [119] as shown in Fig. 4.7. For fitting M(H), we first remove the sharp dips associated with the mixed phase, then

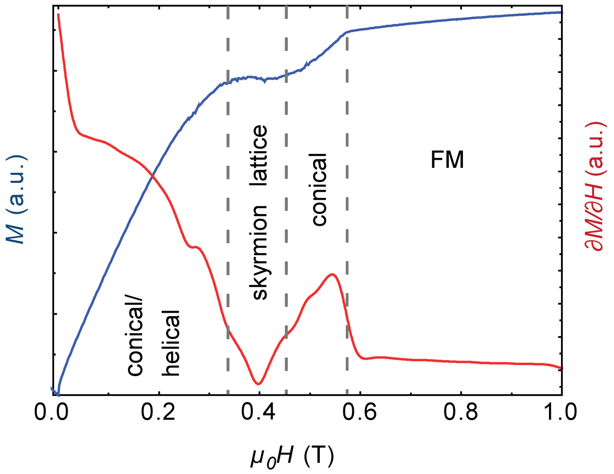

Figure 4.7: An example of M(H) (blue) and the corresponding $\partial M/\partial H$ (red) used for determining magnetic phase transitions, here shown for NW1 at $T = 0.6$K (red).

fit the remaining M(H) curve to a piecewise cubic spline. From this fit we calculate $\partial M/\partial H$, which reveals the overall behavior of the magnetization. Next, moving from high field to low field, we identify the transition from FM to conical phase as the first point of inflection in $\partial M/\partial H$, e.g. around $H = 0.57$ T in figure 4.7. Below this transition, the width of the dip in $\partial M/\partial H$ delineates the size of the skyrmion lattice phase. To quantify this width, we take the full-width at half-maximum (FWHM) as shown by the dotted lines in figure 4.7.

We follow the procedure described above for the different measurements between 0.4 K and 31.8 K shown in Fig. 4.5(a), and obtain the phase diagram shown in Fig. 4.8. The skyrmion lattice phase measured for NW1 extends from $T = 28$ K down to at least 0.4 K and stretches between $H \simeq 0.2$ T and 0.5 T. This region is significantly larger than the small pocket near the critical temperature observed in bulk MnSi (from $T = 26$ K to 28.5 K and $H = 0.1$ T to 0.25 T) [11, 119] and confirms the less direct magnetoresistance observations of Du et al. [52] and Liang et al. [128] in the same field geometry. Note that comparison between field-cooled (FC) and zero-field-cooled (ZFC) measurements also allows us to distinguish the transition between the helical and the conical phase, details about this are given in the next section.

In order to confirm the extended skyrmion phase, we performed the second set of measurements, with NW2. NW2, which is also mounted with its long axis parallel to **H**, is a 26.7-μm-long NW with similar cross-sectional dimensions and grown on the same wafer as NW1, for precise dimensions and properties of the used cantilever see Tab. 4.1. Measurements of the M(H) for NW2 show an extended skyrmion lattice phase similar to that measured in the shorter NW1, as well as a region of reproducible dips in Δf(H), as

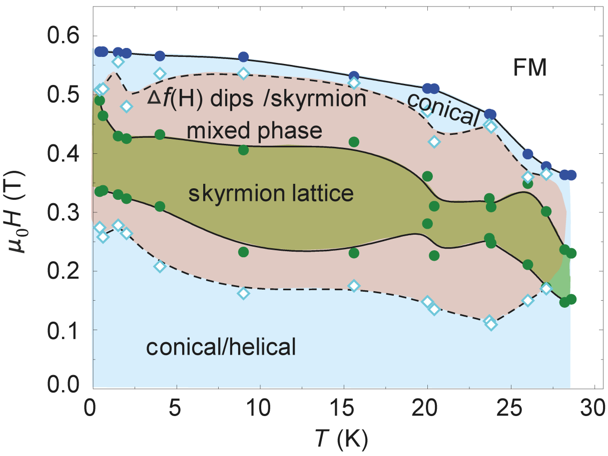

Figure 4.8: Phase diagram for MnSi NW parallel to the field. The magnetic phase diagram shows the boundaries between phases in T and H as determined from measurements of M(H), as shown in Fig. 4.5. Filled circles indicate the boundaries for the 7.1-μm-long NW1. Colored regions of the diagram serve as guides to the eye. The semi-transparent red region denotes the region where the dips in Δf(H) appear. The cyan squares indicate the first and the last dips as a function of H observed in Δf.

visible in Fig. 4.5(b). Remarkable is the clear plateau in the M(H) curve at T = 2 K.

4.3.3 Phase Diagrams Including Helical-to-Conical Transition

In some cases, we cool the NW down through the critical temperature around $T = 28$ K with $H = 0$, i.e. zero-field cooling (ZFC), in order to avoid memory effects from previous magnetic states [119]. We find that ZFC gives different results from our conventional measurement procedure only at low fields ($|H| < 0.1$ T) where hysteresis is observed. We therefore use ZFC in order to distinguish the transition between the helical and the conical phase, which is otherwise obscured by memory effects. In order to assign this transition, we compare the ZFC and the field-cooled (FC) data. Specifically, we compare Δf(H) and assign the transition to the field where the slope ($\partial\Delta f/\partial H$) of the ZFC is equal to the slope of the FC, as shown in figure 4.9. We repeat this procedure for a few temperatures and end up with the phase diagram shown in Fig. 4.10, which includes the helical to conical transition.

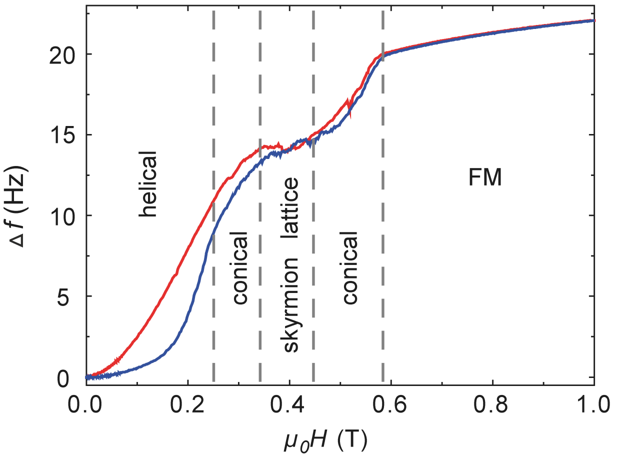

Figure 4.9: Frequency shift as a function of the applied magnetic field for a ZFC (blue) and a FC (red) measurement of NW1 (long axis parallel to the field) at $T = 1.5$ K. The dashed lines mark the transitions between the labeled magnetic phases.

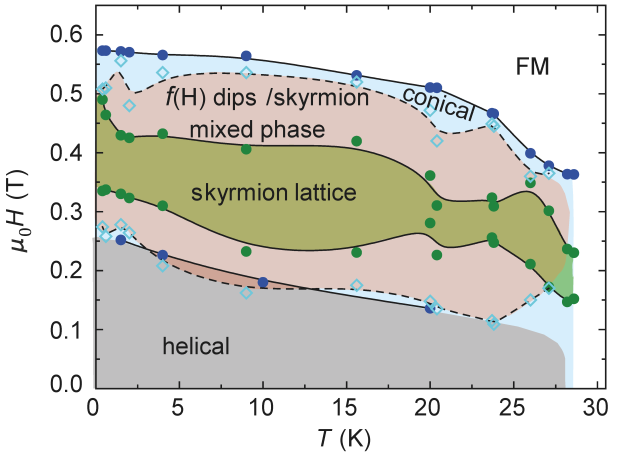

Figure 4.10: Extended skyrmion lattice phase for a MnSi NW parallel to the field (NW1). This phase diagram is identical to that shown in Fig. 4.8, with the addition of the boundary between the helical and conical phase. This boundary is determined through comparison of FC and ZFC measurements.

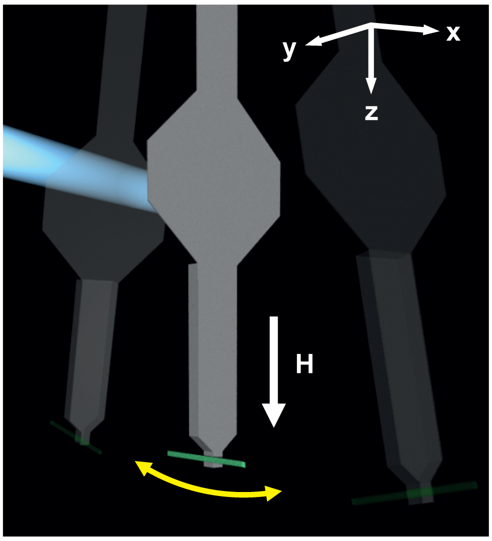

Figure 4.11: Schematic of the experimental setup. A MnSi NW (green) is attached to the end of a Si cantilever (grey), whose long axis is perpendicular to the applied magnetic field **H**. The cantilever oscillates in the x-direction. The laser light from the fiber interferometer is shown in white.

4.4 Magnetic Field Perpendicular to the long Axis of the MnSi Nanowire

In order to complete the research of the skyrmion lattice phase of MnSi in the shape of NWs, we prepared a third sample. For the third set of measurements we attach NW3 to the cantilever such that its long axis is aligned perpendicular to $\mathbf{H}$, as shown in Fig. 4.11. NW3 is a 7.8-μm-long segment of the same longer NW from which NW1 was cut (see Fig. 4.2) and therefore, except for its length, it is identical to NW1 (Tab. 4.1). We plot Δf as a function of H in this configuration in Fig. 4.12(a) for temperatures between 2.0 K and 29.0 K. Here, the shape of Δf differs from the data collected for NW1 and NW2. Because of the strong uniaxial shape anisotropy with the easy axis oriented perpendicular to $\mathbf{H}$, at low applied fields, the anisotropy energy overwhelms the Zeeman energy, forcing $\mathbf{M}$ to point along the long axis of the NW.

The phase transition assignment differs in this case from the parallel configuration, and it is describe in the next section.

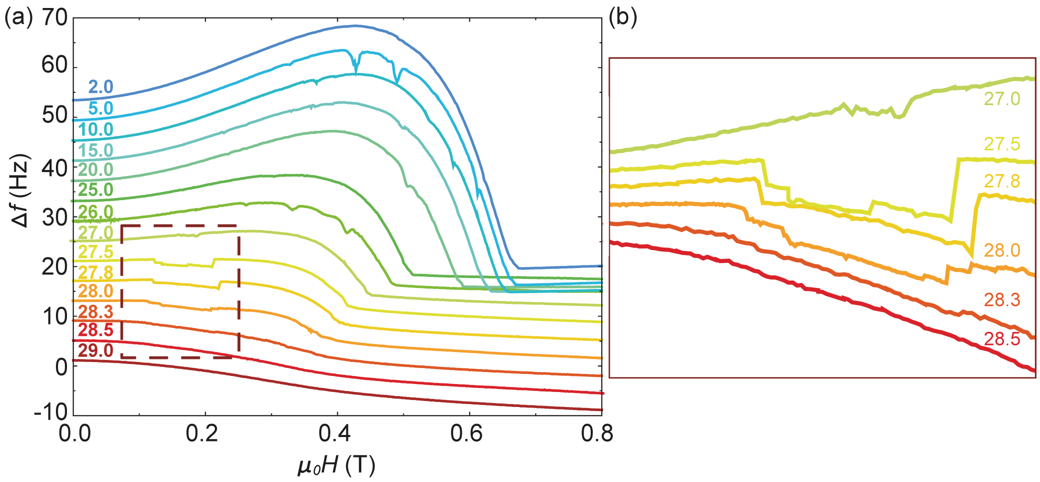

Figure 4.12: Dependence of the frequency shift on the applied magnetic field with the NW perpendicular to the field. (a) Δf(H) for NW3 measured at different temperatures between 2 K and 29 K. For clarity, the Δf(H) at different T have been shifted by a constant frequency. (b) A detailed view of the data near the region of the skyrmion phase marked in (a) by the dashed contour line.

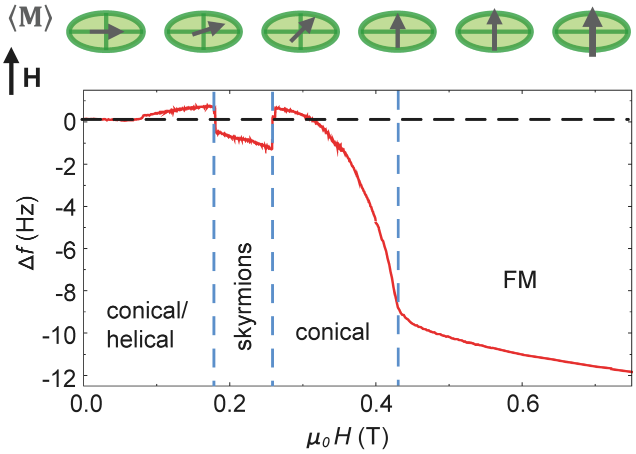

Figure 4.13: Dependence of the frequency shift on magnetic field with the NW perpendicular to the field, for NW3 at $T = 27.5$ K. The dashed blue lines mark the transitions between the labeled magnetic phases. The transitions between conical/helical and skyrmion lattice and between skyrmion lattice and conical phases are determined by the sharp discontinuities in Δf (H). The transition between the conical and field-induced ferromagnetic phase is determined by a sharp change in slope of Δf (H). A sketch of the direction in which the magnetization is pointing is shown above, a detailed description is given in the text.

4.4.1 Determination of Phase Transitions in the Perpendicular Configuration

For measurements of MnSi NWs perpendicular to the applied magnetic field, it is not possible to convert Δf(H) into M(H). Therefore, in order to determine the extent of the various phases, we start by taking note of the region in H and T showing sharp discontinuous dips in Δf (H). These sharp dips appear in a roughly equivalent range of H and T for the perpendicular geometry, e.g. Fig. 4.12(a), as for the parallel geometry, e.g. Figs. 4.5(a) and (b). Once again the features are fully reproducible and robust to changes in the direction and sweep rate of the applied magnetic field. We note that recent transport measurements by Liang *et al.* on MnSi NWs from the same growth batch in the perpendicular magnetic field geometry show a THE signal in a similar range of H and T [128]. We postulate that this region corresponds to a mixture of skyrmion and conical or helical states, similar to that imaged by Yu *et al.* in LTEM measurements of $\mathrm{Fe_{0.5}Co_{0.5}Si}$ [149] under perpendicular magnetic field. Such a phase would have spin chirality and would be expected to produce a THE signal. Note that the features always appear as dips in Δf, i.e. changes in Δf toward more negative values. From equation (4.1) this trend indicates a process resulting in more negative curvatures of E_m with respect to θ_c, corresponding to a reduction in the angular magnetic confinement. The introduction of a magnetic disorder would be consistent with these observations, therefore another possibility is that the features arise from domain wall motion within the NWs. We label this region as the "skyrmion mixed phase", as shown in Fig. 4.14.

Next, to assign the phase transitions, we start with Δf(H) at T = 27.5 K, shown in Fig. 4.13. Let us, for the moment, ignore the field range bounded by discontinuities around $|H| = 0.2$ T. Excluding this range, Δf is positive for $|H| \lesssim 0.3$ T as is, therefore, the curvature of the magnetic energy E_m with respect to the sample angle θ_c. The sign of this curvature indicates that the direction of $\mathbf{M}$ in the sample is close to minimizing the anisotropy energy, i.e. $\mathbf{M}$ points nearly along the magnetic easy axis, here that is the long axis of the NW. As Δf crosses zero and becomes negative (roughly $0.3 < |H| < 0.4$ T), $\mathbf{M}$ points increasingly away from the easy axis and towards the hard axis (short axis of NW) where the anisotropy energy is maximized. This behavior corresponds to $\mathbf{M}$ tilting in the direction of $\mathbf{H}$. The sharp change in the slope of Δf around $|H| = 0.4$ T reflects the coincidence of $\mathbf{M}$ with $\mathbf{H}$ and marks the transition from the conical to the field-polarized ferromagnetic state [23]. The subsequent gradual decrease in Δf to more negative values results from the gradual increase of $\mathbf{M}$ along $\mathbf{H}$ as it approaches saturation. The diagram above Fig. 4.13 schematically shows the progression of the net magnetization $\mathbf{M}$ inferred from Δf(H) in NW3.

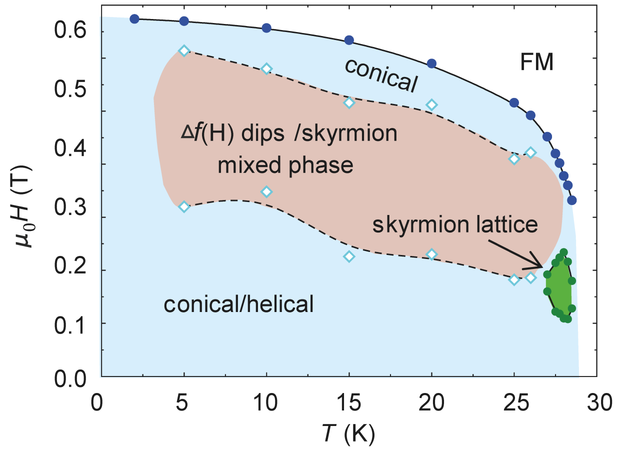

Figure 4.14: Phase diagram for a MnSi NW perpendicular to the field. The magnetic phase diagram shows the boundaries between phases in T and H as determined from measurements of Δf(H), as shown in Fig. 4.12. Filled circles delineate the phases measured for the 7.8-μm-long NW3. Colored regions of the diagram serve as guides to the eye. The semi-transparent red region denotes the region where the sharp dips in Δf (H) appear. The cyan squares indicate the first and last dips as a function of H.

In the next step, we consider the field range bounded by the discontinuities in Δf around $|H| = 0.2$ T. These discontinuities indicate a first order phase transition and delineate a region in T and H similar to that known to correspond to the skyrmion lattice phase in bulk MnSi [11, 119]. This phase is characterized by a reduction in Δf with respect to the neighboring phases. This behavior is consistent with the reduction of M associated with the formation of a skyrmion lattice in a previously conical phase. Measurements of NW3 in this geometry were repeated for temperatures between 2.0 K and 29.0 K, as shown in Fig. 4.12(a). The first order phase transition, indicating the skyrmion lattice phase, appears only in a small T and H region, shown in the zoom-in in Fig. 4.12(b).

By following the interpretation of the data described above, we obtain the phase diagram shown in Fig. 4.14, suggesting a skyrmion lattice phase with an extent similar to that observed in bulk MnSi (see Fig. 2.8) and therefore significantly reduced compared with that observed in NW1 and NW2 with their long axes aligned parallel to **H**. Note that in NW3, the effect of shape-induced magnetic anisotropy appears in the position of the boundary between the conical and field-induced ferromagnetic state, shown in Fig. 4.14. Compared to the phase diagram derived from **H** parallel measurements, shown in Fig. 4.8, the transition fields in Fig. 4.14 are shifted to higher values. The difference can be accounted for by calculating the much larger demagnetization field expected in the perpendicular geometry ($H_d \simeq 0.1$ T) compared with that expected in the parallel geometry ($H_d < 0.005$ T). The values of the

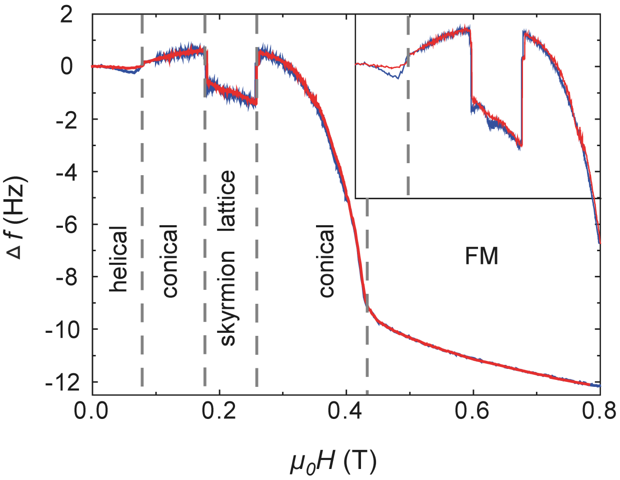

Figure 4.15: Δf(H) of NW3 (long axis perpendicular to the field) at $T = 27.5$ K. The skyrmion lattice phase is bounded by clear discontinuities in Δf (H) as expected for a first order phase transition. By comparing the ZFC (blue) and the FC (red) data we assign the transition between the helical and the conical phase as described for the measurement of NW1, figure 4.9. A zoom-in of the region where the ZFC and the FC data differ is shown in the inset.

demagnetization fields for the three different samples are given in Tab. 4.1.

4.4.2 Phase Diagrams with Helical-to-Conical Transition

Once again, also in this configuration, in order to assign a transition between the conical and helical phases, we compare the ZFC and the FC data. Specifically, we compare Δf and assign the transition to the field where the slope $(\partial \Delta f / \partial H)$ of the ZFC is equal to the slope of the FC, as shown in Fig. 4.15. By doing this for a few data points we obtain Fig. 4.16, which includes the phase transition between helical and conical phases in the phase diagram.

4.5 Discussion and Conclusion

The presented data indicate a stabilization of the skyrmion lattice phase that depends on the orientation of the NWs with respect to the applied magnetic field. Until now, two mechanisms have been proposed to explain experimental observations of skyrmion lattice phase stabilization. The first, based on spatial confinement effects, requires a sample dimension to be comparable or less than the skyrmion lattice constant L_D [122]. Since both the length and cross-sectional dimensions of our NWs are much larger than $L_D = 18$ nm for MnSi, we rule this mechanism out. The second mechanism requires a uniaxial magnetic anisotropy [123]. For example, an easy-axis uniaxial anisotropy, combined with an applied magnetic field aligned parallel to the

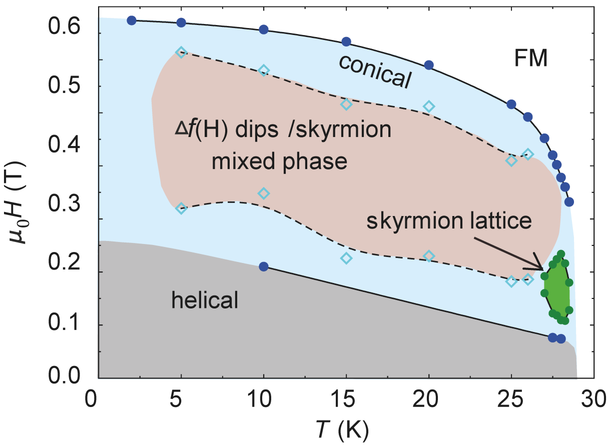

Figure 4.16: Skyrmion lattice phase for a MnSi NW perpendicular to the field (NW3). This phase diagram is identical to that shown in Fig. 4.14, with the addition of the boundary between the helical and the conical phase. This boundary is determined through comparison of the FC and ZPC measurements.

axis, can increase the energy of the conical phase due to its rotating off-axis magnetization components. As a result, the competing skyrmion lattice phase is stabilized. Uniaxial anisotropy can originate from shape, surface, interface, pressure, or crystal direction.

At this point it is instructive to recall that Bauer and Pfleiderer measured millimeter-scale single-crystal MnSi samples as a function of crystal orientation, shape, and field orientation, finding no evidence of skyrmion phase stabilization beyond the conventional bulk case [119]. Magnetocrystalline anisotropy had a small effect on the extent of the skyrmion phase, likely due to its weakness in MnSi [156]. Shape anisotropy also had no stabilization effect, only producing a field shift in the phase diagram due to the demagnetization field. In particular, a $6\times1\times1$-mm^3 sample, whose demagnetization factors are similar to those of our NWs, showed no stabilization effect. The primary difference between these samples and our NWs is the size-scale and the large disparity in the surface-to-volume ratio that results. For long and narrow objects, the surface-to-volume ratio is dominated by surfaces whose normal is perpendicular to the long axis, making the ratio inversely proportional to the diameter. Our samples, with diameters on the order of 470 nm, have surface-to-volume ratios several thousand times larger than the millimeter-scale samples of Bauer and Pfleiderer.

Therefore, we suggest that the demagnetization influence of these surfaces produces an effective magnetic anisotropy [84]. Due to the DMI and missing spins near the boundary [157, 158], spins at the surface align parallel to it. This effective anisotropy could suppresses the conical phase, which combined with a parallel applied magnetic field localizing the skyrmion cores, would stabilize and extend the skyrmion lattice phase [151] and perhaps produce a mixed skyrmion phase. Indications of a mixed skyrmion phase even in the perpendicular geometry may be attributed to the fact that, below the critical field, $\mathbf{M}$ is tilting towards $\mathbf{H}$, and maintains a component along the long axis of the NW. This coincidence of a component of $\mathbf{M}$ with the effective anisotropy axis, could allow some stabilization of the skyrmion phase against the other phases. The stabilizing influence of boundaries on the skyrmion phase is observed in real-space measurements of skyrmion formation in FeGe thin-films, where skyrmions are seen to emerge from the helical phase near the sample edge and grain boundaries [18]. One should also note that the presence of the twinning boundary along the long-axis of the NWs produces an additional anisotropy. The DMI vanishes at this interface, leaving only ferromagnetic exchange. This additional boundary condition prohibits modulation of the magnetization along the twinning plane.

In conclusion, we measure a series of high-aspect-ratio single-crystal MnSi NWs and find strong evidence that their skyrmion phase can be stabilized and extended by an effective magnetic anisotropy. Measurements are made using sensitive dynamic-mode cantilever magnetometry, which allows the investigation of individual nanometer-scale magnetic samples. The finding that an anisotropy – likely arising from the nanometer-scale geometry of the NWs – is enough to stabilize an extended skyrmion phase has important implications. In particular, such a stabilization mechanism would improve the viability of proposals for the use of skyrmions in thin magnetic wires as carriers of high-density information.

4.6 Outlook

A stabilization mechanism of the skyrmion lattice phase due to an effective anisotropy caused by the nanometer-scale geometry of NWs creates broader possibilities for future applications. In terms of high density storage media, as for example the racetrack memory, NWs would provide the needed properties, like the size, robustness, programmability etc. for the realization [8]. Besides the promising shape, NWs have the advantage that the stacking faults or other defects are reduced compared to bulk samples. This is due to the progress which was made in the recent years in the fabrication of these nano-scale objects.

Furthermore, the increased stability of the skyrmion lattice phase due to the nano-scale morphology makes the combination of skyrmions and NWs for applications even more interesting, since skyrmions are promising to be implemented as memory devices. This is due to the property, as mentioned at the beginning of this chapter, that they are stable, have a nanometer-scale size, and the threshold for moving these vortex-like spin configurations is only around 10^6 A/m^2, compared to the 10^{12} A/m^2 required to move a domain wall [15, 16].

So far the disadvantage was that the skyrmion phase in bulk helimagnets is confined to a small region of temperature and magnetic field, and therefore the possibility for applications remains limited. The increased stabilization makes these vortex like structure more robust against external influences and broadens the working conditions, resulting in more possibilities of usage.

Nevertheless, the working conditions of skyrmions in MnSi NWs are not yet really attractive for applications. It is true, that due to the stabilization they become more robust, but still temperatures below 29.5 K are required. On the other hand, the observations which we made, of a stabilized skyrmion lattice in NWs, if the applied magnetic field is parallel to the long axis of the wire, should be valid also for other materials. For instance FeGe would be a promising option. FeGe belongs to the same non-centrosymmetric, B20 crystal class as MnSi, for which reason the behavior is expected to be similar. The crucial advantage of FeGe compared to MnSi is that T_c is around 280 K in bulk [17]. FeGe was already studied in thin-film systems, where a stable skyrmion phase was observed from 280 K down to about 60 K for a film thickness of about 15 nm [18]. These studies show that, if the film thickness is increased to 75 nm, the skyrmion phase is significantly reduced and appears between 250 K to 270 K.

Recently, FeGe in shape of NWs were realized [118]. If our observations of the effective anisotropy stabilizing and extending the skyrmion phase due to the nanometer-scale geometry could be confirmed also in FeGe NWs, this would be a step forward in the direction of skyrmion-containing high density storage media. We have shown the compatibility of our technique with nanometer-scale samples and the required sensitivity. This paves the way for future studies on the effect of confinement and surfaces on magnetic skyrmions. Furthermore, DCM capable of covering the expected temperature range.

5 Néel-type Skyrmions in Multiferroic Lacunar Spinels – Mapping out a Stability Phase Diagram using DCM

In the previous chapter, we demonstrate studying MnSi NWs that DCM is a sensitive technique, suitable to assign phase transition and identify a stabilized skyrmion phase. The focus in this chapter is understanding the role of anisotropy in materials hosting Néel-type skyrmions. We perform DCM measurements on a single-crystal sample of GaV_4S_8: in particular, we compare DCM results with a theoretical model of the magnetic phase diagram as a function of applied magnetic field. By collecting magnetic torque signal for a series of applied field orientations, DCM reveals the magnetization, anisotropy, and magnetic phase diagram of our sample. We observe a skyrmion lattice phase with up to $77.1° \pm 2.3°$ of misalignment between the crystal axis and the applied magnetic field. By comparing our findings with numerical simulations, which describe the stability of the skyrmion lattice in GaV_4S_8, gives us insight into the strength of the uniaxial anisotropy of the system.

The results of this chapter are adapted from the following work:

Néel-type Skyrmions in Multiferroic Lacunar Spinels – Mapping out a Stability Phase Diagram using Dynamic Cantilever Magnetometry
A. Mehlin, B. Gross, I. Kézsmárki, A. Leonov, V. Tsurkan, A. Loidl, and M. Poggio
to be published (2017)

5.1 Introduction

Nontrivial spin structures can occur in non-centrosymmetric crystal compounds, the so called magnetic skyrmions. Starting from their experimental discovery they caught in the recent years increasing attention in condensed matter physics [11]. Magnetic skyrmions arise due to DMI and can occur as individual structures or arranged in a skyrmion lattice and represent a form of magnetic order [159]. In chapter 2 details are given, describing in which material and under which conditions skyrmions occur.

In bulk material until recently mainly Bloch-type skyrmions were investigated. The investigation of Néel-type skyrmions in bulk has become of interest with the discovery of this type of skyrmion lattice in $\mathrm{GaV_4S_8}$, which belongs to the C_{nv} crystal symmetry class [115, 117, 160, 161]. In Néel-type skyrmions, the magnetization rotates in radial direction from the core outwards, see Fig. 2.7(b). Instead in Bloch-type, the magnetic spins rotate perpendicular to the radial direction from the center outwards, as illustrated in Fig. 2.7(a). The relative size of the skyrmion lattice phase of bulk material hosting Néel-skyrmions in the C_{nv} symmetry is bigger than in the case of material carrying Bloch type skyrmions. This is due to the fact that in this type of material the conical phase is not stabilized, while this is the main competing phase of the Bloch-type skyrmion lattice [162]. This additional stabilization seems a promising property of materials carrying Néel-skyrmions and makes them attractive as possible carriers of information in magnetic storage media. Additionally, Néel-skyrmions have a sizable electric polarization, providing the possibility to manipulate them by an electric field [115, 160].

Furthermore, Néel-type skyrmions differ from their Bloch-type counterparts in that their orientation is determined by a uniaxial anisotropy instead of an externally applied magnetic field. This anisotropy is apparent in a strong dependence of the magnetic phase on field orientation. Depending on the strength of the anisotropy the skyrmion lattice phase is more stabilized and therefore occurs for a larger range of the applied magnetic field angle with respect to the direction defined by the anisotropy [162]. More information about Bloch- and Néel-type skyrmions are given in Sec. 2.3.

For the study of the uniaxial anisotropy effect on the stability of the skyrmion phase a single-crystal piece and a suitable technique are required. DCM is an ideal method for investigation of the magnetization of individual structures in various field orientations [23–25]. It is a sensitive and non-invasive technique providing information about the net-magnetization of a sample. Here we use this technique to investigate the stability of the skyrmion lattice phase in $\mathrm{GaV_4S_8}$ depending on the applied field direction which is a measure of the strength of the uniaxial anisotropy. By mounting a single crystal GaV_4S_8 piece at the end of a Si cantilever and measuring its resonance frequency shift for different magnetic field orientations, we determine the corresponding crystals phase diagram. The frequency shift results from the torque generated by the anisotropy in the magnetic energy of the single crystal in combination with a applied magnetic field.

As a result of this investigation, using DCM we provide both complementary as well as new information about the stability of the skyrmion lattice phase in single-crystal GaV_4S_8 samples.

For investigation of the effect of the anisotropy in magnetic crystals carrying Néel-type skyrmions, we use GaV_4S_8. The material is grown by chemical vapor transport, by using iodine as the transport agent. Characterization with X-ray diffraction of a crushed single crystal, which was grown in the same process, showed impurity-free material [115]. GaV_4S_8 belongs to the lacunar spinal family and is a magnetic semiconductor. It undergoes a cubic to rhombohedral transition of the structure at 42 K, driven by a Jahn-Teller distortion, resulting in a stretching of one of the four $\langle 111 \rangle$ crystal axes [115, 117]. The outcome of this transition is a structure containing four different domains in a single-crystal. The magnetic transition occurs in this material at $T_c = 13$ K and therefore the q vector of the cycloidal phase can point in four different directions, as illustrated in Fig. 2.11 (more details about the material are given in Sec. 2.3.2).

GaV_4S_8 was previously studied by magnetic susceptibility and specific heat measurements, investigating the structural and magnetic phase transitions with magnetic field parallel to the $\langle 111 \rangle$ axes [115]. Furthermore, phase transitions depending on the temperature and the applied magnetic field in the three major configurations were investigated by AFM imaging and SANS measurements [117] (the results of those studies are described in Sec. 2.3.2). These studies were followed by magnetic microwave spectroscopy investigations of the spin dynamics in a Néel-type skyrmion lattice and confirmed the previously obtained phase diagrams [161].

5.2 Sample Characteristics

In order to prepare a sample for the DCM measurements, we chose a single-crystal GaV_4S_8 piece, which is shown in Fig. 5.1(a). Shown is the $\{100\}$ surface, which is about $75 \times 75 \mu m^2$. This GaV_4S_8 piece is at the thickest position ~ 43 μm and at the thinness ~ 10 μm thick. These values were determined out of optical pictures. The shown $\{100\}$ surface of the single-crystal was attached with a drop of UV clue to the end of a commercial cantilever under an optical microscope by the use of precision micromanipulators, as shown in Fig. 5.1(b). The used Si cantilever (Nanosensors (TM) TL-Cont) is

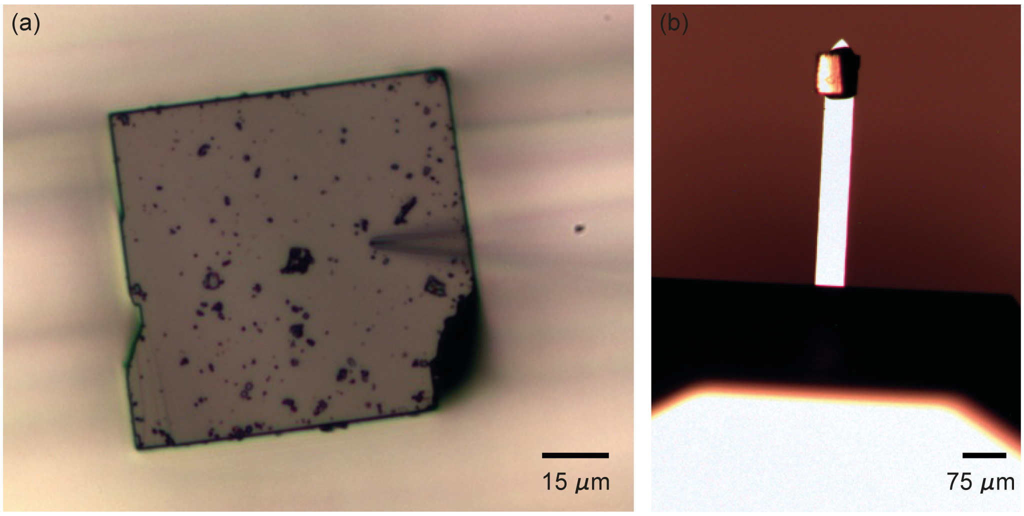

Figure 5.1: Optical pictures showing (a) the $\{100\}$ surface of a single crystal GaV$_4$S$_8$ piece which (b) we attached to the end of a commercial cantilever (Nanosensors (TM) TL-Cont).

made of a 440 μm-long, 50 μm-wide, and 2.3 μm-thick shaft. The shaft ends with a triangle which prolongs the shaft by about 25 μm. The quality factor is about 500´000 and was determined by a ring down measurement at T = 6 K. The fundamental mechanical resonance frequency is $f_0 = 3.25$ kHz and the related spring constant $k_0 \approx 0.3$ N/m.

5.2.1 Cantilever with an Attached Mass

In section 1.2.1.1 we have discussed the properties of bare cantilevers and have shown related numerical simulations by FEM. As mentioned in Sec. 1.2.1.3, the cantilever's properties change if a significant mass is attached. Hence we repeat the numerical simulations, adding a mass with roughly the same dimensions of our sample to the end of the cantilever. For this mass-loaded cantilever the first four resonance modes are shown in Fig. 5.2 (simulations obtained by using the software *Comsol*). By comparing these results with the simulations of the same, bare cantilever, shown in Fig. 1.6, we observe that, in contrast to before, also the n = 1 mode is a torsional mode, not only the n = 3 mode. Furthermore, the numerical calculated frequencies for the first four modes differ significantly. Due to the big additional mass the frequencies shift to smaller values, as expected (see Sec. 1.2.1.3). For instance, the numerical calculated fundamental frequency of the bare lever is $f_0^{bare} = 15.6$ kHz, and of the cantilever with the additional mass is $f_0^{mass} = 4.3$ kHz. The measured value of the cantilever is, as mentioned before, $f_0 = 3.25$ kHz at 6 K.

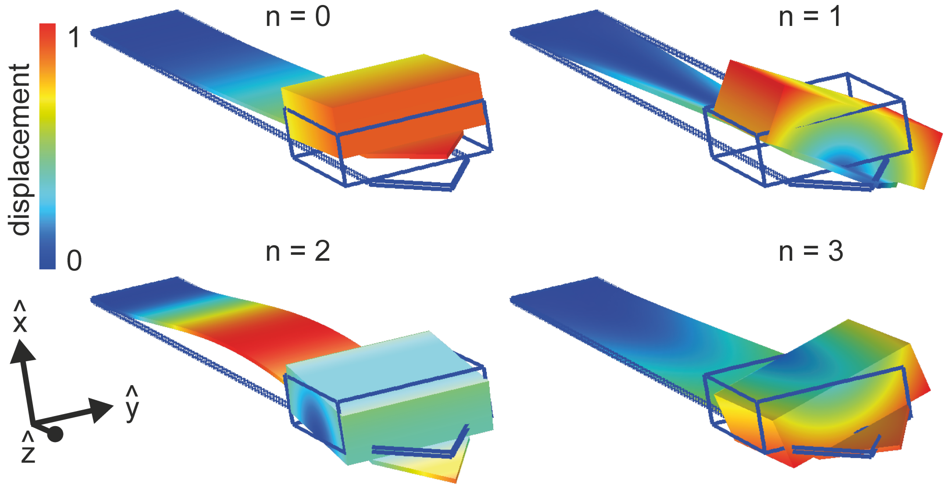

Figure 5.2: The first four modes of the commercial Si cantilever (Nanosensors (TM) TL-Cont) with a big mass attached at the end calculated by FEM. Each mode is separately normalized so that the maximum displacement is 1.

5.3 Experimental Setup

The cantilever magnetometry measurements were performed in a setup composed of two independent closed-cycle cryostats. The cantilever is mounted in a vacuum chamber at the end of a vibration-isolated cryostat in which the temperature can be changed between ∼4 and 300 K. The second cryostat is a rotatable 4.5 T-magnet, with the option of changing the field direction on a plane. The possible field directions with respect to the cantilever are illustrated in Fig. 5.3. In this setup we can change the magnetic field direction in a range of about 120°. During the measurements the cantilever's motion is read-out with an optical-fiber interferometer. Therefore the laser light of a temperature-tunable laser diode is focused on the cantilever where the shaft ends and the triangle starts. The laser diode has a wavelength of 1550 nm and is operated with a power of 100 nW. During the measurements the interferometric deflection signal is fed through an FPGA circuit back to a piezoelectric element, which is mechanically coupled to the cantilever. This provides the possibility to self-oscillate the cantilever at its resonance frequency and at a constant amplitude of $x_{rms} \simeq 30$ nm, for which $\theta_c \ll 1°$. Due to the self-oscillation a faster and more precise read-out of the cantilever's resonance frequency is ensured. Furthermore, we gain access to the dissipation of the combined system of cantilever and magnetic sample, more details are given in the next section. Details about the implemented optical-fiber interferometer are given in section 1.2.2. The used setup and its handling are described in detail in appendix A.

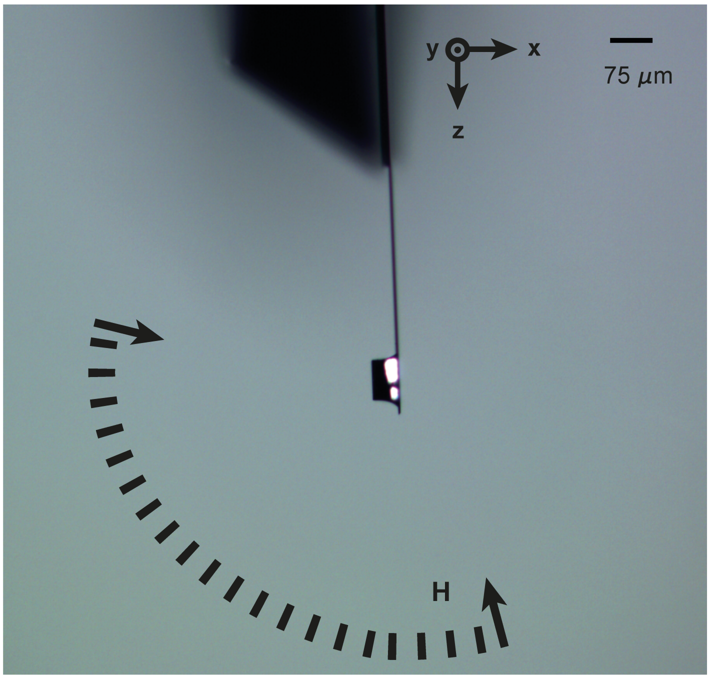

Figure 5.3: Schematic of the possible magnetic field $\mathbf{H}$ directions illustrated on an optical picture showing the cantilever with the attached GaV_4S_8 crystal from a side. The cantilever oscillates during the measurements in the x direction.

5.4 Measurements

Before running the magnetometry measurements presented in this chapter, we bring the system to a constant temperature and apply a large external magnetic field, in order to magnetize the single-crystal and initialize it in its filed-induced FM phase.

5.4.1 Assigning the Phase Transitions

We start in the configuration where the magnetic field is applied parallel to the long axis of the cantilever and therefore parallel to [100] of the magnetic crystal. In this alignment the angle between the four $\langle 111 \rangle$ axes and the field direction is the same for all four, as illustrated in Fig. 5.4, and consequently the phase transitions should occur simultaneously. The response of the frequency as a function of H, at T = 12 K is plotted in Fig. 5.5(a). Since we drive the cantilever at its resonance frequency and keep the amplitude of the oscillation constant we have access to the magnetic dissipation. As demonstrated in Sec. 1.6, according to equation (1.48), the dissipation is peaked as a function of H in occasion of a phase transition. In Fig. 5.5(b), we plot the dissipation

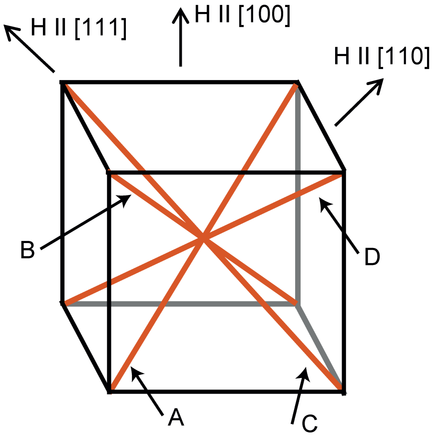

Figure 5.4: Schematic of the crystal structure, in the three crystal directions and the four different body diagonals, the $\langle 111 \rangle$ axes.

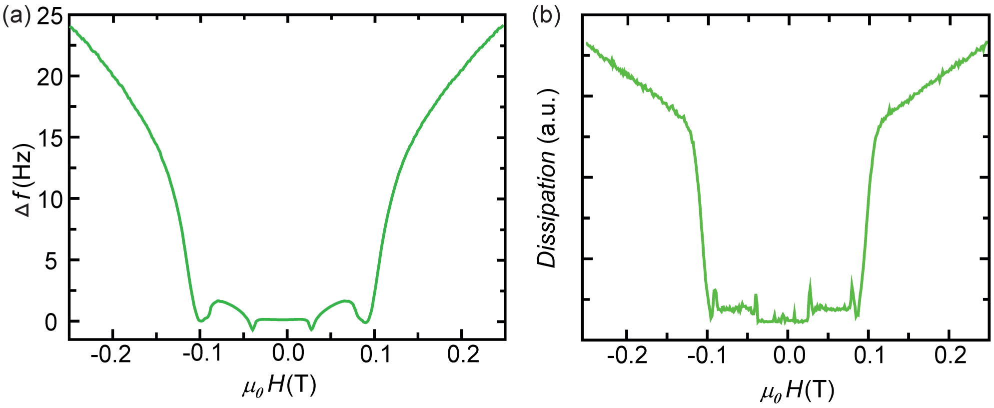

Figure 5.5: (a) Δf (H) at T = 12 K for $\mathbf{H} \,\|[100]$ and (b) the corresponding dissipation. The data were collected by sweeping the field from positive to negative.

as a function of H, which was collected in parallel to Δf (H) shown in (a) when sweeping the magnetic field from positive to negative. Having a closer look, we observe two major peaks for $H > 0$ T and two for $H < 0$ T, roughly symmetric around zero field. These peaks in the dissipation appear at the same field values as the dips in Δf. The peaks (respectively the dips in Δf) for $H > 0$ appear at about 0.03 T and 0.09 T. Comparing these two field values with the results of Kézsmárki *et al.* [117], as shown in Fig. 2.12(c), we find that the field values would fit within the error to the cycloidal to skyrmion phase transition, and to the skyrmion to FM transition at T = 12 K. From this result, that we can use either the dips in Δf or the peaks in the dissipation to assign the phase transition. According to equation (1.27), $\Delta f \propto \partial^2 E_m / \partial \theta_c^2$ reveals changes in the magnetic state.

In order to check the quality and the behavior of our sample, we perform two more tests. First we start changing the temperature and check the response and afterwards we start changing the orientation of the applied magnetic field. The results of these investigations are presented in the following.

5.4.2 Temperature-Dependent Measurements

Since magnetic properties are temperature dependent, we can check the behavior of our single-crystal GaV_4S_8 sample by measuring Δf (H) at different temperatures. In Fig. 5.6 we show Δf in (a) and the corresponding dissipation in (b) for three different temperatures. Data are shown for measurements performed at 7 K and 15 K, in addition to the 12 K already shown before. As previously shown, phase transitions detected at 12 K fit well with previous studies. In comparison, data of the 7-K sweep, indicate a phase transition at around 0.04 T, clearly visible as a peak in the dissipation and as a sudden and significant change in the slope of the frequency. In contrast, at 15 K neither a peak in the dissipation nor any other feature in the frequency shift are visible, hence we do not observe any phase transition at this temperature. Comparing these results with the phase diagram shown in Fig. 2.12(c) we find a good agreement of our data with previous studies.

5.4.3 Angle-Dependent Measurements

Besides temperature dependence, we investigate the angle-dependent behavior of the GaV_4S_8 single-crystal, in order to obtain information about the anisotropy present in this type of magnetic material. Due to the symmetry of the crystal structure, by rotating the magnet by 90° compared to the alignment studied before, $\mathbf{H}$ is again parallel to the [100] crystal orientation. In one case we apply $\mathbf{H}$ parallel to the long axis of the cantilever and in

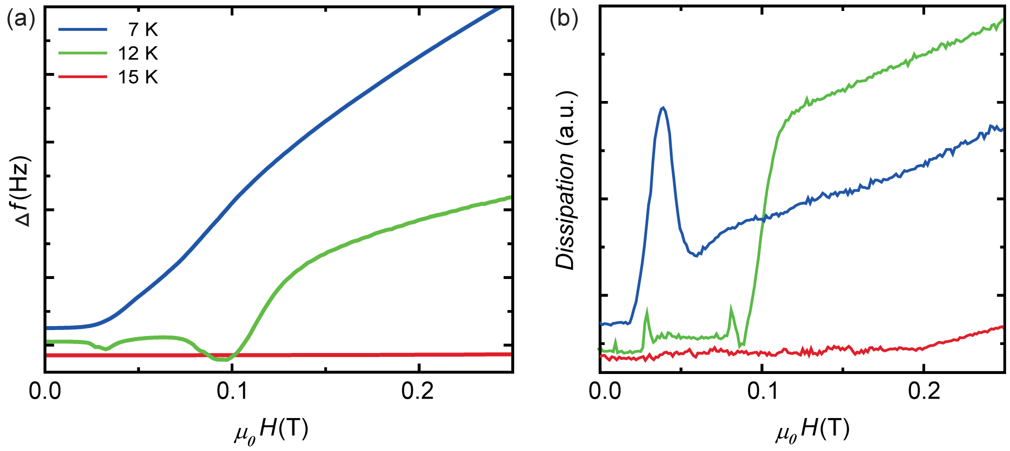

Figure 5.6: For different temperatures, labeled in the legend, (a) Δf (H) and (b) the corresponding dissipation are plotted for H II [100].

the other perpendicular to it, as illustrated in Fig. 5.7(b). Δf (H) in both arrangements have overall a very similar shape, as shown in Fig. 5.7(a). The two curves are slightly shifted with respect to each other in terms of frequency. The same Δf value is reached in both configurations with a separation of about 10 mT. This behavior could be due to the asymmetric shape of the sample, whereby different demagnetization fields for both configurations are expected.

Furthermore, by turning the magnet by 45°, we reach the orientation where $\mathbf{H} \parallel [110]$. From Fig. 5.4, we see that in this configuration the field is coplanar to two body diagonals and perpendicular to the others. Δf (H) at T = 11.0 K in this alignment is plotted in Fig. 5.8(a) and the orientation of the field with respect to the cantilever is sketched in the inset. According to the phase diagram in this configuration, as it is shown in Fig. 2.12(b), in case of a perfect alignment two phase transitions from cycloidal to skyrmion and from the skyrmion lattice to FM are expected at about 30 and 70 mT. However, we observe two dips in Δf between 0.3 and 0.4 T. Considering a small misalignment of the crystal with respect to the applied magnetic field, it is not given that two $\langle 111 \rangle$ axes are perfectly perpendicular to $\mathbf{H}$ and therefore the projection of the field on these axes is non-zero, causing phase transitions to occur at high fields. A misalignment of only 5° from the perfect alignment would result in phase transitions at those high field values. Focusing on the low field (a zoom-in on this region is shown in Fig. 5.8(b)) we observe plateaus in Δf (H). More obviously visible is the change of the slope in the derivative $\partial \Delta f / \partial H$. These features occur at about 32 and 75 mT, which is the region where we expect the phase transition between the cycloidal to the skyrmion phase and from the skyrmion phase to the FM state to take

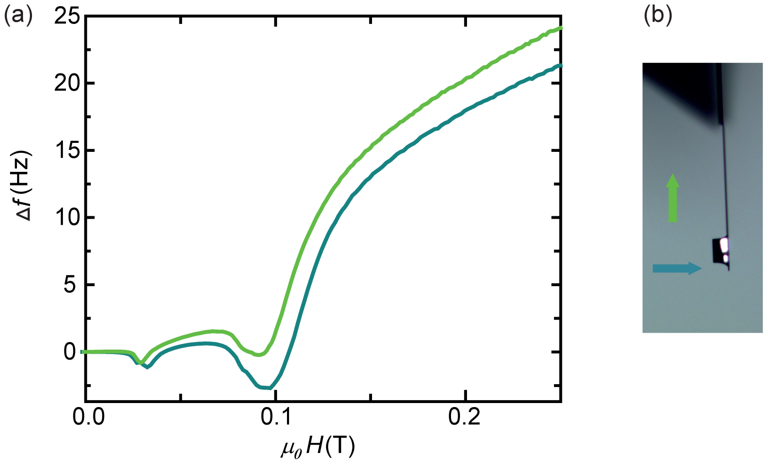

Figure 5.7: (a) Probing Δf (H) for $\mathbf{H}$ II [100] from two different magnetic field orientations at T = 12 K. (b) Illustration of the two different magnetic field directions, indicated by the two colored arrows.

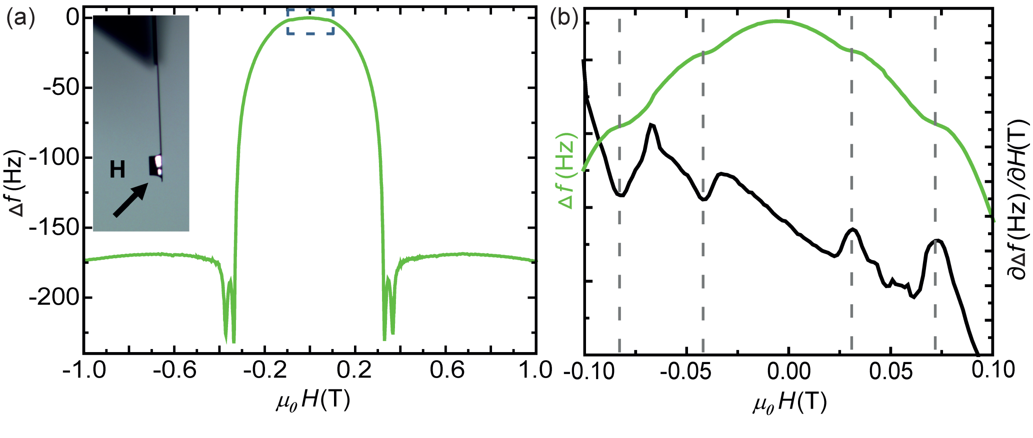

Figure 5.8: (a) Δf(H) for $\mathbf{H}$ II [110] at T = 11 K. (b) A zoom-in on the low-field region, marked in (a) by the dashed contour line. Δf(H) is plotted in green and the corresponding derivative $\partial \Delta f / \partial H$ in black. The phase transitions are indicated by the dashed lines.

place in this configuration.

Comparing Δf for $\mathbf{H} \parallel [100]$ (Fig. 5.5(a)) with the alignment of $\mathbf{H} \parallel [110]$ (Fig. 5.8(a)) we observe that the overall shape differs significantly. The behavior of the frequency shift is strongly influenced by the anisotropy, which can have different origin, as discussed in Sec. 2.1.4. Since the difference in $\Delta f(\mathrm{H})$ is small between $\mathbf{H} \parallel [100]$ probed in two unequal orientations, as shown in Fig. 5.7, we can rule out that the main influence on the anisotropy is due to the shape. Furthermore surface induced anisotropy should have a negligible effect for such a big single-crystal piece, therefore the difference of the overall shape of $\Delta f(\mathrm{H})$ in the different configurations seems to be caused by the intrinsic crystal anisotropy. The sample behaves as having a hard plane for the $\mathbf{H} \parallel [110]$ orientation and an easy plane in the $\mathbf{H} \parallel [100]$ alignment. Having a closer look to the data collected in the $\mathbf{H} \parallel [110]$ configuration plotted in Fig. 5.8, we see that the dips indicating the phase transitions at high field are much more pronounced than those at low field. As mentioned before, the features at high field origin from those $\langle 111 \rangle$ axes which are nearly perpendicular to the applied magnetic field. Looking at the illustration of the crystal structure in Fig. 5.4, the perpendicular axes are labeled with B and C and the parallel axes with A and D. Since the four different $\langle 111 \rangle$ axes are not necessarily equally occupied, from the strength of the signal it seems that A and D are much less represented as the other two. This finding would also explain the easy and hard plane behavior of our sample.

In order to study the strength of this uniaxial anisotropy K_u and hence its effect on the stability of the skyrmion phase, we measure $\Delta f(\mathrm{H})$ for various angles of the applied magnetic field. At $\mathrm{T} = 11$ K we cover a range of about 120° in 2.5° steps. We assign the phase transitions by reading-out the dips appearing in Δf for the full data set. By tracking the transitions through the different orientations, we are able to determine which transition is caused by which of the four axes. Using this information, we can plot the phase transitions as a function of the magnetic field parallel and perpendicular to the [111] axis for each of the four axes A, B, C, D in Fig. 5.4. The resulting phase diagram is shown in Fig. 5.9. We observe that the expansion of the skyrmion lattice is rather limited in $H_{\parallel}$ compared to the field region in $H_{\perp}$ direction. The maximum field at which the skyrmion lattice can still be observed is for $H_{\perp}$ between 0.17 T and 0.23 T, and for $H_{\parallel}$ between 0.04 T and 0.05 T, which define the critical region where the three different phases meet. We conclude from this behavior that $H_{\perp}$ has a small influence, which means that K_u is strong and stabilizes the skyrmions along [111]. The transitions from the cycloidal to the skyrmion phase and the skyrmion phase to the FM for each axis tends to occur more on a nearly horizontal line as stronger k_u is, since $H_{\perp}$ has less influence [162]. This implies that the ratio between the values of $H_{\perp}$ and $H_{\parallel}$ in the critical region provides information about the

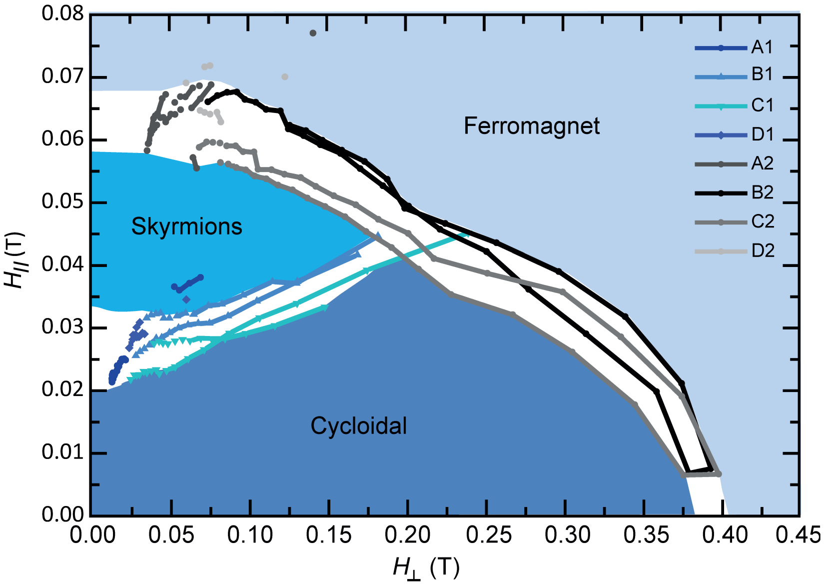

Figure 5.9: Phase diagram for GaV_4S_8 at T = 11 K, as a function of the magnetic field parallel to [111] and perpendicular to it. A, B, C and D are the four different axes, as shown in Fig. 5.4, each going through the two transitions. Colored regions of the diagram serve as guides to the eye.

strength of K_u. Using the information from the phase diagram, we calculate the maximum angle α_{max} between the magnetic field direction and the [111] axis at which the skyrmion lattice is still formed. To do that we consider the critical field region mentioned before, and determine α_{max}= $77.1° \pm 2.3°$, where the error is estimated from the standard deviation. We conclude that in a GaV_4S_8 single-crystal it is possible to have a skyrmion lattice formed along the crystal axis even if the misalignment of the applied field to the axis is α_{max}. Since α_{max} depends on K_u and T, the next step is estimating the strength of K_u knowing the other two. For this a theoretical model is needed.

The theoretical predictions illustrated in the following are made by A. Leonov, and are based on a continuous 2D model [162]. The magnetic energy of a non-centrosymmetric FM with C_{nv} symmetry is described by the sum of the symmetric exchange interaction, the DMI, the Zeeman energy and the anisotropy, which is assumed to be a uniaxial anisotropy. In order to determine the equilibrium states depending on the magnitude and direction of the applied magnetic field, numerical energy minimization using finite-difference discretization is performed. For the calculations an effective uniaxial anisotropy $k_u = K_u M^2 A/D$ is introduced, depending on the K_u the intrinsic uniaxial anisotropy, M the absolute value of the sample's magnetization, A the exchange stiffness and D the DMI constant. Furthermore fixed values for the DMI and the symmetric exchange interaction are chosen, and a few

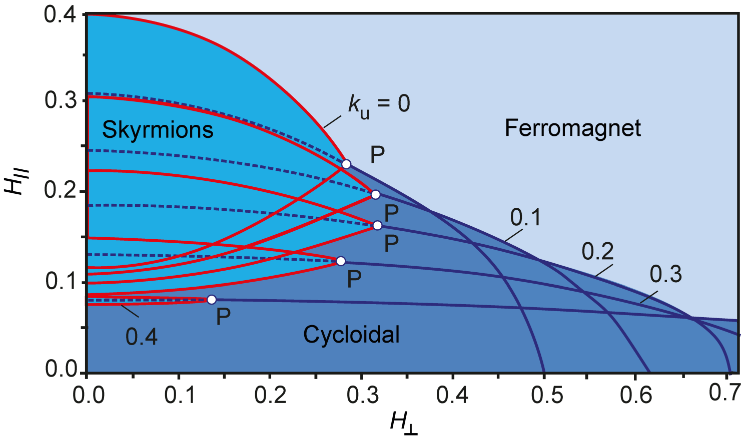

Figure 5.10: Calculated phase diagram for GaV$_4$S$_8$ at $T = 9$ K for different values of k_u as a function of the magnetic field parallel to [111] and perpendicular to it. This diagram is based on a 2D model and was made by A. Leonov [162]. More details about the procedure resulting to this phase diagram are given in the text.

different values of k_u included. The simulations result in the phase diagram shown in Fig. 5.10 for $T = 9$ K. Instead of a critical region as assigned in the results of the measurements, we obtain from the simulation a critical point P, defining the point where the three different phases meet. Comparing the experimental (Fig. 5.9) with the theoretical (Fig. 5.10) phase diagram, we see that the overall shape is very similar. Reading out P, we calculate α_{max} as a function of k_u, as depicted in Fig. 5.11. In this graph the maximum is around $k_u \approx 0.3$ at an angle of about 66°. For the simulation a temperature of around 9 K was assumed, while measurement were performed at around 11 K. Even considering a higher temperature the maximum angle which can be reached with the numerical simulation under these conditions and assumptions, is about 69°. Unfortunately, by comparing the experiment with these numerical simulations, we cannot determine a value for the uniaxial anisotropy. We were able to determine α_{max} with our measurements with what we can provide new and important information in order to improve the theoretical model.

5.5 Discussion and Conclusion

From the presented measurements we obtain an angle α_{max} significantly higher than what the numerical simulations predict, for which reason we are not able to obtain a value for the uniaxial anisotropy present in GaV$_4$S$_8$. The theoretical model is based on a 2D system compared to the 3D investigated structure, which could influence the results. For the numerical simulations it is assumed, among other things, that the Néel skyrmions align only along the

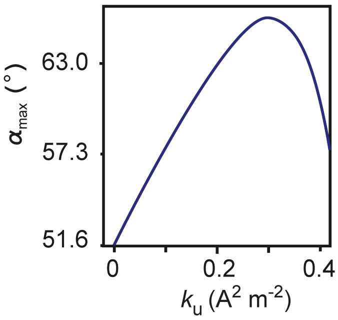

Figure 5.11: $\alpha_{max}(k_u)$ at $T = 9$ K calculated by reading-out P from the phase diagram shown in Fig. 5.10. The numerical simulations are made by A. Leonov [162].

$\langle 111 \rangle$ axis of the crystal and do not tilt away from this axis to align with the direction of the applied magnetic field. If instead even a slight rotation of the skyrmion away from the easy axis would be allowed, a bigger value for α_{max} from the numerical calculations would result.

Furthermore in the theoretical model only DMI, symmetric exchange, Zeeman energy and an easy axis anisotropy was considered, while also other components could contribute to the magnetic energy, as for instance an anisotropic exchange interaction [162]. Since the anisotropic exchange is small compared to the symmetric exchange, it is neglected frequently [163]. In our case the anisotropic exchange could have an influence and we should consider its contribution to explain the high value of the observed α_{max}.

Besides the possible problems of the numerical calculations a possible error of the measurements should be also taken into account. For instance, in the phase diagram, the same phase transitions of all four $\langle 111 \rangle$ axes should match up as a single line. A misalignment of a few degree is possible to occur and we try to account for that as we read-out the phase transitions. On the other hand, an error of a misalignment would not result in such a big discrepancy between experimental and theoretical results as we observe, but it would mainly reduce the error on α_{max} and not the value itself.

In conclusion we investigated the stability of the skyrmion lattice of a GaV_4S_8 single-crystal sample as a function of the orientation of the applied magnetic field. We find the skyrmion lattice still formed with a misalignment of $77.1° \pm 2.3°$ between the [111] crystal axis and the applied magnetic field direction. The observed α_{max} is significantly higher than the theoretical model predicted. The measurements are made using sensitive CM in the dynamic mode, which allows a non invasive investigation of individual samples. This study increases the understanding and knowledge about not yet intensively investigated compounds hosting Néel-type skyrmions with a C_{nv} crystal symmetry and shows the potential of the used technique. Furthermore, these measurements may also help to refine the theoretical model, such that it includes all the relevant interactions.

5.6 Outlook

A high stability of the skyrmion lattice phase was found in a single crystal of GaV_4S_8, due to a uniaxial anisotropy. Until now bulk magnetic materials containing Néel-type skyrmions are not yet intensively studied, since they have got discovered just recently [115, 117, 160, 161]. Besides these few studies on bulk samples, Néel-skyrmions were previously investigated in structures made of PdFe/Ir(111) bilayers, which have as well a strong uniaxial anisotropy [19].

Due to some fundamental properties of magnetic materials hosting Néel-skyrmions, these are of interest in condensed matter physics. As mentioned before, the relative size of the skyrmion lattice region in the phase diagram of materials hosting Néel-skyrmions is significantly larger than for the Bloch-type [113]. In addition, they have a sizeable electric polarization, thus offering the possibility to manipulate them by an electric field, which makes them attractive as possible information carriers in magnetic storage media or for other possible applications [115, 160]. Furthermore, due to the strong orientational confinement, Néel-skyrmions do not turn with the applied field as Bloch-skyrmions do, which makes them more robust against disturbance from outside and therefore better candidates for possible applications [117].

The research on bulk magnetic materials carrying Néel-type skyrmions is still at the beginning, and many things still need to be investigated to acquire more knowledge about this type. For instance in bulk materials, according to the authors knowledge, Néel-skyrmion were only observed in a lattice and not as isolated skyrmions in a mixture with another phase. The question is, is a mixed phase of cyloidal and skyrmion phase possible in bulk materials? According to theoretical predictions, under certain conditions like a big angle between the applied magnetic field and the axis along which the skyrmions form, a mixed phase should exist [162]. We did not see evidence of such a mixed phase as we have observed in the study of MnSi NWs described in chapter 4. This could also be due to the fact that this sample is so big that our sensitivity is not enough to detect single skyrmions occurring and vanishing, and therefore a smaller piece would probably help.

So far only a few compounds of Néel-type hosting materials are known and were grown. An interesting question is, if materials combination hosting Néel-skyrmions exist also at high temperature, as for instance the B20 crystal FeGe does in the case of Bloch-skyrmions [18], or have in another form a stabilized skyrmion lattice. For instance GaV_4Se_8 belongs to the same family as GaV_4S_8 and recently the first results on this compound were presented. Fujima *et al.* performed AC magnetic susceptibility and magnetoelectric measurements, finding an enhanced stabilization of the skyrmion lattice down to 2 K and up to a magnetic field of 370 mT in GaV_4Se_8 [164]. How do other material combinations of the same family behave? Furthermore, basic information about those materials is still missing, for instance: besides the uniaxial anisotropy, do other stabilization mechanisms like shape and surface effects exist and influence the stability of the skyrmion lattice? In order to reach the level of application, these and many other open questions leave room for further intriguing investigation.

6 Conclusion and Outlook

Magnetic materials constitute a field of research covered by continuous and large interest. Their broad use in various areas and their potential adaption in novel and promising applications motivates the search for new materials and investigation on their fundamental properties. Magnetic samples are in fact candidates for biological and biomedical applications [1, 2], magnetic sensing [3], high resolution imaging [4–6] and in logic devices [7]. Especially their potential adaption in high density magnetic storage media [8] increased in the recent years the interest in investigating different types and shapes of magnetic materials. Potential carriers of information could be for instance domain walls [10] or magnetic skyrmions [14–16]. A fundamental knowledge about the stability, the size and the controllability is needed before any kind of magnetic material can be implemented into a device [14, 17–19].

The motivation of this thesis is to give a contribution to the understanding of the growing, interesting and versatile field of magnetic materials by using DCM, which is sensitive, non-invasive and compatible to a broad range of samples with different properties. Using DCM we provide both complimentary and new information about the properties of novel or well-known magnetic materials, taking advantage of the high sensitivity of nanomechanical resonators [26, 27].

In fact, we demonstrate the use of DCM, in combination with numerical simulations, to study the process of magnetic reversal of short FM NT, which was, according to our knowledge, not yet experimentally observed. This reversal is driven by the nucleation of vortices at the end of the tubes and shows a strong aspect-ratio dependence. For instance, short FM NTs go through a vortex state and tubes above a certain length through a mixed state composed of a vortex at each end of the tube and an axial domain in the center. Apart from the aspect ratio, we find that the shape of the ends and impurities have a significant influence on the starting of the reversal process and how it evolves. A precise knowledge of the magnetic reversal is important, since a reliable process is needed for applications like magnetic storage.

We further investigate the stability of the skyrmion lattice phase of two different materials carrying the two different types of skyrmions. We measured

MnSi NWs hosting Bloch-type skyrmions and a GaV_4S_8 single crystal carrying Néel skyrmions. During the studies of MnSi NW we observed an unexpectedly stable skyrmion phase, extending from 29 K down to at least 0.4 K. The stability of the skyrmion lattice is strongly dependent on the applied magnetic field direction. An extended skyrmion lattice is present only if the long axis of the NW is parallel to the magnetic field. This stabilization occurs despite of the fact that the dimensions of the NW are too large to spatially confine the skyrmion lattice. In fact, an important difference between a NW and a single-crystal bulk sample is that a NW has an especially large surface-to-volume ratio for surfaces perpendicular to the long axis of the wire. The demagnetization influence of theses surfaces may produce an effective magnetic anisotropy which suppresses the conical phase, and therefore, in combination with a parallel applied magnetic field, stabilize and extend the skyrmion lattice.

The investigation of a single-crystal of GaV_4S_8 also resulted in a surprising stability of the skyrmion lattice phase. In this case, we studied the occurrence of the skyrmion phase depending on the orientation of the applied magnetic field. We found the skyrmion lattice still formed with a misalignment of $77.1^\circ \pm 2.3^\circ$ between the [111] crystal axis, which is the axis along which the skyrmions form in this material, and the applied magnetic field direction. The stability of the skyrmion phase is correlated with the strength of the uniaxial anisotropy present in this material. Since the observed stability is higher than what the theoretical model predicts, for the moment we cannot conclude on the strength of the anisotropy, but the findings could help to refine the model, so that it may include all relevant interactions and fit the experimental observations.

The performed studies show the diversity for which DCM measurements are suitable. In this work, we made measurements at room and low temperature in different magnetic field orientations, on a variety of sample sizes, covering NTs, NWs, and a piece of a single crystal. In general, the range of possible samples and measurement conditions is much broader. DCM is especially good for the study of small and/ or insulating samples for which conventional techniques are not applicable. Improved growing methods continuously provide new materials or combinations of magnetic materials which have unknown properties and could be investigated with DCM. Also some existing materials, especially which host Néel-type skyrmions are until now not investigated on shape and sized dependence.

Finally, we have investigated a method, RCM, to increase the measurement sensitivity at low field. By embedding RCM in our setup, we have obtained direct access to two directions of the magnetization of the sample. Apart from RCM, other methods like torque-mixing magnetic resonance spectroscopy [146] could be implemented in order to gain access into additional information like, the spin resonance. Future research in this direction opens room for obtaining a more complete understanding about magnetic materials.

A | Magnetometry Setup

In this appendix we illustrate the setup used for the investigation of the length dependence of the magnetic state of CoFeB NTs at low and at room temperature, as described in Chap. 3. This setup was also used for the study of the anisotropy of GaV_4S_8 by angle dependent measurements of the applied magnetic field, see Chap. 5. The used setup is a combination of two independent commercial close-cycle cryostats. One is the Montana system, which hosts the sample chamber and provides the possibility to control the temperature between 4.8 K and about 300 K, (Fig. A.1(b)). The second close-cycle system is a rotatable magnet which can reach a field of about 4.5 T, (Fig. A.1(a)). Both components and their handling are described in the following sections more in detail.

A.1 The Montana Cryostation

This section is dedicated to the technical details and the handling of the cryostation fabricated by Montana Instruments. It includes also a step-by-step guide for mounting and aligning the sample in our setup. The main reference is the manual provided by Montana Instruments [165].

A.1.1 Technical Details

The main components of the cryostation are the compressor, the control unit, the cryostat with a custom-made sample chamber, and the user interface to control the system, schematically shown in Fig. A.2. The variable-flow helium compressor is equipped with a microcontroller in order to achieve the needed cooling power. The controller regulates the compressor capsule and the motor of the cold-head drive. For an efficient and optimized operation several parameters like temperature, pressure, oil level, and oil flow are checked and used by the microcontroller to optimize the performance.

The electronics needed to operate the cryostat is placed in the control unit. The unit includes also the power supplies of the system, a pump, and a high frequency filter for the motor of the cryo-cooler.

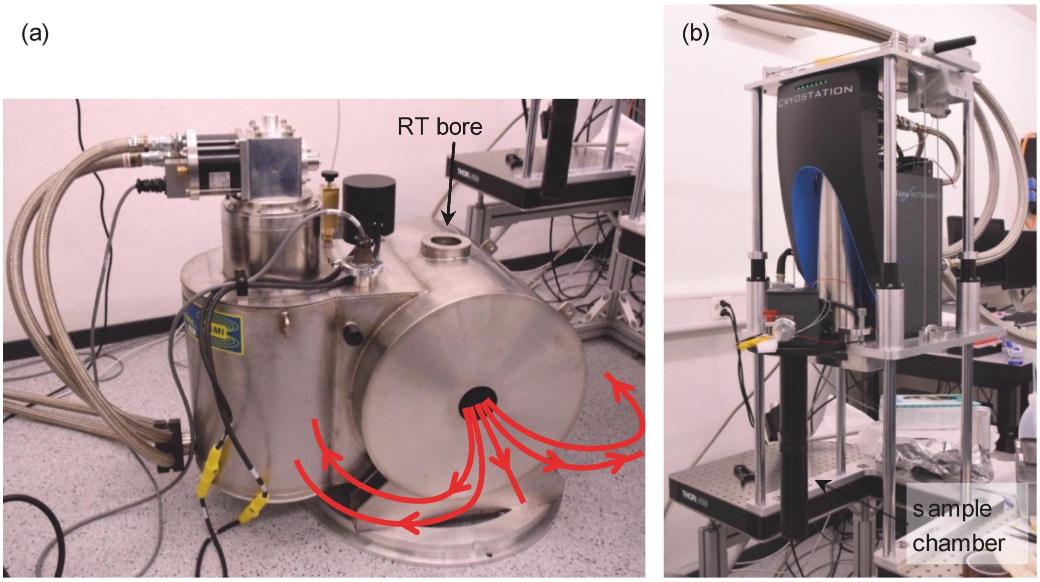

Figure A.1: The two components of the magnetometry setup. (a) The rotatable magnet with a room temperature bore where the sample chamber of (b) the Montana cryostation enters.

The cryostat itself is an assembly of a cooling tower and the sample chamber. It is connected via the He hoses to the compressor which supplies and returns the He. The vacuum line connects the pump of the control unit with the cryostat. Another link between these two components is an electrical connection needed for the control of the cryostat. The frame and the sample chamber are strongly fixed to the base and the cooling tower is floating with respect to them, therefore the propagation of the vibrations from the compressor is reduced. According to the manufacturers' specification, the stabilization of the vibration is below 5 nm peak-to-peak. In our setup additionally, the sample mount hangs from springs to further reduce the influence of environmental vibrations. The sample chamber contains also a Hall sensor and various electrical connections. A holder fixes the positions of the lens and the optical fiber, part of the interferometer for the readout of the cantilever motion, (see section 1.2.2). Two coils are mounted close to the cantilever, for the application of an AC-field, in order to perform RCM measurements, (see Sec. 1.5 and 3.2). In addition, the sample chamber is equipped with temperature sensors and heaters at different positions, monitored and controlled by a PID-loop to stabilize the desired temperature. All these components are surrounded by a radiation and a vacuum shield.

The cooling tower holds a Gifford-McMahon cryo-cooler providing the main cooling capacity. This cryo-cooler is part of a closed He loop and obtains pressurized He from the compressor. The cooler has two different stages and each of the stages is equipped with a temperature sensor and a heater for

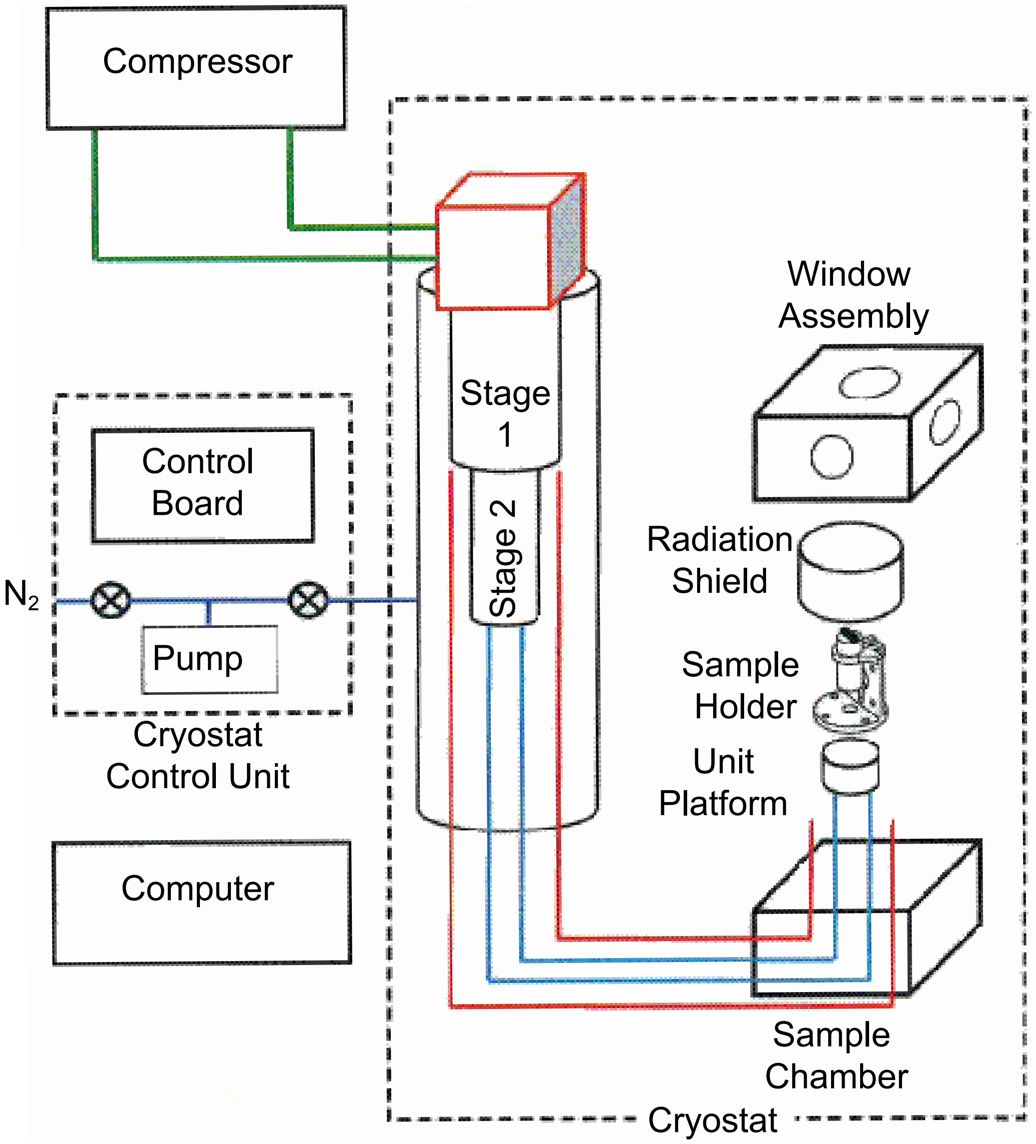

Figure A.2: Schematic of the main components of the Montana cryostation. The compressor, the control unit, and the user interface are drafted on the left side and the cryostation with its components on the right. In addition, several temperature sensors and heaters are mounted at different positions of the cryostat. Note that the sample mount for our setup is pointing down.

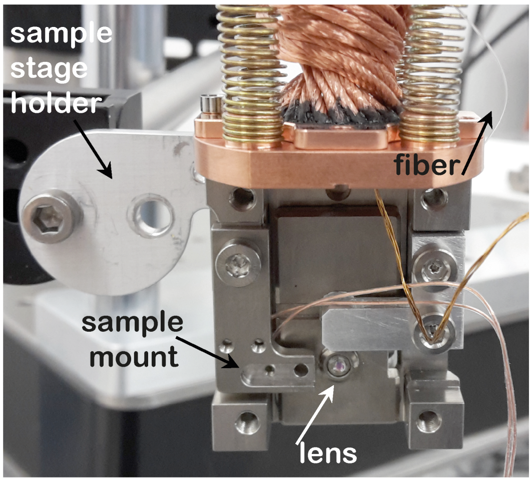

Figure A.3: The empty sample stage is fixed with a holder and the cantilever can be mounted in front of the lens.

observing and regulating the temperature of the system, see Fig. A.2. The first stage is in contact with the radiation shield and the second one with a platform connected to the sample stage.

The vacuum reached in the sample chamber with the pump of the control unit is rather weak. The remaining vapor is trapped by cryopumping charcoal adsorber. Since the sample holder is cooling down slower than the remaining parts, no condensation on the sample occurs. Using this combination a base pressure between 10^{-6} to 10^{-8} Torr can be reached, according to the manufacturers' instructions. In our custom made version with the special and long sample chamber with electrical connections going down, we can cover a temperature range of 4.7 K to 300 K with a stability below 10 mK peak-to-peak detected close to the sample.

A.1.2 Mounting and Aligning the Sample

In this section we schematically describe step-by-step the procedure of mounting and aligning the sample in the magnetometry setup.

- fix the sample space 90° rotated compared to how it is shown in Fig. A.3, so that the surface visible on the picture is parallel to the floor
- mount the cantilever clamped in a special holder with a Titanium screw to the sample mount
- put the sample stage back to the initial position as in Fig. A.3 and fix it.

During the alignment in this setup, the holder of the fiber plus lens is moved with respect to the cantilever.

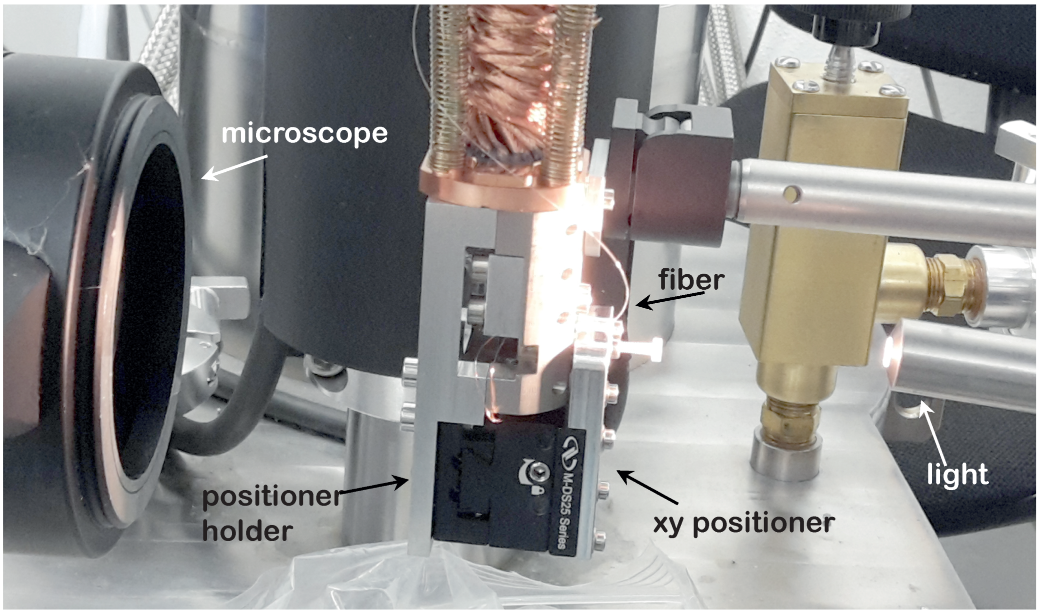

Figure A.4: Sample stage is ready for the alignment. XY-positioner is mounted to the sample stage with a special holder. The light microscope is in the position to make the alignment.

- mount the positioner holder and the xy-positioner as shown in Fig. A.4
- position the microscope and couple the light of a lamp with a flexible neck from the back into the fiber, see Fig. A.4
- check the distance between cantilever and lens: it should be the same as between lens and fiber end. If the distances are correct, the image of the fiber end should be in the same focal plane as the cantilever,
- if the distance is not correct, loosen the fiber chuck (small set screw with hexagon socket, access from the side)
- push with the plastic screw the fiber chuck gently in the right position (it may be necessary to pull it first gently out) and fix the fiber chuck afterwards
- loosen slightly the screw of the holder of the fiber and lens (big screw at the back of the stage)
- observe through the microscope and position the fiber behind the cantilever (respectively the paddle) by using the xy-positioner
- drive the cantilever through the piezo with a low frequency signal (from the DAC card with an amplitude of 10 V, connected through the high voltage amplifier (gain = 40) to the piezo)
- look at the DC signal from the photo detector
- optimize the signal; peak-to-peak the voltage, should be between 0.6 and 1.5 V, depending on the cantilever (if the gain of the DC preamplifier is 10 and the laser power is about 100 nW)
- turn off the high voltage

- tight carefully the screw at the back of the sample stage to fix the position of the fiber chuck
- check the signal, if you lost too much re-do the alignment otherwise
- dismount the xy-positioner and the positioner holder
- mount in front of the cantilever (instead of the positioner holder) a Titanium piece for a better weight distribution; the piece also includes coils to perform RCM measurements (see Sec. 1.5 and 3.2)
- fix the Titanium piece also to the copper piece at the top with screws, screw it properly since these is an important thermal contact
- plug in the electrical connections of the RCM coils
- check from the dc signal of the photo detector if the alignment of the cantilever is still fine
- loosen the sample stage
- check if the sample stage hangs straight, otherwise correct it by screwing or unscrewing the nuts attached to the top of the springs
- close the radiation shield
- close the vacuum shield

The system is ready to pump and cool down. Details to this process are given in the next section.

A.1.3 Operation of the Cryostation

After the sample chamber is closed with the two different shields you can start the cool down:

- turn on the control unit
- turn on the compressor and wait about 20 s, the front panel of the compressor will show the initializing and self-test countdown
- start the user interface for the control of the Montana cryostat
- before starting with the cool down, test shortly the vacuum; open the **MANUAL CONTROL** tab in the **SYSTEM** menu of the user interface and check the option **ENABLE MANUAL CONTROL**; now you can turn on the pump and open the case valve; you should see the pressure dropping (you may have to press slightly at the top lead, the window assembly Fig. A.2, of the sample chamber)
- in order to use the automatic cool down, deactivate the manual control
- click ⊕ the target button and enter the wanted temperature in the dialog box which opens; press **OK**
- press ↓ the cool down button to start the process
- open the **PREFERENCES** tab and click on the **ENABLE EXTERNAL CONTROL** option, so that the NI LabVIEW programs have access to the actual temperature

- start to checking the fringe during the cool down
- about 4.5 h are necessary to reach the base temperature
- if you want to change the temperature press again ⊕ the target button, enter the wanted temperature and press ↓ the cool down button to start
- do not close the user interface during measurements, if you close it, the system stops cooling and will warm-up
- if you are done, press ↑ to warm-up the system, everything is automatic so the system will stop heating when a temperature of 285 K is reached and will vent with N_2.

A.2 Rotatable Magnet

The second component of the magnetometry setup is the magnet produced by American Magnetics Incorporated. In the following we describe the technical details and the handling of the system, therefore the manual provided by the manufacturer is used as the main reference [166].

A.2.1 Technical Details

The magnet is a custom-made cryogen-free system. The main components of the system are the cryostat, the compressor and the electrical equipment. The compressor of the type F-70H is manufactured by Sumitomo (SHI) Cryogenics of America, Inc.. The compressor supplies the cold head which is attached to the cryostat with high pressurized, oil-free He. It is connected via He hoses to the cold head. Apart from the He lines, an electrical connection between the compressor and the cold head is used for the control.

The cryostat contains a split coil made out of superconducting material. For electrical isolation an epoxy is used between the windings. The coil is surrounded by a vacuum chamber for thermal isolation from the environment. The cryostat is cooled by a cold head connected to the coils. The cold head is a two-stage refrigerator which is based on the principle of a Gifford-McMahon refrigeration cycle. At different position of the cryostat temperature sensors are placed. These sensors are monitored by the electrical equipment, which also controls and monitors the current applied to the coil.

The cryostat has two room temperature bores, see A.1(a). The vertical radial access has a diameter of 2.4 inch and into this bore we insert the sample chamber of the Montana setup. The possible orientation of the magnetic field lines are sketched in Fig. A.1(a). Since the magnet is mounted on a rotatable ring, the magnetic field direction can be changed in one plane with respect to the sample which is fixed in position.

A.2.2 Operation of the Magnet

The following section illustrates the handling of the magnet. Before one can start applying a magnetic field, a few things have to be done. The necessary steps are listed in headwords:

- first of all turn on the LakeShore temperature monitor in the electronic rack
- check the He pressure of the compressor, it is supposed to be 207 - 212 PSIG at 68 °F, respectively 1.43 to 1.46 MPa at 20 °C
- turn on the compressor and the cold head will start working
- coming from RT the system needs about 50 h to cool down
- temperatures at the different sensors are suppose to be T_1 ~2.7 K (2nd stage of cryocooler), T_2 ~3.1 K (magnet), T_6 ~39.1 K (high temperature superconductor) and T_7 ~39.1 K (high temperature superconductor)
- magnet is ready for operation as soon as the temperatures are close to these values
- turn on the electronic control of the magnet (AMI Model 430 programmer)
- turn on the power supply of the magnet (AMI Model 4Q06125PS), wait a short moment before following the instruction below
- press **ENTER** and the default display will appear
- rotate the magnet in the wanted orientation
- from now on one can use NI LabVIEW to control the magnet and apply fields, or
- press the **PERSIST. SWITCH CONTROL** button to heat up the magnet persistent switch, which will need 20 s
- press **TARGET FIELD/CURRENT** and type the wanted field and press **RAMP/PAUSE**
- the LED **CURRENT LEADS ENERGIZED** will turn on and will turn off as soon as the field is reached and then
- **FIELD AT TARGET** LED will turn on
- by pressing **RAMP TO ZERO** the field will be ramp down
- to turn off the magnet after having ramped it down to zero, first turn off the power supply, afterwards the electronic control, and then the compressor

If a field is applied, one should remove magnetic materials from the close surrounding of the magnet and make sure that the temperature of the magnet is low in order to prevent a quench. It seems that a quench is more probable if the temperature on the four sensors show higher values as usual. Slightly higher temperatures are normal if sweeping the magnet, but it could also be a sign of dropping pressure in the closed cycle He lines due to a leak. The load on the superconducting magnet is permanently monitored by the control electronics (AMI Model 430 programmer). It can automatically detect a field/current quench and in this case the output voltage of the power supply is automatically set to zero. If a quench occurred:

- the **MAGNET QUENCH** LED will be on
- clear the quench detection by pressing **SHIFT** and then **RESET QUENCH** otherwise the electronic control is blocked
- due to the quench the temperatures of the magnet increased, wait for cooling down and reaching about base temperature before using the magnet again; duration 3 to 4 h

A.3 Some Hints for the Next Generation of PhD-Students

This short section is written in the spirit of learning from the mistakes and experience of others.

Attention should be paid to a few things with the previously described setup. The resonance frequency of a cantilever should not be too low. If the resonance frequency is too low, the frequency of the two compressors will couple very well to the system and you will struggle to run the measurements stably. Try to work with cantilevers which have a resonance frequency above 1 kHz, or even 2 kHz to be on the safe side. Consider also that by attaching a sample to a cantilever you will reduce the resonance frequency.

If you have the sample chamber of the Montana cryostation too long open, then the cryopumping charcoal adsorber will saturate. If you then cool down, the vacuum will not be as good as it used to. In case the sample chamber was for a longer time open, close the sample chamber and pump it out without starting the cool down. After pumping for a while, vent the chamber with pure N_2 and pump it out again. Repeat this procedure a few times and the charcoal adsorber should be active again.

In case you want to perform measurements only at room temperature, it is not necessary to cool down the system in order to reach the needed vacuum. Just connect with an adapter at the top of the sample chamber a combination of three pumps: use a roughing pump, a turbo pump and an ion pump. Try to mount the ion pump as close as possible to the system but as far as necessary not to induce a quench of the magnet.

B | ^{3}He System

This chapter provides a short introduction into the technical details and the operation of the ^{3}He cryostat from Janis Research Company. The described system was used for the investigation of the skyrmion phase in MnSi NWs, (see chapter 4). In the first section the focus is more on the technical details, while the second part gives in key words a short manual for the handling of the system.

B.1 ^{3}He Cryostat

In order to perform sensitive DCM measurements, a good vibration isolation from the environment is required. This is ensured by a compressed-air suspended table to which the cryostat is attached, see Fig. B.1(a). Additionally, the sample stage hangs from springs and is mounted inside a vacuum chamber. The sample is mounted on a special holder and all the parts necessary for the readout of the cantilever‘s motion are mounted to the sample stage. Needed for the read out are one end of a fiber, a lens, diverse holders, and setscrews for positioning. These components build up an optical fiber interferometer, Fig. B.1(b). More details about the parts and the principle of a fiber interferometer are given in section 1.2.2. Furthermore, underneath the cantilever mount there is a stack of piezo-based nanopositioners (Attocube). On top of this stack various things can be mounted, depending on which kind of experiment is performed. For example, figure B.1(b) shows a holder with two coils, which are used to perform RCM measurments, see Sec. 1.5 and sec:RCMexp for more details. The chamber contains also a temperature sensor, a hall bar and various electrical connections. During the measurement the pressure in the sample chamber is below 10^{-6} mbar.

The ^{3}He cryostat includes a ^{4}He bath, in which an inner vacuum chamber (IVC) is placed. The IVC encloses the sample chamber and, due to the vacuum, it enables the flexibility, of changing the temperature independently of the ^{4}He-bath. The system is additionally equipped with a closed-cycle ^{3}He circulation. The ^{3}He line is in good thermal contact to a small separated ^{4}He reservoir. By pumping on this separated reservoir, the temperature drops

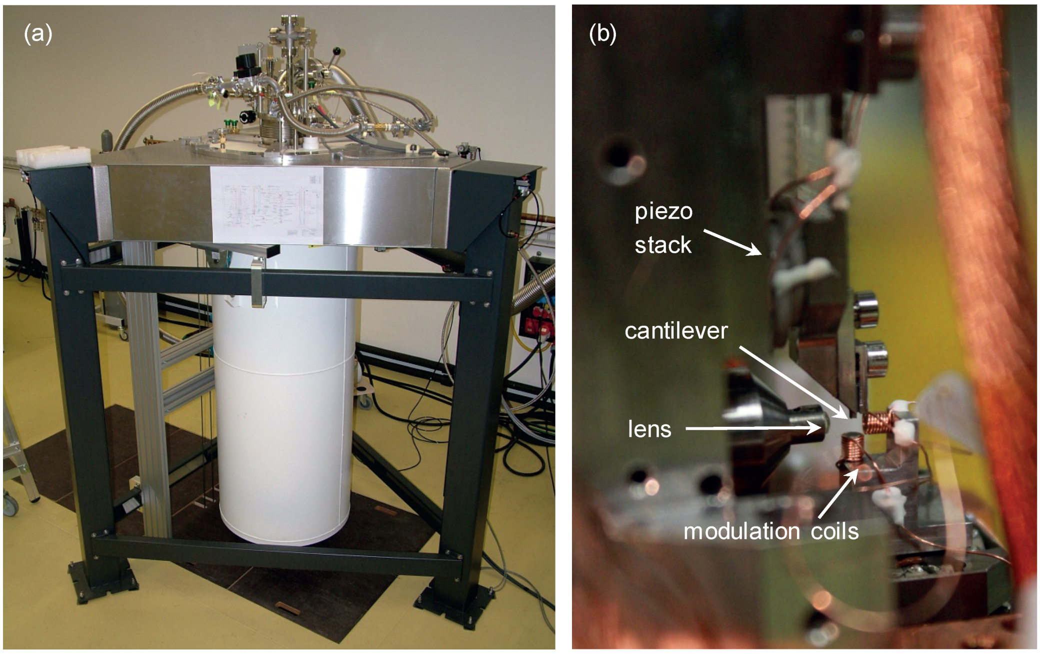

Figure B.1: (a) Picture of the cryostat attached to the air suspended table. (b) Shown is the sample mount from the side. The setup includes the cantilever, the components of the optical fiber interferometer and additionally a pair of coils are mounted for performing RCM measurements.

from 4.2 K to 1 K, and for this reason the reservoir is called the 1 K-pot. The 1 K-pot pre-cools the ^{3}He which by pumping on it, allows reaching a temperature below 300 mK. Since the sample space is decoupled from the He-bath, with this cryostat a big temperature range can be covered. Temperatures below 300 mK can be reached and it is still possible to stabilize temperatures up to about 100 K. A few thermal sensors and heaters are mounted at different positions of the system and the temperature is stabilized via a PID-loop.

The IVC is surrounded by a superconducting NbTi/Cu coil immersed in the ^{4}He. With this superconducting magnet (Cryomagnetics) we can apply a magnetic field up to ±6 T parallel to the long axis of the cantilever.

B.2 Manual for the Operation of the System

This section is devoted to the handling of the ^{3}He cryostat which was used for some of the previously shown measurements. The steps necessary for operating this system are listed in headwords.

B.2.1 Install the Sample

First, mount the cantilever which is clamped in a holder, to a special Titanium piece which has a piezo stack attached, see Fig. B.1(b). The piezos are used to drive the cantilever at its resonance frequency. Start with

- fixing the sample stage with a special holder
- mount the cantilever together with this special Titanium piece in the system
- plug in the connection of the piezo stack
- make a rough alignment using a microscope and move the cantilever together with the holder, bring the cantilever as good as possible in front of the fiber
- pay attention to the angle of the cantilever with respect to the vertical direction, correct for it if necessary
- check from the side the distance between cantilever and front of the lens, it is supposed to be 1.69 mm, to this purpose, set the stereo microscope to the 5-times scale and set the distance to 84.5 divisions (small ticks - in the past we have seen that everything between 84-86 divisions works)
- if the distance is not correct, loosen the fiber, pull it carefully out and push it gently by using a screw into the correct position, fix the fiber chuck again
- make a fine alignment by moving the fiber with the setscrews
- drive the cantilever through the piezo on which a low-frequency AC signal is applied, more details are given in A.1.2
- read out the peak-to-peak voltage of the DC fringe value
- if the preamplifier gain of the DC signal is 10 and the laser power is set to 100 nW, the voltage readout should be of about 1 V

Due to thermal contraction during the cool-down a distortion, of the sample mount is induced. In order not to loose the alignment, we counter act and make a mis-alignment of the cantilever before cooling down. Therefore:

- push the fiber down till the maximum fringe value is reduced by 10 %
- push the fiber towards the wall till another 5 % of the maximum value of the fringe is lost
- check if the screws are all tight
- remove the holder which fixes the sample stage

Monitor the fringe during the cool-down in order to take soon action if something goes wrong.

B.2.2 Cool Down of the System

After having mounted the sample, start to close the system:

- use the 1-mm (diameter) Indium for the O-ring seal of the sample chamber
- close the sample chamber, pump for a few hours
- make a leak-check, using the RGA
- make the O-ring seal of the IVC (inner vacuum chamber) by using the 1-mm Indium and a bit of vacuum grease
- close the IVC and pump over night, than leak check
- pull-up the dewar

Perform now the first tests at room temperature:

- fill the cold trap dewar with liquid N_2
- make ^{3}He flow test at RT (procedure described in the next section)
- characterize the cantilever

Continue to prepare and start with the cool down:

- pump out the dewar
- fill dewar with N_2 gas and pump out 3 times
- fill dewar with slight overpressure and fill the 1 K pot through the needle valve, pump out 2-3 times
- dewar and 1 K pot have a slight overpressure
- put $\sim$100 mbar N_2 exchange gas in the IVC (turn off IVC pump)
- insert both the transfer lines (one with the rubber attached, special for LN_2 transfer), to reach the bottom of the dewar
- take away the blind flange
- pump on the 1 K pot, have the needle valve close and the main space (to the pump) closed
- start fringe look program
- start with the liquid N_2 transfer
- during transfer open once a while the needle valve, pressure goes up (if just gas, it is maybe necessary to close the valve to the pump to see an effect); before reaching $T = 150$ K stop it
- after transfer put on the overpressure valve
- let the system cool down over night

After 77 K have been reached:

- characterize the cantilever
- make ^{3}He flow test, see next section

Continue with cleaning the dewar from LN_2 and continue then to cool down to liquid He temperature, therefore:

- turn on the IVC pump to remove the exchange gas
- mount the blind flange
- connect the He gas cylinder (from pump side) to the dewar to push out the liquid N_2
- open the gas cylinder and push out the liquid N_2 completely
- remove transfer line with the rubber tube, leave the inset which reaches the bottom of the dewar
- fill the dewar with He gas and pump out 3 times, connect the exhaust of the 1 K pot pump to the He-recovery line
- fill dewar with slight overpressure and fill the 1 K pot through the needle valve, pump out 2-3 times
- dewar should remain with slight overpressure
- put 10 mbar exchange gas (He) into the IVC, 4-5 shoots (clean out first the line)
- have the inset transfer line in the dewar, in order to reach the bottom of the cryostat
- open the valve to the recovery line (red handle)
- use the He transfer line and start with the transfer of liquid He (takes about 1.5 h)
- start to detect the fringe
- take out the exchange gas of the IVC before reaching 20 K
- after the transfer is done, take out both transfer lines

While the system is cooling down, the ^{3}He circulation can be started:

- open the valves on the system: the green and the big black, if not already open (V19 and V20)
- open the needle valve slightly, and have the 1 K pot pump running
- open valve V5 (V15, V14, V12, V3/V3A and V4/V4A should be still open and remaining valves should be closed from the flow test at 77 K)
- start pump (green, middle, down(PPM start)) and slowly open valve V1

B.2.3 ^{3}He Flow Test

The following procedure is performed at room temperature and at 77 K in order to check if the lines of the ^{3}He circulation are free. To perform the flow test follow the next steps:

- refill the LN_2 of the cold trap

- switch on pump (PPM Start)
- open V1, V4/V4A, V5, V6, V19, V20 and pump out the system
- wait until Pirani gauge shows Lo10-4 or a low 10-3 (∼4h @ RT)
- close V4 or V4A
- open V15, V14, V12, V3 or V3A and wait 5 min to let the ^{3}He enter the system
- close V1, V6 and open V4 or V4A
- start logging the flow and pressure of the Pirani gauge for 10 min
- afterwards flood the system, open V6 and wait till the flow goes back to base value (∼0.020, ∼5min)
- then close V3/V3A, and SLOWLY open V1
- leave the system pumping until at LN_2 (when coming from RT)
- when Pirani gauge has reached Lo10-4, close all valves and shut off the pump
- when cooling down the system, keep pumping on the system (V4/V4A, V5, V20, V19, V1 open, V3/V3A closed) in order to prevent a clog

B.2.4 Warm up the Cryostat

After the measurements are done, the system has to prepare for the warm up:

- turn off the magnet
- unlock the fringe
- close the needle valve
- turn off the 1 K pot pump
- open the valve between the main space and the 1 K pot
- turn on the IVC and the sample chamber pump
- to pump out the ^{3}He close the cold trap entrance valves (V3/or V3A)
- open valve V6
- keep pumping till the temperature of the system is over 77K (longer does not hurt)
- close all valves: V4 or V4A, V5, V6, V19(top of the cryostat, big handle), V20 (top of the cryostat, green swaglock), V1, V12, V14
- turn off the He circulation pump (PPM STOP)
- put the floating table down
- close the connection to the He-recovery line and disconnect the connections to the magnet and the level meter
- take away the over pressure valve and put on the blind flange
- lower the dewar and put the flange above the opening

B.2.5 Clean out the Cold Trap

^{3}He passes through a LN_2 cooled region before entering the cryostat. In this cold trap everything with a boiling point above 77 K solidifies, like oil water and so on. At some point this trap is saturated and needs to be cleaned out. Therefore follow the following steps:

- the cold trap is cold and dipped in LN_2
- pump out the cold trap, have V3/V3A closed, V4/V4A open and open V6 and V1
- have V12, V14 and V15 open so that the ^{3}He can go back to the dump and have all the other valves closed
- pump out till the Pirani gauge shows LO 10-4
- check if the entire ^{3}He is in the dump
- close V4/V4A and close the valves in front of the dump
- check if V4/V4A and V3/V3A are really closed
- connect a pump to the port A and turn it on
- take out the cold trap from the LN_2 bath
- open V10/V10A, you should see an increase of the pressure at gauge 4 if the trap was dirty
- if pump is on speed (and pressure low about 10^{-7} mbar) open V11 slowly to start pumping on the trap
- use a heat gun and warm up the cold trap, watch out not to damage the indium seals, should see increase of the pressure
- let it pump down and heat up again, repeat a few times till you do not see a significant increase of the pressure when warming up
- pump on the cold trap till reaching a low 10^{-6} mbar
- close V11 and V10/V10A, cold trap is ready to be used again

Acknowledgements

This work would not have been possible without the help, advice, and support of many people. I am very thankful for all of those, that I would like to acknowledge in the following.

During the time of my PhD I had the chance to work with several different nice, friendly personalities helping me through my PhD. First off all I would like to thank Martino Poggio. Thanks a lot Martino, your office door was always open, thanks for your patience and your advice. I learned a lot from you, and not just theoretically but also practically. Most of the times you were the best person to ask for advice. Thanks for giving me the freedom of approaching the things first by my self, but even more thanks for your advice and hints trying to solve problems and tricky situations. It was a pleasure to have you as a boss.

Thanks Thomas Mühl that you immediately accepted my request to evaluate my work and that you have saved your time for doing that and for the defense. Ilaria Zardo, thank you that you took the time to chair my defense. Even more, thanks for the conversations we had and the coffee breaks we spent together.

During my time in the Poggio group I was working on different projects which gave me the possibility to learn from and work with different people. I started to work together with Michele Montinaro and later Hari Solanki. Thanks to them I learned a lot in terms of sample processing and working in a clean-room. Thanks for your company, thanks for your advice, thanks for your patience of teaching to me, the young and inexperienced one. Afterwards a new topic and a new collaboration started. Thanks Fei Xue for sharing your experience with me, teaching me attaching tiny things to the end of cantilevers and introducing me to the fascinating world of skyrmions. A big thanks goes also to the first two guys which started with cantilever magnetometry measurements in our group. Thanks Dennis Weber for sharing your ”long life experience” with me and Arne Buchter for teaching me with your calmness how to handle the ^{3}He system. Both of you were always available and very helpful when I had a question. I first introduced you Boris Groß into the world of cantilever magnetometry, and in the world of the strange vortex-like spin structures. But what I got back was more than what I gave. Whenever

I had a question you always took the time to help me, to explain me, and trying to calm me down. Thank you for your support and your company. Furthermore, Marcus Wyss thanks a lot for introducing me to the FIB and letting me enter into the crazy world of beam-lines. Since you, Simon Philipp, started recently in the final phase of my PhD, it was a bit difficult for me to spend as much time as I would have like to, for introducing you into the sample fabrication and so on. I hope I could teach you the most important things. Thanks for trying to be helpful and to support me whenever it was possible for you even at this early stage of your PhD. I really appreciate.

A big thanks goes to all the group members and former members. I did not work directly with all of you but it was always possible to find a pair of helping hands or getting an advice without asking twice. Also thank you for providing some distraction during the joined lunch and coffee breaks. Thanks for that Benedikt, Davide, Floris, Nicola, Denis, Thibaud, Lorenzo, Giulio. It was a pleasure to work in the same group with you. Besides the group members I would like to thank Christina Psaroudaki. Thank you for your prompt replies to my questions and your theoretical support.

In addition I would also like to thank Claudia Wirth, Audrey Fischer, Barbara Kammeramann, Astrid Kalt, and Germain Weaver, if there was a problem or an advice needed you were always there and helpful. If something was broken, the right tool was missing, urgently some helium was needed, a new setup was built up or some strong helping hands were needed, one of you was always willing to help, thanks for that: Sascha Martin, Dominik Sifrig, Patrick Stöcklin, Bernd Heimann, Heinz Breitenstein, Stefan Gentsch and Michael Steinacher. Thank you Beat Glatz for your IT support and helping to deal with the Comsol business.

Making a PhD offered me the possibility to work with different people also from outside the department. I enjoyed working in cooperation with people from various background and different cultures. During the last years I was working on different projects and therefore with different people. Some of you I met in person, with others I had just contact via mail or Skype. Of all the interactions I had, I keep good memories. Thanks, Song Jin and your PhD student Dong Liang, and Matthew Stolt for our nice cooperation on the MnSi NWs. This project opened for me the fascinating world of skyrmions. Thanks to Anna Fontcuberta i Morral and Dirk Grundler for the cooperation on the CoFeB NTs and the conversations we had during conferences with you and your students and post-docs. Thank you Istvan Kézsmárki, Andrey Leonov, Vladimir Tsurkan, and Alois Loidl for the cooperation on the GaV_4S_8, the useful Skype conversations and email exchanges.

Besides the scientific support, sometimes other kind of support is as important during the time of the PhD. My family was always a big support for me, always there if I needed something and believing in my capabilities

more than I do myself. Thank you mum, allowing me always to do whatever I wanted, to follow my dreams and trusting in me that I will find the right way for me. Thanks to my sisters listening to my annoying stories of what happened at work, not really understanding what I was talking about, but always trying to motivate or at least to distract me.

Last but absolutely not less important, a special thanks goes to Michele. You welcomed me warmly into the group, helped me with the start, and you helped me to complete, and finish the work. Thanks for your advice, your proof-reading, your patience, your support, your hugs, being there for me always and to any time and for so much more. Using words I cannot express what you and my family mean to me. Thanks for everything.

Basel, April 2017,

Andrea Mehlin

Curriculum Vitae

Andrea Mehlin

University of Basel
Department of Phyiscs
Klingelbergstrasse 82
CH-4056 Basel, Switzerland

Personal Information

Birth: 20.09.1986 in Lörrach, Germany
Citizenship: German
Languages: German (native), English (Business proficiency), Italian (B1/B2)

Education

- June 2017, **Ph.D. in Physics**
  University of Basel, Switzerland
  Thesis: Dynamic Cantilever Magnetometry of Reversal Processes and Phase Transitions in Individual Nanomagnets
  Advisors: Prof. M. Poggio, University of Basel
  External Reviewer: Dr. T. Mühl, IFW Dresden

- June 2012, **M.Sc in Nanosience, Major in Physics**
  University of Basel, Switzerland
  Thesis: A Quantum Point Contact as Sensitive Sensor of Cantilever Motion
  Advisors: Prof. M. Poggio, Dr. M. Montinaro
  Second Reviewer: Prof. E. Meyer

- July 2010 **B.Sc. in Nanoience**
  University of Basel, Switzerland

- June 2006, **Abitur**
  Hauswirtschaftliche Schule Lörrach, biotechnologische Richtung, Germany

List of Publications

2017: **Néel-type Skyrmions in Multiferroic Lacunar Spinels – Mapping out a Stability Phase Diagram using Dynamic Cantilever Magnetometry**
Mehlin, A., Gross, B., Kézsmárki, I., Leonov, A., Tsurkan, V., Loidl, A., and Poggio, M. *in preparation* (2017)

Observation of Magnetization Reversal Nucleation Induced by Vortices in Individual Ferromagnetic Nanotubes
Mehlin, A., Gross, B., Wyss, M., Tütüncüoglu, G., Heimbach, F., Foncuberta i. Morral, A., Grundler, D., and Poggio, M. *in preparation* (2017)

Imaging Magnetic Vortex Configurations in Ferromagnetic Nanotubes
Wyss, M., Mehlin, A., Gross, B., Farhan, A., Buzzi, M., Kleibert, A., Tütüncüoglu, G., Heimbach, F., Foncuberta i. Morral, A., Grundler, D., and Poggio, M. *Physical Review B* **96**, 024423 (2017)

2015: **Stabilized Skyrmion Phase in MnSi Nanowires Detected by Dynamic Cantilever Magnetometry**
Mehlin, A., Xue, F., Liang, D., Du, H., Stolt, M. J., Jin, S., Tian, M., and Poggio, M. *Nano Letters* **15**, 4839 (2015)

2012: **Feedback Cooling of Cantilever Motion using a Quantum Point Contact Transducer**
Montinaro, M., Mehlin, A., Solanki, H. S., Peddibhotla, P., Mack, S., Awschalom, D. D., and Poggio, M. *Applied Physics Letters* **101**, 133104 (2012)

Grating-Based Tomography of Human Tissues
Müller, B., Schulz, G., Mehlin, A., Herzen, J., Lang, S., Holme, M., Zanette, I., Hieber, S., Deyhle, H., Beckmann, F., Pfeiffer, F., and Weitkamp, T. *AIP Conference Proceedings* **1466**, 107 (2012)

References

[1] Pankhurst, Q. A., Connolly, J., Jones, S. K. and Dobson, J. Applications of magnetic nanoparticles in biomedicine. *Journal of Physics D: Applied Physics* **36**, R167 (2003).

[2] Son, S. J., Reichel, J., He, B., Schuchman, M. and Lee, S. B. Magnetic Nanotubes for Magnetic-Field-Assisted Bioseparation, Biointeraction, and Drug Delivery. *Journal of the American Chemical Society* **127**, 7316–7317 (2005).

[3] Maqableh, M. M., Huang, X., Sung, S.-Y., Reddy, K. S. M., Norby, G., Victora, R. H. and Stadler, B. J. H. Low-Resistivity 10 nm Diameter Magnetic Sensors. *Nano Letters* **12**, 4102–4109 (2012).

[4] Khizroev, S., Kryder, M. H., Litvinov, D. and Thompson, D. A. Direct observation of magnetization switching in focused-ion-beam-fabricated magnetic nanotubes. *Applied Physics Letters* **81**, 2256–2257 (2002).

[5] Poggio, M. and Degen, C. L. Force-detected nuclear magnetic resonance: recent advances and future challenges. *Nanotechnology* **21**, 342001 (2010).

[6] Campanella, H., Jaafar, M., Llobet, J., Esteve, J., Vázquez, M., Asenjo, A., Real, R. P. d. and Plaza, J. A. Nanomagnets with high shape anisotropy and strong crystalline anisotropy: perspectives on magnetic force microscopy. *Nanotechnology* **22**, 505301 (2011).

[7] Allwood, D. A. Magnetic Domain-Wall Logic. *Science* **309**, 1688–1692 (2005).

[8] Parkin, S. S. P., Hayashi, M. and Thomas, L. Magnetic Domain-Wall Racetrack Memory. *Science* **320**, 190–194 (2008).

[9] Han, X. F., Wen, Z. C. and Wei, H. X. Nanoring magnetic tunnel junction and its application in magnetic random access memory demo devices with spin-polarized current switching (invited). *Journal of Applied Physics* **103**, 07E933 (2008).

[10] López-López, J., Cortés-Ortuño, D. and Landeros, P. Role of anisotropy on the domain wall properties of ferromagnetic nanotubes. *Journal of Magnetism and Magnetic Materials* **324**, 2024 – 2029 (2012).

[11] Mühlbauer, S., Binz, B., Jonietz, F., Pfleiderer, C., Rosch, A., Neubauer, A., Georgii, R. and Böni, P. Skyrmion Lattice in a Chiral Magnet. *Science* **323**, 915–919 (2009).

[12] Neubauer, A., Pfleiderer, C., Binz, B., Rosch, A., Ritz, R., Niklowitz, P. G. and Böni, P. Topological Hall Effect in the A Phase of MnSi. *Phys. Rev. Lett.* **102**, 186602 (2009).

[13] Pappas, C., Lelièvre-Berna, E., Falus, P., Bentley, P. M., Moskvin, E., Grigoriev, S., Fouquet, P. and Farago, B. Chiral Paramagnetic Skyrmion-like Phase in MnSi. *Phys. Rev. Lett.* **102**, 197202 (2009).

[14] Fert, A., Cros, V. and Sampaio, J. Skyrmions on the track. *Nat Nano* **8**, 152–156 (2013).

[15] Jonietz, F., Mühlbauer, S., Pfleiderer, C., Neubauer, A., Münzer, W., Bauer, A., Adams, T., Georgii, R., Böni, P., Duine, R. A., Everschor, K., Garst, M. and Rosch, A. Spin Transfer Torques in MnSi at Ultralow Current Densities. *Science* **330**, 1648–1651 (2010).

[16] Yu, X. Z., Kanazawa, N., Zhang, W. Z., Nagai, T., Hara, T., Kimoto, K., Matsui, Y., Onose, Y. and Tokura, Y. Skyrmion flow near room temperature in an ultralow current density. *Nat Commun* **3**, 988 (2012).

[17] Nagaosa, N. and Tokura, Y. Topological properties and dynamics of magnetic skyrmions. *Nat Nano* **8**, 899–911 (2013).

[18] Yu, X. Z., Kanazawa, N., Onose, Y., Kimoto, K., Zhang, W. Z., Ishiwata, S., Matsui, Y. and Tokura, Y. Near room-temperature formation of a skyrmion crystal in thin-films of the helimagnet FeGe. *Nat Mater* **10**, 106–109 (2011).

[19] Romming, N., Hanneken, C., Menzel, M., Bickel, J. E., Wolter, B., von Bergmann, K., Kubetzka, A. and Wiesendanger, R. Writing and Deleting Single Magnetic Skyrmions. *Science* **341**, 636–639 (2013).

[20] Tang, S., Kravchenko, I., Yi, J., Cao, G., Howe, J., Mandrus, D. and Gai, Z. Growth of skyrmionic MnSi nanowires on Si: Critical importance of the SiO_2 layer. *Nano Res.* **7**, 1788–1796 (2014).

[21] Bleszynski-Jayich, A. C., Shanks, W. E., Peaudecerf, B., Ginossar, E., Oppen, F. v., Glazman, L. and Harris, J. G. E. Persistent Currents in Normal Metal Rings. *Science* **326**, 272–275 (2009).

[22] Jang, J., Ferguson, D. G., Vakaryuk, V., Budakian, R., Chung, S. B., Goldbart, P. M. and Maeno, Y. Observation of Half-Height Magnetization Steps in Sr_2RuO_4. *Science* **331**, 186–188 (2011).

[23] Weber, D. P., Rüffer, D., Buchter, A., Xue, F., Russo-Averchi, E., Huber, R., Berberich, P., Arbiol, J., Fontcuberta i Morral, A., Grundler, D. and Poggio, M. Cantilever Magnetometry of Individual Ni Nanotubes. *Nano Lett.* **12**, 6139–6144 (2012).

[24] Mehlin, A., Xue, F., Liang, D., Du, H. F., Stolt, M. J., Jin, S., Tian, M. L. and Poggio, M. Stabilized Skyrmion Phase Detected in MnSi Nanowires by Dynamic Cantilever Magnetometry. *Nano Letters* **15**, 4839–4844 (2015).

[25] Gross, B., Weber, D. P., Rüffer, D., Buchter, A., Heimbach, F., Fontcuberta i Morral, A., Grundler, D. and Poggio, M. Dynamic cantilever magnetometry of individual CoFeB nanotubes. *Physical Review B* **93**, 064409 (2016).

[26] Tsaturyan, Y., Barg, A., Polzik, E. and Schliesser, A. Ultra-coherent nanomechanical resonators via soft clamping and dissipation dilution. *arXiv:* 1608.00937 [quant–ph] (2016).

[27] Rugar, D., Budakian, R., Mamin, H. J. and Chui, B. W. Single spin detection by magnetic resonance force microscopy. *Nature* **430**, 329–332 (2004).

[28] Chabot, M. D. and Moreland, J. Micrometer-scale magnetometry of thin $Ni_{80}Fe_{20}$ films using ultrasensitive microcantilevers. *Journal of Applied Physics* **93**, 7897–7899 (2003).

[29] Buchter, A., Nagel, J., Rüffer, D., Xue, F., Weber, D. P., Kieler, O. F., Weimann, T., Kohlmann, J., Zorin, A. B., Russo-Averchi, E., Huber, R., Berberich, P., Fontcuberta i Morral, A., Kemmler, M., Kleiner, R., Koelle, D., Grundler, D. and Poggio, M. Reversal Mechanism of an Individual Ni Nanotube Simultaneously Studied by Torque and SQUID Magnetometry. *Physical Review Letters* **111**, 067202 (2013).

[30] Buchter, A., Wölbing, R., Wyss, M., Kieler, O. F., Weimann, T., Kohlmann, J., Zorin, A. B., Rüffer, D., Matteini, F., Tütüncüoglu, G., Heimbach, F., Kleibert, A., Fontcuberta i Morral, A., Grundler, D.,

Kleiner, R., Koelle, D. and Poggio, M. Magnetization reversal of an individual exchange-biased permalloy nanotube. *Physical Review B* **92**, 214432 (2015).

[31] Banerjee, P., Wolny, F., Pelekhov, D. V., Herman, M. R., Fong, K. C., Weissker, U., Mühl, T., Obukhov, Y., Leonhardt, A., Büchner, B. and Hammel, P. C. Magnetization reversal in an individual 25 nm iron-filled carbon nanotube. *Applied Physics Letters* **96**, 252505 (2010).

[32] Stipe, B. C., Mamin, H. J., Stowe, T. D., Kenny, T. W. and Rugar, D. Magnetic Dissipation and Fluctuations in Individual Nanomagnets Measured by Ultrasensitive Cantilever Magnetometry. *Phys. Rev. Lett.* **86**, 2874–2877 (2001).

[33] Bossoni, L., Carretta, P. and Poggio, M. Vortex lattice melting of a $NbSe_2$ single grain probed by ultrasensitive cantilever magnetometry. *Applied Physics Letters* **104**, 182601 (2014).

[34] Landeros, P., Suarez, O. J., Cuchillo, A. and Vargas, P. Equilibrium states and vortex domain wall nucleation in ferromagnetic nanotubes. *Physical Review B* **79**, 024404 (2009).

[35] Rugar, D., Mamin, H. J., Guethner, P., Lambert, S. E., Stern, J. E., McFadyen, I. and Yogi, T. Magnetic force microscopy: General principles and application to longitudinal recording media. *Journal of Applied Physics* **68**, 1169–1183 (1990).

[36] Amelinckx, S., Dyck, D. v., Landuyt, J. v. and Tendeloo, G. v. *Electron Microscopy: Principles and Fundamentals* (John Wiley & Sons, 2008).

[37] Schwarz, A. and Wiesendanger, R. Magnetic sensitive force microscopy. *Nano Today* **3**, 28 – 39 (2008).

[38] Magnetic phase imaging with transmission electron microscopy. In Zhu, Y. (ed.) *Modern Techniques for Characterizing Magnetic Materials*, 267–326 (Springer US, 2005). `http://link.springer.com/chapter/10.1007/0-387-23395-4_7`.

[39] Magnetic neutron scattering. In Zhu, Y. (ed.) *Modern Techniques for Characterizing Magnetic Materials*, 3–64 (Springer US, 2005). `http://link.springer.com/chapter/10.1007/0-387-23395-4_1`.

[40] Morss, L. R., Edelstein, N. M. and Fuger, J. *The Chemistry of the Actinide and Transactinide Elements (Set Vol.1-6): Volumes 1-6* (Springer Science & Business Media, 2010).

[41] Resonant soft x-ray techniques to resolve nanoscale magnetism. In Zhu, Y. (ed.) *Modern Techniques for Characterizing Magnetic Materials*, 159–200 (Springer US, 2005). `http://link.springer.com/chapter/10.1007/0-387-23395-4_4`.

[42] Nolting, F. Magnetic imaging with X-rays. In Beaurepaire, E., Bulou, H., Scheurer, F. and Kappler, J.-P. (eds.) *magnetism and synchrotron radiation*, vol. 133 of *Springer Proceedings in Physics* (Springer Berlin Heidelberg, 2010).

[43] Wende, H. and Antoniak, C. *X-Ray Magnetic Dichroism* (Springer Berlin Heidelberg, 2010). `http://link.springer.com/chapter/10.1007/978-3-642-04498-4_5`.

[44] Chao, W., Harteneck, B. D., Liddle, J. A., Anderson, E. H. and Attwood, D. T. Soft X-ray microscopy at a spatial resolution better than 15 nm. *Nature* **435**, 1210–1213 (2005).

[45] Graham, C. High-sensitivity magnetization measurements. *Journal of Materials Sciences and Technology* **16**, 97 (2000).

[46] Vasyukov, D., Anahory, Y., Embon, L., Halbertal, D., Cuppens, J., Neeman, L., Finkler, A., Segev, Y., Myasoedov, Y., Rappaport, M. L., Huber, M. E. and Zeldov, E. A scanning superconducting quantum interference device with single electron spin sensitivity. *Nat Nano* **8**, 639–644 (2013).

[47] Irie, A., Sasahara, H., Yamashita, T., Kurosawa, H., Yamane, H. and Hirai, T. High temperature operation of $YBa_2Cu_3O_{7-x}$ DC SQUID. *IEEE Transactions on Magnetics* **27**, 3032–3035 (1991).

[48] Weinstock, H. *SQUID Sensors: Fundamentals, Fabrication and Applications* (Springer Science & Business Media, 2012).

[49] Pathak, S. and Sharma, M. Polar magneto-optical Kerr effect instrument for 1-dimensional magnetic nanostructures. *Journal of Applied Physics* **115**, 043906 (2014).

[50] Zhang, G. P., Hübner, W., Lefkidis, G., Bai, Y. and George, T. F. Paradigm of the time-resolved magneto-optical Kerr effect for femtosecond magnetism. *Nature Physics* **5**, 499–502 (2009).

[51] Rao, C. N. R. and Raveau, B. *Colossal Magnetoresistance, Charge Ordering and Related Properties of Manganese Oxides* (World Scientific, 1998).

[52] Du, H., DeGrave, J. P., Xue, F., Liang, D., Ning, W., Yang, J., Tian, M., Zhang, Y. and Jin, S. Highly Stable Skyrmion State in Helimagnetic MnSi Nanowires. *Nano Lett.* **14**, 2026–2032 (2014).

[53] Kolb, E., Mulloy, M., Dupas, C., Galtier, M., Renard, D., Renard, J., Trigui, F. and Vélu, E. Magnetoresistance study of granular behaviour in Co/Au(111) ultrathin films. *Journal of Magnetism and Magnetic Materials* **148**, 315–316 (1995).

[54] Bakonyi, I. and Péter, L. Electrodeposited multilayer films with giant magnetoresistance (GMR): Progress and problems. *Progress in Materials Science* **55**, 107–245 (2010).

[55] Akther Hossain, A. K. M., Cohen, L. F., Damay, F., Berenov, A., MacManus-Driscoll, J., Alford, N. M., Mathur, N. D., Blamire, M. G. and Evetts, J. E. Influence of grain size on magnetoresistance properties of bulk $La_{0.67}Ca_{0.33}MnO_{3-\delta}$. *Journal of Magnetism and Magnetic Materials* **192**, 263–270 (1999).

[56] Schwarz, M. P., Grundler, D., Meinel, I., Heyn, C. and Heitmann, D. Micromechanical cantilever magnetometer with an integrated two-dimensional electron system. *Applied Physics Letters* **76**, 3564–3566 (2000).

[57] Giorgio, M., Meier, B., Magin, R. and Meyer, E. Magnetic damping losses of tipped cantilevers. *Nanotechnology* **17**, 871 (2006).

[58] Albrecht, T. R., Grütter, P., Horne, D. and Rugar, D. Frequency modulation detection using high-Q cantilevers for enhanced force microscope sensitivity. *Journal of Applied Physics* **69**, 668–673 (1991).

[59] Hauer, B., Doolin, C., Beach, K. and Davis, J. A general procedure for thermomechanical calibration of nano/micro-mechanical resonators. *Annals of Physics* **339**, 181 – 207 (2013).

[60] Montinaro, M. *Coupling of nanomechanical resonators to controllable quantum systems.* Phd thesis, University of Basel, Switzerland (2014). `http://edoc.unibas.ch/diss/DissB_11080`.

[61] Cleland, A. N. *Foundations of Nanomechanics From Solid-State Theory to Device Applications* (Springer Berlin Heidelberg, 2003). `http://dx.doi.org/10.1007/978-3-662-05287-7`.

[62] Sidles, J. A., Garbini, J. L., Bruland, K. J., Rugar, D., Züger, O., Hoen, S. and Yannoni, C. S. Magnetic resonance force microscopy. *Reviews of Modern Physics* **67**, 249–265 (1995).

[63] Yasumura, K. Y., Stowe, T. D., Chow, E. M., Pfafman, T., Kenny, T., Stipe, B. C. and Rugar, D. Quality factors in micron- and submicron-thick cantilevers. *J. MEMS* **9**, 117 – 125 (2000).

[64] Sarid, D. *Scanning Force Microscopy: With Applications to Electric, Magnetic, and Atomic Forces* (Oxford University Press, 1994).

[65] Sansa, M., Sage, E., Bullard, E. C., Gély, M., Alava, T., Colinet, E., Naik, A. K., Villanueva, L. G., Duraffourg, L., Roukes, M. L., Jourdan, G. and Hentz, S. Frequency fluctuations in silicon nanoresonators. *Nature Nanotechnology* **11**, 552–558 (2016).

[66] Jensen, K., Kim, K. and Zettl, A. An atomic-resolution nanomechanical mass sensor. *Nature Nanotechnology* **3**, 533–537 (2008).

[67] Ekinci, K. L., Yang, Y. T. and Roukes, M. L. Ultimate limits to inertial mass sensing based upon nanoelectromechanical systems. *Journal of Applied Physics* **95**, 2682–2689 (2004).

[68] Chaste, J., Eichler, A., Moser, J., Ceballos, G., Rurali, R. and Bachtold, A. A nanomechanical mass sensor with yoctogram resolution. *Nature Nanotechnology* **7**, 301–304 (2012).

[69] Drake, A. D. and Leiner, D. C. Fiber-optic interferometer for remote subangstrom vibration measurement. *Review of Scientific Instruments* **55**, 162–165 (1984).

[70] Rugar, D., Mamin, H. J., Erlandsson, R., Stern, J. E. and Terris, B. D. Force microscope using a fiber-optic displacement sensor. *Review of Scientific Instruments* **59**, 2337–2340 (1988).

[71] Rugar, D., Mamin, H. J. and Guethner, P. Improved fiber-optic interferometer for atomic force microscopy. *Applied Physics Letters* **55**, 2588–2590 (1989).

[72] Montinaro, M., Mehlin, A., Solanki, H. S., Peddibhotla, P., Mack, S., Awschalom, D. D. and Poggio, M. Feedback cooling of cantilever motion using a quantum point contact transducer. *Applied Physics Letters* **101**, 133104 (2012).

[73] Herzog, B. E., Cadeddu, D., Xue, F., Peddibhotla, P. and Poggio, M. Boundary between the thermal and statistical polarization regimes in a nuclear spin ensemble. *Applied Physics Letters* **105**, 043112 (2014).

[74] Poggio, M., Degen, C. L., Rettner, C. T., Mamin, H. J. and Rugar, D. Nuclear magnetic resonance force microscopy with a microwire rf source. *Applied Physics Letters* **90**, 263111 (2007).

[75] Nichol, J. M., Hemesath, E. R., Lauhon, L. J. and Budakian, R. Displacement detection of silicon nanowires by polarization-enhanced fiber-optic interferometry. *Applied Physics Letters* **93**, 193110 (2008).

[76] Braakman, F. R., Cadeddu, D., Tütüncüoglu, G., Matteini, F., Rüffer, D., i Morral, A. F. and Poggio, M. Nonlinear motion and mechanical mixing in as-grown gaas nanowires. *Applied Physics Letters* **105**, 173111 (2014).

[77] Rossi, N., Braakman, F. R., Cadeddu, D., Vasyukov, D., Tütüncüoglu, G., Morral, A. F. i. and Poggio, M. Vectorial scanning force microscopy using a nanowire sensor. *Nature Nanotechnology* 150–156 (2017).

[78] Mamin, H. J. and Rugar, D. Sub-attonewton force detection at millikelvin temperatures. *Applied Physics Letters* **79**, 3358–3360 (2001).

[79] Jang, J., Budakian, R. and Maeno, Y. Phase-locked cantilever magnetometry. *Applied Physics Letters* **98**, 132510 (2011).

[80] Poggio, M. Private conversation.

[81] Buchter, A. *Hybrid torque and SQUID magnetometry of individual magnetic nanotubes*. Ph.D. thesis, University of Basel, Switzerland (2015). `https://doi.org/10.5451/unibas-006483670`.

[82] Fischbacher, T., Franchin, M., Bordignon, G. and Fangohr, H. A Systematic Approach to Multiphysics Extensions of Finite-Element-Based Micromagnetic Simulations: Nmag. *IEEE Transactions on Magnetics* **43**, 2896–2898 (2007).

[83] Vansteenkiste, A., Leliaert, J., Dvornik, M., Helsen, M., Garcia-Sanchez, F. and Van Waeyenberge, B. The design and verification of MuMax3. *AIP Advances* **4**, 107133 (2014).

[84] Aharoni, A. *Introduction to the Theory of Ferromagnetism* (Oxford University Press, 2001), 2 edn.

[85] Skomski, R. and Coey, J. M. D. *Permanent Magnetism* (Institute of Physics Publishing, 1999).

[86] Guimarães, A. P. *Principles of Nanomagnetism*. NanoScience and Technology (Springer Berlin Heidelberg, 2009). `http://link.springer.com/10.1007/978-3-642-01482-6`.

[87] Morrish, A. H. *The Physical Principles of Magnetism* (Wiley, 2001).

[88] Leonov, A. *Twisted, localized, and modulated states described in the phenomenological theory of chiral and nanoscale ferromagnets.* Phd thesis, Technische Universität Dresden, Germany (2011). `http://www.qucosa.de/recherche/frontdoor/?tx_slubopus4frontend%5bid%5d=urn:nbn:de:bsz:14-qucosa-83823`.

[89] Weber, D. P. *Dynamic cantilever magnetometry of individual ferromagnetic nanotubes.* Ph.D. thesis, University of Basel, Switzerland (2014). `https://doi.org/10.5451/unibas-006323604`.

[90] Rüffer, D. *Magnetic States and Spin-Wave Modes in Single Ferromagnetic Nanotubes.* Ph.D. thesis, EPFL, Lausanne, Switzerland (2014).

[91] Hertel, R. and Kirschner, J. Magnetic drops in a soft-magnetic cylinder. *Journal of Magnetism and Magnetic Materials* **278**, L291–L297 (2004).

[92] Escrig, J., Landeros, P., Altbir, D., Vogel, E. E. and Vargas, P. Phase diagrams of magnetic nanotubes. *Journal of Magnetism and Magnetic Materials* **308**, 233–237 (2007).

[93] Landeros, P., Allende, S., Escrig, J., Salcedo, E., Altbir, D. and Vogel, E. E. Reversal modes in magnetic nanotubes. *Applied Physics Letters* **90**, 102501 (2007).

[94] Chen, A.-P., Gonzalez, J. M. and Guslienko, K. Y. Magnetization configurations and reversal of magnetic nanotubes with opposite chiralities of the end domains. *Journal of Applied Physics* **109**, 073923 (2011).

[95] Rüffer, D., Slot, M., Huber, R., Schwarze, T., Heimbach, F., Tütüncüoglu, G., Matteini, F., Russo-Averchi, E., Kovács, A., Dunin-Borkowski, R., Zamani, R. R., Morante, J. R., Arbiol, J., Morral, A. F. i. and Grundler, D. Anisotropic magnetoresistance of individual CoFeB and Ni nanotubes with values of up to 1.4% at room temperature. *APL Materials* **2**, 076112 (2014).

[96] Bilzer, C., Devolder, T., Kim, J.-V., Counil, G. and Chappert, C. Study of the dynamic magnetic properties of soft CoFeB films. *Journal of Applied Physics* **100**, 053903 (2006).

[97] Li, D., Thompson, R. S., Bergmann, G. and Lu, J. G. Template-based synthesis and magnetic properties of cobalt nanotube arrays. *Advanced Materials* **20**, 4575–4578 (2008).

[98] Wyss, M., Mehlin, A., Gross, B., Buchter, A., Farhan, A., Buzzi, M., Kleibert, A., Tütüncüoglu, G., Heimbach, F., Morral, A. F. i., Grundler, D. and Poggio, M. Imaging magnetic vortex configurations in ferromagnetic nanotubes. *Physical Review B* **96**, 024423 (2017).

[99] Landeros, P. and Núñez, l. S. Domain wall motion on magnetic nanotubes. *Journal of Applied Physics* **108**, 033917 (2010).

[100] Bachmann, J., Jing, Knez, M., Barth, S., Shen, H., Mathur, S., Gösele, U. and Nielsch, K. Ordered Iron Oxide Nanotube Arrays of Controlled Geometry and Tunable Magnetism by Atomic Layer Deposition. *Journal of the American Chemical Society* **129**, 9554–9555 (2007).

[101] Daub, M., Knez, M., Goesele, U. and Nielsch, K. Ferromagnetic nanotubes by atomic layer deposition in anodic alumina membranes. *Journal of Applied Physics* **101**, 09J111 (2007).

[102] Escrig, J., Bachmann, J., Jing, J., Daub, M., Altbir, D. and Nielsch, K. Crossover between two different magnetization reversal modes in arrays of iron oxide nanotubes. *Physical Review B* **77**, 214421 (2008).

[103] Bachmann, J., Escrig, J., Pitzschel, K., Moreno, J. M. M., Jing, J., Görlitz, D., Altbir, D. and Nielsch, K. Size effects in ordered arrays of magnetic nanotubes: Pick your reversal mode. *Journal of Applied Physics* **105**, 07B521 (2009).

[104] Rudolph, A., Soda, M., Kiessling, M., Wojtowicz, T., Schuh, D., Wegscheider, W., Zweck, J., Back, C. and Reiger, E. Ferromagnetic GaAs/GaMnAs Core-Shell Nanowires Grown by Molecular Beam Epitaxy. *Nano Letters* **9**, 3860–3866 (2009).

[105] Chong, Y. T., Görlitz, D., Martens, S., Yau, M. Y. E., Allende, S., Bachmann, J. and Nielsch, K. Multilayered Core/Shell Nanowires Displaying Two Distinct Magnetic Switching Events. *Advanced Materials* **22**, 2435–2439 (2010).

[106] Albrecht, O., Zierold, R., Allende, S., Escrig, J., Patzig, C., Rauschenbach, B., Nielsch, K. and Görlitz, D. Experimental evidence for an angular dependent transition of magnetization reversal modes in magnetic nanotubes. *Journal of Applied Physics* **109**, 093910 (2011).

[107] Baumgaertl, K., Heimbach, F., Maendl, S., Rueffer, D., Fontcuberta i Morral, A. and Grundler, D. Magnetization reversal in individual Py and CoFeB nanotubes locally probed via anisotropic magnetoresistance

and anomalous Nernst effect. *Applied Physics Letters* **108**, 132408 (2016).

[108] Nagel, J., Buchter, A., Xue, F., Kieler, O. F., Weimann, T., Kohlmann, J., Zorin, A. B., Rüffer, D., Russo-Averchi, E., Huber, R., Berberich, P., Fontcuberta i Morral, A., Grundler, D., Kleiner, R., Koelle, D., Poggio, M. and Kemmler, M. Nanoscale multifunctional sensor formed by a Ni nanotube and a scanning Nb nanoSQUID. *Physical Review B* **88**, 064425 (2013).

[109] Leonov, A. O. Chiral skyrmion states in non-centrosymmetric magnets. *arXiv:* 1406.2177 [cond–mat] (2014).

[110] Dzialoshinskii, I. Thermodynamic Theory of "Weak" Ferromagnetism in Antiferromagnetic Sustances. *Soviet Physics JETP* **5**, 1259–1272 (1957).

[111] Moriya, T. Anisotropic Superexchange Interaction and Weak Ferromagnetism. *Phys. Rev.* **120**, 91–98 (1960).

[112] Buhrandt, S. and Fritz, L. Skyrmion lattice phase in three-dimensional chiral magnets from Monte Carlo simulations. *Physical Review B* **88** (2013).

[113] Levatić, I., Popčević, P., Šurija, V., Kruchkov, A., Berger, H., Magrez, A., White, J. S., Rønnow, H. M. and Živković, I. Dramatic pressure-driven enhancement of bulk skyrmion stability. *Scientific Reports* **6** (2016).

[114] Bauer, A., Neubauer, A., Franz, C., Münzer, W., Garst, M. and Pfleiderer, C. Quantum phase transitions in single-crystal $\mathrm{Mn}_{1-x}\mathrm{Fe}_x\mathrm{Si}$ and $\mathrm{Mn}_{1-x}\mathrm{Co}_x\mathrm{Si}$: Crystal growth, magnetization, ac susceptibility, and specific heat. *Physical Review B* **82** (2010).

[115] Ruff, E., Widmann, S., Lunkenheimer, P., Tsurkan, V., Bordacs, S., Kezsmarki, I. and Loidl, A. Multiferroicity and skyrmions carrying electric polarization in $\mathrm{GaV}_4\mathrm{S}_8$. *Science Advances* **1**, e1500916–e1500916 (2015).

[116] Bogdanov, A. and Hubert, A. Thermodynamically stable magnetic vortex states in magnetic crystals. *Journal of Magnetism and Magnetic Materials* **138**, 255–269 (1994).

[117] Kézsmárki, I., Bordács, S., Milde, P., Neuber, E., Eng, L., White, J., Rønnow, H., Dewhurst, C., Mochizuki, M., Yanai, K., Nakamura,

H., Ehlers, D., Tsurkan, V. and Loidl, A. Neel-type skyrmion lattice with confined orientation in the polar magnetic semiconductor GaV_4S_8. *Nature Materials* **14**, 1116–1122 (2015).

[118] Stolt, M. J., Li, Z.-A., Phillips, B., Song, D., Mathur, N., Dunin-Borkowski, R. E. and Jin, S. Selective Chemical Vapor Deposition Growth of Cubic FeGe Nanowires That Support Stabilized Magnetic Skyrmions. *Nano Letters* **17**, 508–514 (2017).

[119] Bauer, A. and Pfleiderer, C. Magnetic phase diagram of MnSi inferred from magnetization and ac susceptibility. *Phys. Rev. B* **85**, 214418 (2012).

[120] Münzer, W., Neubauer, A., Adams, T., Mühlbauer, S., Franz, C., Jonietz, F., Georgii, R., Böni, P., Pedersen, B., Schmidt, M., Rosch, A. and Pfleiderer, C. Skyrmion lattice in the doped semiconductor Fe 1 x Co x Si. *Physical Review B* **81** (2010).

[121] Seki, S., Yu, X. Z., Ishiwata, S. and Tokura, Y. Observation of Skyrmions in a Multiferroic Material. *Science* **336**, 198–201 (2012).

[122] Rybakov, F. N., Borisov, A. B. and Bogdanov, A. N. Three-dimensional skyrmion states in thin films of cubic helimagnets. *Phys. Rev. B* **87**, 094424 (2013).

[123] Butenko, A. B., Leonov, A. A., Rößler, U. K. and Bogdanov, A. N. Stabilization of skyrmion textures by uniaxial distortions in noncentrosymmetric cubic helimagnets. *Phys. Rev. B* **82**, 052403 (2010).

[124] Li, Y., Kanazawa, N., Yu, X. Z., Tsukazaki, A., Kawasaki, M., Ichikawa, M., Jin, X. F., Kagawa, F. and Tokura, Y. Robust Formation of Skyrmions and Topological Hall Effect Anomaly in Epitaxial Thin Films of MnSi. *Phys. Rev. Lett.* **110**, 117202 (2013).

[125] Tonomura, A., Yu, X., Yanagisawa, K., Matsuda, T., Onose, Y., Kanazawa, N., Park, H. S. and Tokura, Y. Real-Space Observation of Skyrmion Lattice in Helimagnet MnSi Thin Samples. *Nano Lett.* **12**, 1673–1677 (2012).

[126] Yu, X., DeGrave, J. P., Hara, Y., Hara, T., Jin, S. and Tokura, Y. Observation of the Magnetic Skyrmion Lattice in a MnSi Nanowire by Lorentz TEM. *Nano Lett.* **13**, 3755–3759 (2013).

[127] Du, H., Liang, D., Jin, C., Kong, L., Stolt, M. J., Ning, W., Yang, J., Xing, Y., Wang, J., Che, R., Zang, J., Jin, S., Zhang, Y. and Tian,

M. Electrical probing of field-driven cascading quantized transitions of skyrmion cluster states in MnSi nanowires. *Nature Communications* **6**, 7637 (2015).

[128] Liang, D., DeGrave, J. P., Stolt, M. J., Tokura, Y. and Jin, S. Current-driven dynamics of skyrmions stabilized in MnSi nanowires revealed by topological Hall effect. *Nature Communications* **6**, 8217 (2015).

[129] Pocha, R., Johrendt, D. and Pöttgen, R. Electronic and Structural Instabilities in GaV_4S_8 and $GaMo_4S_8$. *Chemistry of Materials* **12**, 2882–2887 (2000).

[130] Fruchart, O., Nozières, J.-P., Wernsdorfer, W., Givord, D., Rousseaux, F. and Decanini, D. Enhanced Coercivity in Submicrometer-Sized Ultrathin Epitaxial Dots with In-Plane Magnetization. *Phys. Rev. Lett.* **82**, 1305–1308 (1999).

[131] Zheng, Y. and Zhu, J.-G. Switching field variation in patterned submicron magnetic film elements. *Journal of Applied Physics* **81**, 5471–5473 (1997).

[132] Rothman, J., Kläui, M., Lopez-Diaz, L., Vaz, C. A. F., Bleloch, A., Bland, J. A. C., Cui, Z. and Speaks, R. Observation of a Bi-Domain State and Nucleation Free Switching in Mesoscopic Ring Magnets. *Phys. Rev. Lett.* **86**, 1098–1101 (2001).

[133] Usov, N. A., Zhukov, A. and Gonzalez, J. Domain walls and magnetization reversal process in soft magnetic nanowires and nanotubes. *Journal of Magnetism and Magnetic Materials* **316**, 255–261 (2007).

[134] Wang, Z. Spin Waves in Nickel Nanorings of Large Aspect Ratio. *Physical Review Letters* **94** (2005).

[135] Kläui, M., Rothman, J., Lopez-Diaz, L., Vaz, C. A. F., Bland, J. A. C. and Cui, Z. Vortex circulation control in mesoscopic ring magnets. *Applied Physics Letters* **78**, 3268–3270 (2001).

[136] Garbini, J. L., Bruland, K. J., Dougherty, W. M. and Sidles, J. A. Optimal control of force microscope cantilevers. I. Controller design. *Journal of Applied Physics* **80**, 1951–1958 (1996).

[137] Bruland, K. J., Garbini, J. L., Dougherty, W. M. and Sidles, J. A. Optimal control of force microscope cantilevers. II. Magnetic coupling implementation. *Journal of Applied Physics* **80**, 1959–1964 (1996).

[138] Kimling, J., Kronast, F., Martens, S., Böhnert, T., Martens, M., Herrero-Albillos, J., Tati-Bismaths, L., Merkt, U., Nielsch, K. and Meier, G. Photoemission electron microscopy of three-dimensional magnetization configurations in core-shell nanostructures. *Phys. Rev. B* **84**, 174406 (2011).

[139] Jamet, S., Da Col, S., Rougemaille, N., Wartelle, A., Locatelli, A., Mentes, T. O., Santos Burgos, B., Afid, R., Cagnon, L., Bochmann, S., Bachmann, J., Fruchart, O. and Toussaint, J. C. Quantitative analysis of shadow x-ray magnetic circular dichroism photoemission electron microscopy. *Phys. Rev. B* **92**, 144428 (2015).

[140] Da Col, S., Jamet, S., Rougemaille, N., Locatelli, A., Mentes, T. O., Burgos, B. S., Afid, R., Darques, M., Cagnon, L., Toussaint, J. C. and Fruchart, O. Observation of Bloch-point domain walls in cylindrical magnetic nanowires. *Phys. Rev. B* **89**, 180405 (2014).

[141] Tao, Y., Navaretti, P., Hauert, R., Grob, U., Poggio, M. and Degen, C. L. Permanent reduction of dissipation in nanomechanical Si resonators by chemical surface protection. *Nanotechnology* **26**, 465501 (2015).

[142] Reiche, C. F., Körner, J., Büchner, B. and Mühl, T. Introduction of a co-resonant detection concept for mechanical oscillation-based sensors. *Nanotechnology* **26**, 335501 (2015).

[143] Körner, J., Reiche, C. F., Büchner, B., Mühl, T. and Gerlach, G. Employing electro-mechanical analogies for co-resonantly coupled cantilever sensors. *Journal of Sensors and Sensor Systems* **5**, 245–259 (2016).

[144] Körner, J., Reiche, C. F., Gemming, T., Büchner, B., Gerlach, G. and Mühl, T. Signal enhancement in cantilever magnetometry based on a co-resonantly coupled sensor. *Beilstein Journal of Nanotechnology* **7**, 1033–1043 (2016).

[145] Ramos, D., Gil-Santos, E., Malvar, O., Llorens, J. M., Pini, V., Paulo, A. S., Calleja, M. and Tamayo, J. Silicon nanowires: where mechanics and optics meet at the nanoscale. *Scientific Reports* **3** (2013).

[146] Losby, J. E., Sani, F. F., Grandmont, D. T., Diao, Z., Belov, M., Burgess, J. A. J., Compton, S. R., Hiebert, W. K., Vick, D., Mohammad, K., Salimi, E., Bridges, G. E., Thomson, D. J. and Freeman, M. R. Torque-mixing magnetic resonance spectroscopy. *Science* **350**, 798–801 (2015).

[147] Dzyaloshinsky, I. A thermodynamic theory of “weak” ferromagnetism of antiferromagnetics. *Journal of Physics and Chemistry of Solids* **4**, 241–255 (1958).

[148] Crépieux, A. and Lacroix, C. Dzyaloshinsky–Moriya interactions induced by symmetry breaking at a surface. *Journal of Magnetism and Magnetic Materials* **182**, 341–349 (1998).

[149] Yu, X. Z., Onose, Y., Kanazawa, N., Park, J. H., Han, J. H., Matsui, Y., Nagaosa, N. and Tokura, Y. Real-space observation of a two-dimensional skyrmion crystal. *Nature* **465**, 901–904 (2010).

[150] Huang, S. X. and Chien, C. L. Extended Skyrmion Phase in Epitaxial FeGe(111) Thin Films. *Phys. Rev. Lett.* **108**, 267201 (2012).

[151] Bogdanov, A. N. and Rößler, U. K. Chiral Symmetry Breaking in Magnetic Thin Films and Multilayers. *Phys. Rev. Lett.* **87**, 037203 (2001).

[152] Higgins, J. M., Ding, R., DeGrave, J. P. and Jin, S. Signature of Helimagnetic Ordering in Single-Crystal MnSi Nanowires. *Nano Lett.* **10**, 1605–1610 (2010).

[153] Szczech, J. R. and Jin, S. Epitaxially-hyperbranched FeSi nanowires exhibiting merohedral twinning. *J. Mater. Chem.* **20**, 1375–1382 (2010).

[154] Aharoni, A. Demagnetizing factors for rectangular ferromagnetic prisms. *Journal of Applied Physics* **83**, 3432–3434 (1998).

[155] Karhu, E. A., Rößler, U. K., Bogdanov, A. N., Kahwaji, S., Kirby, B. J., Fritzsche, H., Robertson, M. D., Majkrzak, C. F. and Monchesky, T. L. Chiral modulations and reorientation effects in MnSi thin films. *Phys. Rev. B* **85**, 094429 (2012).

[156] Date, M., Okuda, K. and Kadowaki, K. Electron Spin Resonance in the Itinerant-Electron Helical Magnet MnSi. *J. Phys. Soc. Jpn.* **42**, 1555–1561 (1977).

[157] Du, H., Ning, W., Tian, M. and Zhang, Y. Field-driven evolution of chiral spin textures in a thin helimagnet nanodisk. *Phys. Rev. B* **87**, 014401 (2013).

[158] Leonov, A. O., Rößler, U. K. and Mostovoy, M. Target-skyrmions and skyrmion clusters in nanowires of chiral magnets. *EPJ Web of Conferences* **75**, 05002 (2014).

[159] Roszler, U. K., Bogdanov, A. N. and Pfleiderer, C. Spontaneous skyrmion ground states in magnetic metals. *Nature* **442**, 797–801 (2006).

[160] Wang, Z., Ruff, E., Schmidt, M., Tsurkan, V., Kézsmárki, I., Lunkenheimer, P. and Loidl, A. Polar Dynamics at the Jahn-Teller Transition in Ferroelectric Ga V 4 S 8. *Physical Review Letters* **115** (2015).

[161] Ehlers, D., Stasinopoulos, I., Tsurkan, V., Krug von Nidda, H.-A., Fehér, T., Leonov, A., Kézsmárki, I., Grundler, D. and Loidl, A. Skyrmion dynamics under uniaxial anisotropy. *Physical Review B* **94** (2016).

[162] Leonov, A. Private conversation.

[163] Skomski, R., Kashyap, A., Zhou, J. and Sellmyer, D. J. Anisotropic exchange. *Journal of Applied Physics* **97**, 10B302 (2005).

[164] Fujima, Y., Abe, N. and Tokunaga, T.-H., Y. Arima. Magnetic Phase Diagram of a Lacunar Spinel GaV_4Se_8 (APS March Meeting, 2017).

[165] Montana Instruments. *Cryostation user manual.* Montana Instruments, Bozeman, MT 59715, USA, 1.11 edn. (2014). `http://www.montanainstruments.com`.

[166] American Magnetics, Inc. *Superconducting magnet system user manual.* AMI, Oak Ridge, TN 37830, USA, 0 edn. (2015). `http://www.americanmagnetics.com`.

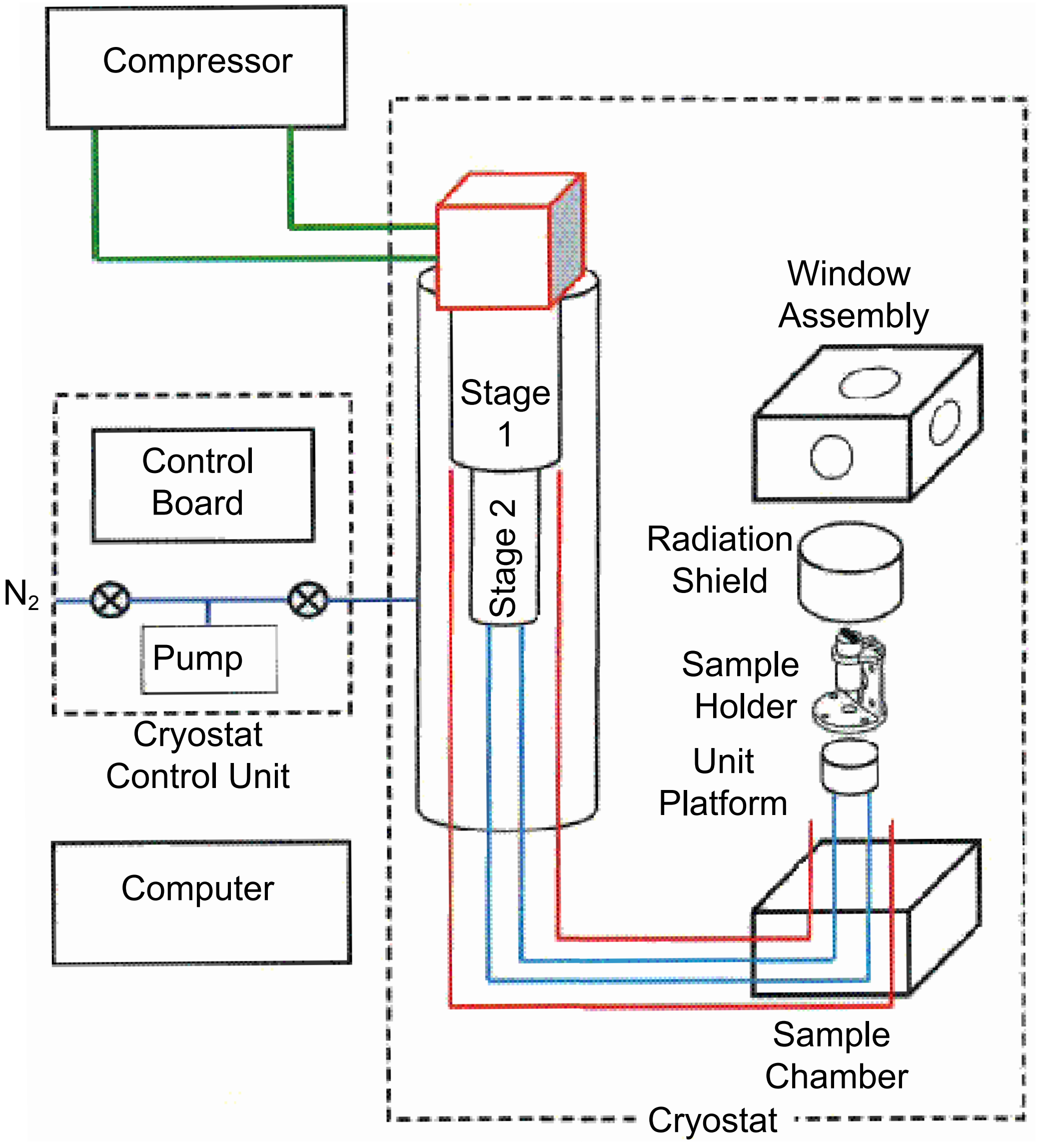

Figure A.2: Schematic of the main components of the Montana cryostation. The compressor, the control unit, and the user interface are drafted on the left side and the cryostation with its components on the right. In addition, several temperature sensors and heaters are mounted at different positions of the cryostat. Note that the sample mount for our setup is pointing down.